



**HAL**  
open science

# Oriented micro/nano-crystallization in silicate glasses under thermal or laser field for mastering optical non-linear optics in bulk

Xuan He

► **To cite this version:**

Xuan He. Oriented micro/nano-crystallization in silicate glasses under thermal or laser field for mastering optical non-linear optics in bulk. Other. Université Paris Sud - Paris XI; Wuhan University of Technology, 2013. English. NNT: 2013PA112287 . tel-01123989

**HAL Id: tel-01123989**

**<https://theses.hal.science/tel-01123989>**

Submitted on 6 Mar 2015

**HAL** is a multi-disciplinary open access archive for the deposit and dissemination of scientific research documents, whether they are published or not. The documents may come from teaching and research institutions in France or abroad, or from public or private research centers.

L'archive ouverte pluridisciplinaire **HAL**, est destinée au dépôt et à la diffusion de documents scientifiques de niveau recherche, publiés ou non, émanant des établissements d'enseignement et de recherche français ou étrangers, des laboratoires publics ou privés.

UNIVERSITE PARIS-SUD &  
WUHAN UNIVERSITY OF TECHNOLOGY  
ÉCOLE DOCTORALE : *Chimie de Paris Sud (ED470)*  
*Laboratoire de Institut de Chimie Moléculaire et Matériaux d'Orsay*

*DISCIPLINE Chimie*

THÈSE DE DOCTORAT

soutenue le 01/12/2013

par

Xuan HE

Oriented micro/nano-crystallization in silicate glasses under thermal or laser field for mastering optical non-linear optics in bulk

Directeur de thèse :  
Co-directeur de thèse :

Bertrand POUHELLEC  
Qiming LIU

Directeur de Recherche CNRS. (ICMMO/UPS)  
Professeur (WUT)

Composition du jury :

*Président du jury :*  
*Rapporteurs :*

Changzhong JIANG  
Jinyan LI  
Haizheng TAO  
Matthieu LANCRY

Prof. (WUT)  
Prof. (HUST)  
Prof. (WHUT)  
Ass./Prof. (ICMMO/UPS)

*Examineurs :*

*Membres invités :*

Xiujian ZHAO  
Xiangming HU

Prof. (ICMMO/UPS)  
Prof. (CCNU)

---

## ABSTRACT

In the past few years, nonlinear optical materials have attracted much attention due to their application in optical telecommunications. Nonlinear optical glass-related materials have been widely studied according to their advantages. Glass ceramics having an aligned microstructure would exhibit an anisotropy of physical properties. This dissertation mainly contributes to the control of micro/nano-crystallization in silicate glass in crystalline phase, distribution, size and orientation under additional field, particularly by femtosecond irradiation, to master the nonlinear optical properties of glass further. This work is significant for the design and production of novel nonlinear optical material with multi-function in future.

In this thesis, thermal field was used to induce crystals in SrO-TiO<sub>2</sub>-SiO<sub>2</sub> glass. The crystallization behavior of glasses in different heat-treated condition and their second-order nonlinear optical properties have been analyzed by Maker fringes method and X-ray diffraction measurement, respectively. It showed that the oriented crystallization of nonlinear Sr<sub>2</sub>TiSi<sub>2</sub>O<sub>8</sub> crystals can be obtained in the surface layer by heat treatment. The polar axis of oriented crystals was perpendicular to the sample surface. Moreover, by applying higher temperature or prolonging the time duration of heat treatment, the maximum intensity of second harmonic generation shifting toward 0° is likely due to the presence of randomly distributed crystals in glass and surface crystallization turns to be volume at this moment.

However, since it is hard to control crystallization by heat treatment and time-consuming, femtosecond laser irradiation was proposed to realize the control of crystallization in glass owing to the accessible control of energy deposition in time and in space. It opens fantastic opportunities to manufacture novel multifunctional materials by manipulating the crystallization of nonlinear crystals embedded in glasses. Therefore, we achieved to precipitate preferential oriented LiNbO<sub>3</sub> and Sr<sub>2</sub>TiSi<sub>2</sub>O<sub>8</sub> crystals in glass with femtosecond laser irradiation at high repetition rate (typ. 300 kHz).

In Li<sub>2</sub>O-Nb<sub>2</sub>O<sub>5</sub>-SiO<sub>2</sub> glass, we obtained micro-/nano-crystals in glass sample by

---

varying pulse energy and polarization direction. Specifically, when applying low pulse energy and polarization parallel to laser writing direction, the oriented nano-crystallization has been obtained as shown by EBSD (Electron back-scattered diffraction). Second harmonic (SH) microscopy measurement illustrated preferred orientation of crystallization in laser lines. In order to understand the exact orientation of crystals with respect to the writing direction, a series of coherent SH measurement has been achieved in pairs of laser lines written in opposite orientation. EDS (Energy Dispersive Spectrometer) and nuclear micro-probe has been used to realize the chemical analysis in laser lines. The mechanism of oriented crystallization was discussed both in static mode and in dynamic mode through illustrating the distribution of different gradients.

In SrO-TiO<sub>2</sub>-SiO<sub>2</sub> system, laser irradiation was applied both in stoichiometric and non-stoichiometric glasses. In the former case, not only the size and distribution can be controlled by varying laser parameters, but also the crystalline phase can be chosen in samples. SH microscopy measurement was used to characterize the nonlinear properties of glass and it implied that the polar axis of crystals is always along the writing direction. In non-stoichiometric glass, only pure Sr<sub>2</sub>TiSi<sub>2</sub>O<sub>8</sub> crystals were obtained. The asymmetric writing involving oriented crystallization has been studied by varying polarization and writing orientation. The orientational dependent is likely due to the combined action of oblique pulse front tilt affected by the polarization orientation plane leading to different anisotropic photosensitivity and its aftereffects to induce asymmetric distribution of thermal and chemical gradients.

**Keywords** : femtosecond laser; controllable crystallization; oriented micro-/nano-crystals; asymmetric writing; second-order nonlinear property

---

## RÉSUMÉ

Au cours des dernières années, les matériaux optiques non linéaires ont attiré beaucoup d'attention en raison de leur application dans les télécommunications optiques. Les vitro-céramiques pour l'optique non-linéaire, ayant une microstructure alignée, présentent des propriétés physiques anisotropes. Il est donc intéressant de maîtriser la cristallisation dans ce genre de verre. Nous avons étudié ici la distribution, la taille et l'orientation sous un champ supplémentaire, en particulier par l'irradiation femtoseconde, de verres silicatés. Ce travail est important pour la conception et la production de nouveaux matériaux optiques non linéaires multi- fonction.

Dans cette thèse, le champ thermique a été utilisé pour produire des cristaux dans un verre SrO-TiO<sub>2</sub>-SiO<sub>2</sub>. L'analyse a été menée à l'aide de la méthode des franges de Maker et de de diffraction des rayons X pour étudier la cristallisation et les propriétés optiques non-linéaires. Il a montré que les cristaux non linéaires Sr<sub>2</sub>TiSi<sub>2</sub>O<sub>8</sub> peut être obtenue dans la couche de surface par traitement thermique. L'axe polaire de cristaux orientés est perpendiculaire à la surface du verre. En augmentant la température ou en prolongeant la durée de traitement thermique, l'apparition d'une intensité non-nulle de génération de second harmonique (GSH) en incidence perpendiculaire indique la présence de cristaux orientés de manière aléatoire dans le volume du verre.

Etant donné la cristallisation, spatialement difficile à contrôler par traitement thermique, l'irradiation laser femtoseconde pour contrôler la cristallisation dans le verre sont proposée en raison de son contrôle précis du dépôt d'énergie dans le temps et dans l'espace. Il ouvre des possibilités fantastiques pour la fabrication de matériaux multifonctionnels par maîtrisant la cristallization des cristaux non linéaires dans le verre.

Nous avons précipité des cristaux orientés de LiNbO<sub>3</sub> et de Sr<sub>2</sub>TiSi<sub>2</sub>O<sub>8</sub> en volume par irradiation laser femtoseconde à haute cadence (typ. 300 kHz). Dans le verre Li<sub>2</sub>O-Nb<sub>2</sub>O<sub>5</sub>-SiO<sub>2</sub>, les micro-/nano-cristaux en variant l'énergie d'impulsion et la direction de polarisation ont obtenu. En particulier, lors de l'application à basse énergie et de la polarisation parallèle à la direction d'inscription du laser, la cristallization orientée en nanomètre a été démontrée par EBSD (Electron diffraction

---

rétro-diffusée). Le mesure microscopique de SH a prouvé l'orientation préférentielle de cristallisation parallèlement à la direction de déplacement du faisceau laser. Afin de comprendre l'orientation exacte des cristaux par rapport à la direction d'écriture, une série de mesurer les signaux cohérent de SH ont été réalisés dans des paires de lignes de laser avec des orientations de déplacement opposées. EDS (spectromètre à dispersion d'énergie) et la micro-sonde nucléaire ont été utilisées pour réaliser l'analyse chimique dans les lignes de laser. Nous discutons aussi le mécanisme de cristallisation orientée en mode statique et en mode dynamique en illustrant la distribution des gradients différents.

Pour le système SrO-TiO<sub>2</sub>-SiO<sub>2</sub>, l'irradiation du laser a été appliquée dans les verres stoechiométrique et non-stoechiométrique. Dans le premier cas, non seulement la taille et la distribution peuvent être contrôlées en variant les paramètres du laser, mais aussi la phase peuvent être choisis dans l'échantillon. La mesure de SH a montré que l'axe polaire de cristaux est toujours dans le sens de l'écriture. Pour le verre non-stoechiométrique, des purs cristaux de Sr<sub>2</sub>TiSi<sub>2</sub>O<sub>8</sub> ont été obtenus seulement. En utilisant EBSD, l'écriture asymétrique ont été étudiés en variant l'orientation de la polarisation et de l'écriture. On a montré ainsi que le mécanisme d'orientation est probablement dû à l'action combinée du front « tilté » de l'impulsion et à l'orientation du plan de polarisation qui conduit à une photosensibilité anisotrope. En conséquence, cela induit une distribution asymétrique des gradients thermiques et chimiques.

**Mots-clés:** le laser femtoseconde; la cristallisation contrôlable; les cristaux orientés en micro-/nanometre; l'écriture asymétrique; la propriété non linéaire de second ordre.

---

## Contents

<b>Chapter 1 General Introduction.....</b>	<b>1</b>
1.1 Motivation and aims .....	1
1.2 Outline of thesis .....	3
<b>Chapter 2 Theoretical background .....</b>	<b>7</b>
2.1 Nonlinear optical theory .....	7
2.1.1 Maxwell equations in Nonlinear Media .....	7
2.1.2 Nonlinear optical phenomenon in material.....	9
2.1.3 SHG in glasses.....	15
2.2 Mechanism of crystallization in glass .....	19
2.2.1 Basic theory of crystallization in glass .....	19
2.3.2 Methods for oriented crystallization.....	31
2.3 Laser-induced modifications in transparent glass.....	34
2.3.1 Fs laser-induced modifications .....	34
2.3.1 Fs laser-induced crystallization .....	36
<b>Chapter 3 Experimental section .....</b>	<b>44</b>
3.1 Glass fabrication .....	44
3.1.1 Preparation of $\text{Li}_2\text{O-Nb}_2\text{O}_5\text{-SiO}_2$ glass .....	44
3.1.2 Preparation of $\text{SrO-TiO}_2\text{-SiO}_2$ glass .....	45
3.1.3 Polishing of glass samples .....	46
3.2 The treatment by additional fields .....	47
3.2.1 Thermal treatment.....	47
3.2.2 Irradiation set-up by femtosecond laser.....	48
3.3 Characterization of induced structural modification .....	49
3.3.1 Chemical analysis .....	50
3.3.2 XRD .....	51
3.3.3 Combined Micro-Raman and Micro-SHG mapping .....	52
3.3.4 SEM-EBSD .....	53
3.3.5 Refractive index information.....	55
3.3.7 Nonlinear optical properties .....	56
<b>Chapter 4 Thermally induced Nano-crystallization in <math>\text{SrO-TiO}_2\text{-SiO}_2</math> glasses ...</b>	<b>60</b>

---

4.1 Experimental details .....	60
4.2 Experimental results .....	61
4.3 Discussion.....	65
4.4 Conclusions .....	71
<b>Chapter 5 Photo-induced oriented nano-crystals in LNS glass by fs laser irradiation.....</b>	<b>73</b>
5.1 Experimental details .....	73
5.2 Experimental results .....	74
5.2.1 Photo-induced oriented crystallization in glass .....	74
5.2.2 Chemical analysis of laser-induced crystallization.....	77
5.2.3 The orientation of nano-crystallization by SHG.....	82
5.3 Discussions .....	89
5.3.1 Fs laser-induced crystallization mechanism .....	89
5.3.2 Oriented crystallization.....	92
5.4 Conclusion .....	95
<b>Chapter 6 Photo-Induced oriented crystallization in STS glass by fs laser .....</b>	<b>98</b>
6.1 Photo-induced oriented crystallization in the glass 40SrO-20TiO <sub>2</sub> -40SiO <sub>2</sub> (STS1).....	98
6.1.1 The crystallization induced by fs laser .....	98
6.1.2 The orientation of induced crystallization by fs laser irradiation .....	105
6.2 Photo-induced asymmetric oriented crystallization in the glass 33.3SrO-16.7TiO <sub>2</sub> -50SiO <sub>2</sub> (STS-2).....	112
6.2.1 The crystallization induced by fs laser .....	112
6.2.2 Asymmetric oriented crystallization induced by fs laser.....	114
6.2.3 Polarization direction and orientation writing dependence of crystallization orientation induced by fs laser. ....	119
6.3 Discussion.....	121
6.4 Conclusion .....	125
<b>Chapter 7 Summery and perspective.....</b>	<b>128</b>
7.1 Summery of thesis .....	128
7.2 Perspective.....	130

---

<b>Appendix SHG simulation .....</b>	<b>132</b>
<b>Publication list.....</b>	<b>139</b>

---

## List of figures

<b>Figure 2.1</b> Index surface of fundamental wave (blue) and second harmonic wave (red) of a negative uniaxial crystal. The angle $\theta$ indicate the propagation direction of waves for phase matching with respect to the z axis of crystal. ....	14
<b>Figure 2.2</b> Free energy diagram for nucleation with the existence of a “critical nucleus” .....	21
<b>Figure 2.3</b> (a) Effect of temperature on the size and free energy of formation of a critical nucleus ( $\Delta T_1 > \Delta T_2$ ). (b) Relation between the degree of supercooling and the nucleation rate. ....	24
<b>Figure 2.4</b> kinetic of crystal growth.....	26
<b>Figure 2.5</b> the evaluation of nucleation rate $N(T)$ and crystal growth rate $C(T)$ .	27
<b>Figure 2.6</b> Binary diagram of system A-B.....	28
<b>Figure 2.7</b> The schematic profiles of concentration and diffusion processes of two different mechanisms of phase separation: (a) spinodal decomposition and (b) nucleation-growth in function of time with $t_1 < t_2 < t_3$ .....	29
<b>Figure 2.8</b> A TTT diagram of glass with fraction of crystallized volume at $10^{-6}$ and 99% .....	30
<b>Figure 2.9</b> Pulse energy versus numerical aperture diagram in log-log scale defining regions with different kinds of laser interaction with pure silica. N.B.: the blue discontinuous line marks the position where we have precisely positioned the thresholds by means of different types of observations <sup>[106-107]</sup> .....	35
<b>Figure 3.1</b> glass forming diagram of SrO-TiO <sub>2</sub> -SiO <sub>2</sub> system. ....	45
<b>Figure 3.2</b> DSC curve of 33.3SrO-16.7TiO <sub>2</sub> -50SiO <sub>2</sub> system.....	46
<b>Figure 3.3</b> Experimental set-up of 3D laser writing inside glass. The rectangle in dashed-line presents the additional dispositive for SHG measurement. .	48
<b>Figure 3.4</b> Scheme of laser irradiation inside glass. Laser propagates: z-axis, writing and polarization direction: x-axis or y-axis.....	49

---

<b>Figure 3.5</b> Scheme of nuclear microprobe set-up in CEA/Saclay in Orsay.....	51
<b>Figure 3.6</b> The photo of micro-Raman and micro-SHG experimental set-up ....	53
<b>Figure 3.7</b> the schematic diagram of EBSD implementation (a) and an indexed Kikuchi pattern (b) of SrTiO <sub>3</sub> crystal obtained by SEM-EBSD.....	54
<b>Figure 3.8</b> schematc drawing of Senarmont compensator configuration .....	55
<b>Figure 3.9</b> The schema of Maker fringes experiments principle in transmission mode. $k_i$ is the wave vector of incident beam at fundamental wavelength (1064 nm). $k_{2i}$ is the wave vector of transmitted beam at double frequency (532 nm). The $\theta$ of the sample supporter is the angle between the $k_i$ direction and normal direction $n$ to the sample surface.....	57
<b>Figure 3.10</b> The experimental set-up of Maker fringes measurement .....	58
<b>Figure 4.1</b> UV-Vis-near IR optical transmission spectra for as-treated samples and heat-treated glasses at $T_{HT}=790^\circ\text{C}$ - $910^\circ\text{C}$ for 2 h.....	62
<b>Figure 4.2</b> Maker fringe patterns for transparent crystallized glasses obtained by heat-treatments at $T_{HT}=790^\circ\text{C}$ - $910^\circ\text{C}$ for 2 h. ....	63
<b>Figure 4.3</b> XRD patterns for the (a) as-treated glass and the surface region of transparent crystallized glasses heat-treated at (b) $850^\circ\text{C}$ for 2h and (c) $910^\circ\text{C}$ for 2h. ....	64
<b>Figure 4.4</b> SEM images of the surface and the cross-section (insert picture) heat-treated at $T_{HT}=850^\circ\text{C}$ for 2h. ....	67
<b>Figure 4.5</b> Maker fringe patterns of $\alpha$ -quartz and transparent crystallized glasses obtained by heat-treatments at $T_{HT}=850^\circ\text{C}$ for 2h-5h. ....	67
<b>Figure 4.6</b> Maker fringe patterns of a commercial z-cut quartz plate with polarization “p” (a) and calculated Maker fringe patterns (b) with the same polarization and thickness.....	68
<b>Figure 4.7</b> Calculated transmitted SHG Maker-fringes patterns (@ MAP/LPCES/ICMMO/PSUD, black and green lines) and experimental and calculated transmitted SHG Maker-fringes patterns (@ Bordeaux, red, blue, pink and brown lines) for thermally poled glass <sup>[9]</sup> .....	69
<b>Figure 4.8</b> Calculated transmitted SHG Maker-fringes intensity as function of sample thickness $L_e$ of Z-cut quartz at “s”,and (b) is a magnification of (a).	

---

.....	70
<b>Figure 4.9</b> The obtained Maker fringes in experiment (a) and in simulation (b) of the sample heated at 850°C for 2h .....	71
<b>Figure 5.1</b> Pulse energy versus repetition rate with different processing thresholds of femtosecond laser interaction with LNS glass. Other laser parameters: OB: optical breakdown; CF: crystallization formation. Dots in the graph indicate the investigations performed in this work <sup>[1]</sup> .....	74
<b>Figure 5.2</b> EBSD scan images of written line cross-sections irradiated at 2.0 to 0.6 μJ (with polarization parallel $\vec{e}$ to the laser motion direction $\vec{v}$ ) coding the crystal orientation along x (a). (b) EBSD images coding crystal orientation along x of written line cross-sections irradiated at 2.0 μJ with a polarization perpendicular to the scanning direction. EBSD scan image coding the crystal orientation are along x axis and along y axis at 1.0μJ (c) and 0.6μJ (d), respectively. The polarization for writing is parallel to the laser motion direction. Laser tracks were profiled in red dashed-line. Other laser parameters: 300 kHz, 5 μm/s, 300 fs, 1030 nm, NA = 0.6.....	76
<b>Figure 5.3</b> Micro-Raman scattering (Ar <sup>+</sup> laser 515 nm) spectra at room temperature for unirradiated area (black curve) and the irradiated crystalline line (red curve) in LNS glass. Laser parameters: 300 kHz, 1.5 μJ, 5 μm/s, 300 fs, 1030 nm, NA = 0.6, $\vec{e} \parallel \vec{v}$ .....	78
<b>Figure 5.4</b> SEM image (a) and EDX line-scanning spectra (b) of the cross-section of laser trace written at 0.9μJ, 5μm/s, 300 kHz, 300 fs, NA=0.6, $\vec{e} \parallel \vec{v}$ . The position of laser trace in (a) corresponds to the region between the two black lines in (b). .....	79
<b>Figure 5.5</b> SEM image (left) and WDS line-scanning spectra (right) of the cross-section of laser trace written at 0.6 μJ (a) and at 0.8 μJ (b). Other laser parameters: 5μm/s, 300 kHz, 300 fs, NA=0.6, $\vec{e} \parallel \vec{v}$ . The position of laser trace in (a) involves the region between the two black lines in (b). .....	80
<b>Figure 5.6</b> Optical image (a) of pairs of laser traces in y-z plane and concentration mapping of Li element (b) of one laser trace written at 0.9 μJ (the one inside the red box in fig. 5a). Other laser parameters: 5μm/s, 300	

---

kHz, 300 fs, NA=0.6, $\vec{e} \parallel \vec{v}$ . The cartographic area is 14 x 14 $\mu\text{m}^2$ in red rectangle.....	81
<b>Figure 5.7</b> Optical image (a) of pairs of laser traces in y-z plane and concentration mapping of Si (b) and Li elements (c) of laser traces written at 1.9 $\mu\text{J}$ . Other laser parameters: 5 $\mu\text{m/s}$ , 300 kHz, 300 fs, NA=0.6, $\vec{e} \parallel \vec{v}$ . The cartographic area is 70 x 35 $\mu\text{m}^2$ in red rectangle. ....	81
<b>Figure 5.8</b> SEM image of pair of laser traces in xy plane (left) and EDX line-scanning spectra of Si and Nb elements (right) of laser traces written in transversal (a) and in longitudinal (b) direction, respectively. Other laser parameters: 2.0 $\mu\text{J}$ , 5 $\mu\text{m/s}$ , 300 kHz, 300 fs, NA=0.6, $\vec{e} \parallel \vec{v}$ . The blue dashed lines gave the outlines of these two laser tracks in glass.....	82
<b>Figure 5.9</b> (a) Second harmonic microscopy images of 2 written lines at different pulse energies below the glass surface of 350 $\mu\text{m}$ ; (b) Polarization dependence of normalized SH intensity of the written lines at 0.5 $\mu\text{J}$ (red), 0.7 (black) and 1.0 $\mu\text{J}$ (blue) as a function of probing polarization angle. The line direction is at 0° (//x). Other laser parameters: 300 kHz, 5 $\mu\text{m/s}$ , 300 fs, 1030 nm, NA = 0.6, $\vec{e} \parallel \vec{v}$ . ....	84
<b>Figure 5.10</b> The schematic illustration of investigation of orientational writing dependence of crystallization using different sizes of probe laser beam. The written distance between the two lines L1 and L2 is fixed at 30 $\mu\text{m}$ by writing program. This pair of laser lines was written in two orientations along x-axis (Xp-x and Xn-x defined in chapter 3). The white arrows correspond to possible orientation of polar axis detected in the measurement. ....	85
<b>Figure 5.11</b> The experimental (solid line) and simulated (dash line or dotted dash line) SH intensity curves at different probe beam sizes of laser lines written at 1.5 (a), 1.0 (b) and 0.6 $\mu\text{J}$ (c). The noted “p” on the left side presents the input linear polarization along y-axis (perpendicular to laser lines) while the “s” indicates the polarization along x-axis (parallel to the laser lines).....	89
<b>Figure 5.12</b> (a) the schema of interaction volume passing a given point A (b)	

---

Temperature-nucleation and crystal growth rate diagram (left) and Temperature-time profiles at point A at different pulse energies (right): E1 (red)> E2 (yellow)>E3(blue).....	91
<b>Figure 6.1</b> Micro-Raman scattering spectra at room temperature for glass substrate and irradiated crystalline in STS-1 glass. Laser parameter: 300 kHz, 0.7 $\mu$ J, 5 $\mu$ m/s, 300fs, 1030nm, NA=0.6,.....	101
<b>Figure 6.2</b> SEM image of entire morphology of cross-section of laser trace written at 0.7 $\mu$ J in STS-1 glass after cleaving and etching with 2% HF acid for 30s and magnified part at the head of cross-section (b) and EDX line scanning spectra (c). The fs laser propagation is along z-axis, from the top to bottom of the photographs. Laser parameter: 300 kHz, 5 $\mu$ m/s, 300fs, 150 $\mu$ m, 1030nm, NA=0.6, $\vec{e} \parallel \vec{v}$ .....	102
<b>Figure 6.3</b> SEM images of cross-section of the written lines irradiated 150 $\mu$ m below the glass surface after having cleaved, polished and etched with 2%HF for 30s. Laser parameters:(a) 1.7 $\mu$ m, 3 $\mu$ m/s;(b) 1.7 $\mu$ J, 5 $\mu$ m/s;(c) 1.7 $\mu$ J, 20 $\mu$ m/s; (d) 1.5 $\mu$ J, 3 $\mu$ m/s; (e) 1.5 $\mu$ J, 10 $\mu$ m/s; (f) 1.3 $\mu$ J, 3 $\mu$ m/s; (g) 0.7 $\mu$ J, 3 $\mu$ m/s; (h) 0.7 $\mu$ J, 5 $\mu$ m/s; (i) 0.7 $\mu$ J, 10 $\mu$ m/s; other parameters: 300 kHz, 300 fs, 1030 nm, NA = 0.6, $\vec{e} \parallel \vec{v}$ .....	104
<b>Figure 6.4</b> EBSD images coding the orientation of Sr <sub>2</sub> TiSi <sub>2</sub> O <sub>8</sub> crystals along x-axis in the cross-section of the written lines irradiated 150 $\mu$ m below the glass surface after having cleaved, polished and etched with 2% HF for 30s. Laser parameters:(a) 1.7 $\mu$ m, 20 $\mu$ m/s; (b) 1.5 $\mu$ J, 3 $\mu$ m/s; (c) 1.5 $\mu$ J, 10 $\mu$ m/s; (d) 1.3 $\mu$ J, 3 $\mu$ m/s; (e) 0.7 $\mu$ J, 3 $\mu$ m/s; (f) 0.7 $\mu$ J, 5 $\mu$ m/s; (g) 0.7 $\mu$ J, 10 $\mu$ m/s; other parameters: 300 kHz, 300 fs, 1030 nm, NA = 0.6, $\vec{e} \parallel \vec{v}$ ..	107
<b>Figure 6.5</b> EBSD images (a) coding the orientation of Sr <sub>2</sub> TiSi <sub>2</sub> O <sub>8</sub> crystals along x-axis and orientation distribution functions (ODFs) (b) in the cross-section of the written lines irradiated 150 $\mu$ m below the glass surface after having cleaved, polished and etched with 2% HF for 30s. Laser parameters: 1.5 $\mu$ J, 3 $\mu$ m/s, 300 kHz, 300 fs, 1030 nm, NA = 0.6, $\vec{e} \parallel \vec{v}$ .....	108
<b>Figure 6.6</b> EBSD images coding the orientation of Sr <sub>2</sub> TiSi <sub>2</sub> O <sub>8</sub> crystals along x-axis of the sample (a) and angular distribution of c axis (001 pole figures)	

obtained in the cross-section of the same written lines irradiated 150  $\mu\text{m}$  below the glass surface after having cleaved, polished and etched with 2% HF for 30s. Laser parameters:(a) 1.7  $\mu\text{m}$ , 20  $\mu\text{m/s}$ ; (b) 1.5  $\mu\text{J}$ , 10  $\mu\text{m/s}$ ; (c) 1.3  $\mu\text{J}$ , 3  $\mu\text{m/s}$ ; (d) 0.7  $\mu\text{J}$ , 3  $\mu\text{m/s}$ ; other parameters: 300 kHz, 300 fs, 1030 nm, NA = 0.6,  $\vec{e} \parallel \vec{v}$ . .....109

**Figure 6.8** The SEM image (a) and EDX line scanning spectra (right to left) of the cross section of laser track at the head (b) and at the tail (c), respectively. The grey regions in (b) and (c) are the white fracture as shown in (a). The concentration in weight of each element in zone i (i=I, II, or III) is named as  $C_i$  (Si, Sr or Ti). The colored pointed-lines present the  $C_i$  in the parent glass to observe well the change tendency in zone I, II and III..... 114

**Figure 6.9** IQ maps (a) and IPF maps (b) of cross section of laser lines. Other laser parameters: 300 kHz, 1.7  $\mu\text{J}$ , 10  $\mu\text{m/s}$ , 300 fs, 1030 nm, NA = 0.6, laser polarization is parallel to the written lines. The colors in IPF map of EBSD-scan based on Pb4m space group and  $\text{Sr}_2\text{TiSi}_2\text{O}_8$  crystal parameters indicate the crystal axis  $\langle a b c \rangle$  which is normal to the image plane. ....115

**Figure 6.10** IPF images of EBSD-scan color coding the longitudinal (a) and transversal (b) orientation of polar-axis which are corresponding to the  $\mu$ -SHG mapping images with vertical (c) and horizontal (d) probing polarization of the cross-section of laser lines written at 1.7  $\mu\text{J}$  in 10 $\mu\text{m/s}$ , respectively. N. B. The colors in two IPF maps of EBSD-scan indicate the crystal axis  $\langle a b c \rangle$ , which is parallel to the applied polarization in (c) and (d), respectively.....117

**Figure 6.11** Polarization dependence of SH intensity of the written lines (a) at 1.7  $\mu\text{J}$  150  $\mu\text{m}$  below the glass surface as a function of probe polarization angle, and the line direction is at  $0^\circ$ . Insert images: (b) Second harmonic microscopy image of one line written at 1.7 $\mu\text{J}$  with probing polarization parallel to laser lines. (c) 001 pole figure obtained at the same polished laser track surface as in Fig. 1. N.B.: the laser focus has been enlarged and thus the probe intensity is below modification threshold during the SH intensity measurement..... 118

---

**Figure 6.12** IPF EBSD maps of cross section of laser lines written at configuration Xp-x (a), Yp-y(b) and Yp-x(c) in STS-2 glass. The corresponding polar figures are displayed in (d), (e) and (f), respectively. Other laser parameters: 300 kHz, 0.7  $\mu$ J, 5  $\mu$ m/s, 300 fs, 1030 nm, NA = 0.6. The colors in IPF map of EBSD-scan based on Pb4m space group and Sr<sub>2</sub>TiSi<sub>2</sub>O<sub>8</sub> crystal parameters indicate the crystal axis  $\langle a b c \rangle$  is normal to the image plane ( $//x$  axis).....120

**Figure 6.13** IPF EBSD maps of cross section of laser lines written at configuration Yn-x (a) and Yp-x(b) in STS-2 glass. Other laser parameters: 300 kHz, 0.7  $\mu$ J, 5  $\mu$ m/s, 300 fs, 1030 nm, NA = 0.6.....121

---

## List of tables

<b>Table 3.1</b> Glass composition of SrO-TiO <sub>2</sub> -SiO <sub>2</sub> system .....	45
<b>Table 3.2</b> Typical polishing parameters of glass samples .....	47
<b>Table 5.1</b> The simulated variants of SH intensity curves at “p” .....	87
<b>Table 5.2</b> The simulated variants of SH intensity curves at “s” .....	88
<b>Table 6.1</b> The measured retardance (nm) of laser tracks in x-y plan by Senarmon method. Other laser parameters: 300 kHz, 300 fs, 1030 nm, NA = 0.6, Xp-x writing configuration. ....	100
<b>Table 6.2</b> The detailed information concerning to the size of interaction volume, location and crystalline phase of induced crystals in laser tracks shown in figure 6.3. ....	105

---

## ACKNOWLEDGEMENT

In my three years as a student at Wuhan university of Technology and University of Paris Sud, I have learned a great deal about both science and life. The journey has been as rewarding as challenging. In these pages, I would like to thank the many friends and colleagues who helped me with the work presented in this thesis.

First I am very grateful to my advisor Prof. POUHELLEC Bertrand, Prof. LIU Qiming and Dr. LANCRY Matthieu for their kindly help during these years. They taught me about optics, research and life as a scientist and always are receptive and supportive to my ideas, allowing me the opportunity to direct the course of my research. This unique challenge makes me become a better and confident scientific worker. On a personal level, one could not ask for a better advisor than Bertrand, Qiming and matthieu, especially during my stay in France. They always asked me how my days were going before they asked me about the experiment no matter when I was in Paris or in Wuhan.

I would also like to thank Prof. ZHAO Xiujian for his encouragement and guide. I am grateful that matthieu let me try new ideas and gave me precious advice during my thesis. Moreover, he always had an encouraging interest in my work. I was very fortunate to work with Mr. BRISSET Francois, an excellent microscopist, and Dr. DUSSAUZE Marc in University of Bordeaux-I to give experimental support during my thesis. For their help and support, I would also like to thank colleagues in the State Key Laboratory of Silicate Materials for Architectures for supporting my work in the lab for these years, such as Prof. YUAN Qihua, Mr. ZHOU Xuedong, Prof. HAN Jianjun, Prof. TAO Haizheng, Mr. KE Ju, Mr. FENG Jinyang. And I also should say thanks to my dear friends, beautiful XIA Lian, Mrs. WANG Xuelai and Mrs. ZHOU Wei, handsome FAN Chaxing and Mr. Right WANG Wei, and my good friends COSTE Sylvain, ERRAJI-CHAHID Abdel, WEICKMAN Antoine, DESMARCHELIER Rudy and HEILI Manon in LPCES/UPS. I hope that health and happiness will accompany them forever.

Finally I would like to thank my family for their loving support throughout these

---

many years of my education. My parents encouraged me throughout my undergraduate and graduate studies, and supported me selflessly whatever I chose in these years. I hope I can count on more of the same in the future.

# Chapter 1 General Introduction

## 1.1 Motivation and aims

In the past few years, the nonlinear optical materials have attracted much attention due to their application in optical telecommunications<sup>[1-2]</sup>. Nonlinear optical glass-related materials have been widely studied according to their advantages. Moreover, in order to develop micro photonic devices nonlinear optical response at the micrometer or nanometer should be structured, while optical elements with large scale dimensions and large damage threshold should be developed for high power laser facilities<sup>[3]</sup>. It was reported that glass ceramics having an aligned microstructure would have great impact on applications through a possible anisotropy of physical properties<sup>[4]</sup>. Therefore, the production of structured crystalline materials with glass as the precursor has been recognized as an effective approach to fabricate functional materials.

So far, several methods have been proposed to facilitate controlled crystallization, including melting-quenching<sup>[5]</sup>, ultrasonic surface treatment<sup>[6]</sup>, mechanical hot extrusion<sup>[7]</sup>, crystallization under electric field or magnetic field<sup>[8-9]</sup>, etc. Recently, femtosecond (fs) laser processing has been recognized as a powerful tool to provide transparent material with new functionalities. For instance, this technique is able to induce space-selective structural change and can be utilized to fabricate optical devices such as optical waveguides, photonic crystals, Bragg gratings, and so on<sup>[10-26]</sup>. As far as concerned, nonlinear effects are regarded as important roles in energy transference and structural modification during laser-matter interaction process. There are two kinds of absorption mechanisms for structural modification. For high energy pulse, the appearance of multiphoton or tunneling ionization at the beginning of the pulse will result in massive free electron plasma, and pulse energy will be then absorbed via one or several-photon absorption mechanism of inverse bremsstrahlung heating<sup>[27]</sup>. For low energy pulse, when ultrashort laser pulses are focused inside glass, it was observed that a memory in

nonlinear ionization of transparent solids and reduction in ionization threshold with number of laser pulses. Meantime, the self-organized nanostructures can be formed because of the positive feedback and local field effects<sup>[28]</sup>. At high repetition rate, the absorbed energy in the focal point cannot dissipate or diffuse timely to outer region before the arrival of the next pulse. Thus, the deposited energy will continuously accumulate and a high temperature is generated in the irradiated region<sup>[29-32]</sup>. The laser-induced crystallization might occur during this heating process or the thermal diffusion procedure after the departure of laser spot. In the past decade, a series of nonlinear crystals such as  $\beta$ -BaB<sub>2</sub>O<sub>4</sub><sup>[16, 33]</sup>, Ba<sub>2</sub>TiSi<sub>2</sub>O<sub>8</sub><sup>[34-36]</sup>, LiNbO<sub>3</sub><sup>[33, 36-37]</sup>, Ba<sub>2</sub>TiGe<sub>2</sub>O<sub>8</sub><sup>[38]</sup> and Sr<sub>2</sub>TiSi<sub>2</sub>O<sub>8</sub><sup>[39]</sup> as well as crystalline Ge<sup>[40]</sup> inside bulk glass were space-selectively precipitated using fs laser irradiations. In addition, with the additional heating equipment or spatial light modulator, Stone et al.<sup>[41-43]</sup> have succeeded in patterning three-dimensional ferroelectric single crystal architecture with its c-axis aligned along the femtosecond laser scanning direction inside a LaBGeO<sub>5</sub> glass. The second harmonic generation (SHG) has been observed in glass due to the appearance of functional crystals.

However, as far as we know, how to control the nonlinear optical properties of via mastering nano-crystallization, particularly in distribution, phase, and orientation inside glass by solely adjusting fs laser irradiation parameters is still under investigation. In this thesis, two kinds of typical frequency-conversion crystals, such as LiNbO<sub>3</sub>-like and Sr<sub>2</sub>TiSi<sub>2</sub>O<sub>8</sub> crystals have been space-selectively photo-induced in glass. It has been found that oriented micro/nano-crystallization in Li<sub>2</sub>O-Nb<sub>2</sub>O<sub>5</sub>-SiO<sub>2</sub> glass system can be achieved just by adjusting the main laser parameters including pulse energy, writing speed as well as laser polarization. And the oriented crystallization in SrO-TiO<sub>2</sub>-SiO<sub>2</sub> glass system depends on the applied laser parameters but also its chemical composition. Parallely, thermal-induced nano-crystallization in SrO-TiO<sub>2</sub>-SiO<sub>2</sub> glass system has also been carried out as a contrast. The nonlinear optical properties of these glass containing nano-crystals indicate that the laser-induced crystallization could become the most efficient method for the production of useful optical devices.

## 1.2 Outline of thesis

Since the objective of work is to define the possibility of controllable nano-crystallization and orientation by additional field (short investigation on traditional heat treatment and detailed research on advanced illumination by ultra-fast laser.) in order to control the nonlinear optical properties of material, this thesis will be described in following chapters:

- **In chapter 2**, the theoretical basic knowledge involving nonlinear optical property, glass crystallization theory and laser-matter interaction in transparent material will be introduced.
- **Chapter 3** will give a basic introduction on glass fabrication process, fs laser illumination and characterization methods used in this work.
- **In chapter 4**, the thermal induced nano-crystallization in SrO-TiO<sub>2</sub>-SiO<sub>2</sub> glass system was described. The crystallization on surface was observed firstly by mean of SEM and XRD. The second nonlinear optical property of treated sample and the crystallization have been investigated by Maker fringes method. The SHG simulation of Maker fringes method will be illustrated particularly in the thickness dependence of efficient NLO layer in the material.
- **In chapter 5**, with respect to the illumination treatment by ultrafast laser, we investigated the controllable nano-crystallization in Li<sub>2</sub>O-Nb<sub>2</sub>O<sub>5</sub>-SiO<sub>2</sub> (LNS) firstly based on the previous work in PSUD group. The mechanism of laser-induced crystallization will be interpreted. Furthermore, SHG simulation was used to determine the general orientation of crystals polar-axis in a pair of laser lines.
- **In chapter 6**, as a subsequent, to verify our understandings for controlling oriented crystallization by fs laser according to chapter 5, we will turn to investigate the laser-induced precipitation of nonlinear crystals Sr<sub>2</sub>TiSi<sub>2</sub>O<sub>8</sub> in SrO-TiO<sub>2</sub>-SiO<sub>2</sub> glass system taking profit of knowledge deduced from the results in chapter 4. This chapter will be divided into two parts: the crystallization in the glass 40SrO-20TiO<sub>2</sub>-40SiO<sub>2</sub> (mol%) with

stoichiometric composition to the nonlinear phase and in the glass 33.3SrO-16.7TiO<sub>2</sub>-50SiO<sub>2</sub> (mol%) with non-stoichiometric composition. A systematical characterization in term of the phase, distribution, size and orientation of photo-induced crystals in glass will be given and mechanism of controlling crystallization will be discussed subsequently.

- In the following part, **chapter 7**, we will draw some conclusions from the work in this thesis.

## References

- [1]. Aitchison, J. S., Prohaska, J. D., Vogel, E. M., The nonlinear optical properties of glass. *Met Mater Process* **1997**, 8 (4), 277-290.
- [2]. Qiu, J. R., Si, J. H., Hirao, K., Photoinduced stable second-harmonic generation in chalcogenide glasses. *Opt Lett* **2001**, 26 (12), 914-916.
- [3]. Gu, J. M., Yan, Y. L., Zhao, Y. S., *et al.*, Controlled Synthesis of Bulk Polymer Nanocomposites with Tunable Second Order Nonlinear Optical Properties. *Adv Mater* **2012**, 24 (17), 2249-2253.
- [4]. McMillan, P. W., Glass Ceramics. Academic Press: London, 1974.
- [5]. Ding, Y., Miura, Y., Nakaoka, S., *et al.*, Oriented surface crystallization of lithium niobate on glass and second harmonic generation. *J Non-Cryst Solids* **1999**, 259, 132-138.
- [6]. Ding, Y., Miura, Y., Yamaji, H., Oriented surface crystallisation of lithium disilicate on glass and the effect of ultrasonic surface treatment. *Phys Chem Glasses* **1998**, 39 (6), 338-343.
- [7]. Ashbee, K. H. G., Anisotropic glass-ceramics produced by extrusion through opposed dies. *J Mater Sci* **1975**, 10 (6), 911-917.
- [8]. Keding, R., Russel, C., The mechanism of electrochemically induced nucleation in glass melts with the composition 2BaO center dot TiO<sub>2</sub> center dot 2.75SiO<sub>2</sub>. *J Non-Cryst Solids* **2005**, 351 (16-17), 1441-1446.
- [9]. Toyohara, N., Benino, Y., Fujiwara, T., *et al.*, Enhancement and depression in second-order optical nonlinearity of Ba<sub>2</sub>TiGe<sub>2</sub>O<sub>8</sub> in crystallized glass prepared in a high magnetic field. *J Appl Phys* **2006**, 99 (4).
- [10]. Davis, K. M., Miura, K., Sugimoto, N., *et al.*, Writing waveguides in glass with a femtosecond laser. *Opt Lett* **1996**, 21 (21), 1729-1731.
- [11]. Glezer, E. N., Milosavljevic, M., Huang, L., *et al.*, Three-dimensional optical storage inside transparent materials. *Opt Lett* **1996**, 21 (24), 2023-2025.
- [12]. Glezer, E. N., Mazur, E., Ultrafast-laser driven micro-explosions in transparent materials. *Appl Phys Lett* **1997**, 71 (7), 882-884.
- [13]. Miura, K., Qiu, J. R., Inouye, H., *et al.*, Photowritten optical waveguides in various glasses with ultrashort pulse laser. *Appl Phys Lett* **1997**, 71 (23), 3329-3331.
- [14]. Homoelle, D., Wielandy, S., Gaeta, A. L., *et al.*, Infrared photosensitivity in silica glasses exposed to femtosecond laser pulses. *Opt Lett* **1999**, 24 (18), 1311-1313.
- [15]. Sudrie, L., Franco, M., Prade, B., *et al.*, Writing of permanent birefringent microlayers in bulk fused silica with femtosecond laser pulses. *Opt Commun* **1999**, 171 (4-6), 279-284.
- [16]. Miura, K., Qiu, J. R., Mitsuyu, T., *et al.*, Space-selective growth of frequency-conversion crystals in glasses with ultrashort infrared laser pulses. *Opt Lett* **2000**, 25 (6), 408-410.

- [17]. Streltsov, A. M., Borrelli, N. F., Fabrication and analysis of a directional coupler written in glass by nanojoule femtosecond laser pulses. *Opt Lett* **2001**, *26* (1), 42-43.
- [18]. Zeil, P., Voigtlander, C., Thomas, J., *et al.*, Femtosecond laser-induced apodized Bragg grating waveguides. *Opt Lett* **2013**, *38* (13), 2354-2356.
- [19]. Grenier, J. R., Fernandes, L. A., Herman, P. R., Femtosecond laser writing of optical edge filters in fused silica optical waveguides. *Opt Express* **2013**, *21* (4), 4493-4502.
- [20]. Chen, H. Y., Lv, T., Zheng, A. S., *et al.*, Directly writing embedded waveguides in lithium niobate by a femtosecond laser. *Optik* **2013**, *124* (3), 195-197.
- [21]. Bricchi, E., Mills, J. D., Kazansky, P. G., *et al.*, Birefringent Fresnel zone plates in silica fabricated by femtosecond laser machining. *Opt Lett* **2002**, *27* (24), 2200-2202.
- [22]. Lancry, M., Poumellec, B., Desmarchelier, R., *et al.*, Oriented creation of anisotropic defects by IR femtosecond laser scanning in silica. *Opt Mater Express* **2012**, *2* (12), 1809-1821.
- [23]. Fan, C. X., Poumellec, B., Zeng, H. D., *et al.*, Directional Writing Dependence of Birefringence in Multicomponent Silica-based Glasses with Ultrashort Laser Irradiation. *J Laser Micro Nanoen* **2011**, *6* (2), 158-163.
- [24]. Lancry, M., Poumellec, B., Chahid-Erraji, A., *et al.*, Dependence of the femtosecond laser refractive index change thresholds on the chemical composition of doped-silica glasses. *Opt Mater Express* **2011**, *1* (4), 711-723.
- [25]. Lancry, M., Groothoff, N., Guizard, S., *et al.*, Femtosecond laser direct processing in wet and dry silica glass. *J Non-Cryst Solids* **2009**, *355* (18-21), 1057-1061.
- [26]. Poumellec, B., Lancry, M., Poulin, J. C., *et al.*, Non reciprocal writing and chirality in femtosecond laser irradiated silica. *Opt Express* **2008**, *16* (22), 18354-18361.
- [27]. Burakov, I. M., Bulgakova, N. M., Stoian, R., *et al.*, Spatial distribution of refractive index variations induced in bulk fused silica by single ultrashort and short laser pulses. *J Appl Phys* **2007**, *101* (4).
- [28]. Rajeev, P. P., Gertsvolf, M., Bhardwaj, V. R., *et al.*, Memory and nanostructure formation in the intense field ionization of fused silica. *Springer Series Chem* **2007**, *88*, 680-682.
- [29]. Eaton, S. M., Zhang, H. B., Herman, P. R., Heat accumulation effects in femtosecond laser-written waveguides with variable repetition rate. *Opt Express* **2005**, *13* (12), 4708-4716.
- [30]. Itoh, K., Watanabe, W., Nolte, S., *et al.*, Ultrafast processes for bulk modification of transparent materials. *Mrs Bull* **2006**, *31* (8), 620-625.
- [31]. Shimizu, M., Sakakura, M., Ohnishi, M., *et al.*, Mechanism of heat-modification inside a glass after irradiation with high-repetition rate femtosecond laser pulses. *J Appl Phys* **2010**, *108* (7).
- [32]. Sakakura, M., Shimizu, M., Shimotsuma, Y., *et al.*, Temperature distribution and modification mechanism inside glass with heat accumulation during 250 kHz irradiation of femtosecond laser pulses. *Appl Phys Lett* **2008**, *93* (23).
- [33]. Yu, B., Chen, B., Yang, X. Y., *et al.*, Study of crystal formation in borate, niobate, and titanate glasses irradiated by femtosecond laser pulses. *J Opt Soc Am B* **2004**, *21* (1), 83-87.
- [34]. Zhu, B., Dai, Y., Ma, H. L., *et al.*, Femtosecond laser induced space-selective precipitation of nonlinear optical crystals in rare-earth-doped glasses. *Opt Express* **2007**, *15* (10), 6069-6074.
- [35]. Dai, Y., Zhu, B., Qiu, J. R., *et al.*, Direct writing three-dimensional Ba<sub>2</sub>TiSi<sub>2</sub>O<sub>8</sub> crystalline pattern in glass with ultrashort pulse laser. *Appl Phys Lett* **2007**, *90* (18).
- [36]. Yonesaki, Y., Miura, K., Araki, R., *et al.*, Space-selective precipitation of non-linear optical crystals inside silicate glasses using near-infrared femtosecond laser. *J Non-Cryst Solids* **2005**, *351* (10-11), 885-892.

- [37]. Fan, C. X., Poumellec, B., Lancry, M., *et al.*, Three-dimensional photoprecipitation of oriented LiNbO<sub>3</sub>-like crystals in silica-based glass with femtosecond laser irradiation. *Opt Lett* **2012**, *37* (14), 2955-2957.
- [38]. Dai, Y., Ma, H. L., Lu, B., *et al.*, Femtosecond laser-induced oriented precipitation of Ba<sub>2</sub>TiGe<sub>2</sub>O<sub>8</sub> crystals in glass. *Opt Express* **2008**, *16* (6), 3912-3917.
- [39]. Dai, Y., Zhu, B., Qiu, J. R., *et al.*, Space-selective precipitation of functional crystals in glass by using a high repetition rate femtosecond laser. *Chem Phys Lett* **2007**, *443* (4-6), 253-257.
- [40]. Lin, G., Luo, F. F., He, F., *et al.*, Space-selective precipitation of Ge crystalline patterns in glasses by femtosecond laser irradiation. *Opt Lett* **2011**, *36* (2), 262-264.
- [41]. Stone, A., Jain, H., Dierolf, V., *et al.*, Multilayer aberration correction for depth-independent three-dimensional crystal growth in glass by femtosecond laser heating. *J Opt Soc Am B* **2013**, *30* (5), 1234-1240.
- [42]. Stone, A., Sakakura, M., Shimotsuma, Y., *et al.*, Formation of ferroelectric single-crystal architectures in LaBGeO<sub>5</sub> glass by femtosecond vs. continuous-wave lasers. *J Non-Cryst Solids* **2010**, *356* (52-54), 3059-3065.
- [43]. Stone, A., Sakakura, M., Shimotsuma, Y., *et al.*, Directionally controlled 3D ferroelectric single crystal growth in LaBGeO<sub>5</sub> glass by femtosecond laser irradiation. *Opt Express* **2009**, *17* (25), 23284-23289.

## Chapter 2 Theoretical background

In order to control the second-order nonlinear optical properties of material according to the precipitation of nano-crystals in glass by femtosecond laser, the basic knowledge with respect to the nonlinear optical theory and second harmonic generation, in particular, will be introduced and a general presentation about SHG in glass will be given in this chapter at first. As we know that the material possessing this nonlinear optical property can realize double frequency transfer, like BBO crystal and KDP crystal. So far, many researchers pointed out that for the transparent glassy material, the second order susceptibility  $\chi^{(2)}$  should be vanished according to its macroscopic isotropy. However, in glass-crystal composite, if crystalline phase is non-center symmetric,  $\chi^{(2)}$  of bulk glass will not be zero anymore. This point is addressed in section 2.1.2.2. Then, the classic theory regarding to the crystallization will be given to explain how to get and control the crystallization in glass. Variety of methods to achieve oriented crystallization will be shortly discussed subsequently. Afterwards, a presentation about the laser-induced modification, particularly in term of space-selectively crystallization in glass, will be delivered in general in the last section.

### 2.1 Nonlinear optical theory

#### 2.1.1 Maxwell equations in Nonlinear Media

The theoretical analysis of various optical effects in media can be carried out by use of classical Maxwell equations, given in differential form in SI units as

$$\nabla \cdot \mathbf{D} = \rho \quad (2.1.1)$$

$$\nabla \times \mathbf{E} = -\frac{\partial \mathbf{B}}{\partial t} \quad (2.1.2)$$

$$\nabla \cdot \mathbf{B} = 0 \quad (2.1.3)$$

$$\nabla \times \mathbf{H} = \mathbf{J} + \frac{\partial \mathbf{D}}{\partial t} \quad (2.1.4)$$

Here,  $\mathbf{E}$ ,  $\mathbf{D}$  are the electric field and the electric displacement, respectively. B

and  $\mathbf{H}$  are the magnetic-flux density and the magnetic field, respectively. The free charge density  $\rho$  and the free current density  $\mathbf{J}$  are two quantities related to the medium itself.

Combining with the constitutive relations mentioned above, these equations in the following can give a complete description for classical light-matter interactions in the medium:

$$\mathbf{D} = \varepsilon \mathbf{E} + \mathbf{P} \quad (2.1.5)$$

$$\mathbf{H} = \frac{1}{\mu} \mathbf{B} - \mathbf{M} \quad (2.1.6)$$

The electric polarization  $\mathbf{P}$  and the magnetization  $\mathbf{M}$  describe the material response to external electro-magnetic perturbations.  $\varepsilon$  is the permittivity and  $\mu$  the permeability tensors of the material. Even the linear case can have various complications, however. For homogeneous materials,  $\varepsilon$  and  $\mu$  are constant throughout the material, while for inhomogeneous materials they depend on location within the material (and perhaps time). For isotropic materials,  $\varepsilon$  and  $\mu$  are scalars, while for anisotropic materials because of the crystal structure, they are tensors. Generally speaking, materials are dispersive, so  $\varepsilon$  and  $\mu$  depend on the frequency of any incident electric-magnetic (EM) waves.

Now, taking the curl  $\nabla \times \mathbf{E}$  of the curl equations, and using the identity  $\nabla \times (\nabla \times \mathbf{E}) = \nabla(\nabla \cdot \mathbf{E}) - \nabla^2 \mathbf{E}$  (with  $\nabla \cdot \mathbf{E} \equiv 0$  in neutral medium) we obtain the approximated plan-wave equations with combining equations from Eq. (2.1.1) to (2.1.6):

$$\nabla^2 \mathbf{E} - \frac{1}{c^2} \frac{\partial^2 \mathbf{E}}{\partial t^2} = \frac{\partial}{\partial t} (\mu \mathbf{J} + \nabla \times \mathbf{M}_1) + \mu \frac{\partial^2 \mathbf{P}_1}{\partial t^2} \quad (2.1.7)$$

$c$  here is the speed of light in free space. The Eq. (2.1.7) is an inhomogeneous wave equation with the electric polarization  $\mathbf{P}_1$ , the magnetization  $\mathbf{M}_1$ , and the current density  $\mathbf{J}$  as its source terms.

As a matter of fact, in Eq. (2.1.7), the various multipolar currents can be absorbed in their respective sources. For instance, the current density  $\mathbf{J}$  can be expressed via conductivity as a loss source in the medium. Then, it needs the expansion of electric polarization  $\mathbf{P}$  and magnetization  $\mathbf{M}$  in terms of their higher

spatial orders:

$$\nabla^2 \mathbf{E} - \frac{1}{c^2} \frac{\partial^2 \mathbf{E}}{\partial t^2} = \nabla \times \frac{\partial}{\partial t} (\mathbf{M}_2 + \dots) + \mu \frac{\partial^2}{\partial t^2} (\mathbf{P}_2 + \nabla \cdot \mathbf{Q} + \dots). \quad (2.1.8)$$

Here,  $\mathbf{M}_2$ ,  $\mathbf{P}_2$  and  $\mathbf{Q}$  are dipolar magnetization, dipolar electric polarization, and electric quadrupolarization, respectively, which are the components of effective second-order nonlinear polarization in medium. In metallic nanoparticles containing glass, both electric polarization and quadrupole contributions to hyper Rayleigh scattering (HRS) of second harmonic responses have been discussed involving a size range of metallic particles<sup>[1]</sup>. Here, we pay more attention on the oxide crystals containing glass and focus the discussion on the dipolar electric polarization who should be the dominate contributor of second harmonic generation in glass ceramic materials. We note dipolar electric polarization as  $\mathbf{P}$  without the subscript 2 subsequently. Hence, for the purpose of current introductory discussion here, we can use

$$\nabla^2 \mathbf{E} - \frac{1}{c^2} \frac{\partial^2 \mathbf{E}}{\partial t^2} = \mu \frac{\partial^2 \mathbf{P}}{\partial t^2} \quad (2.1.9)$$

Here the electric field is driven by the electric dipole polarization which can induce the dipole current also.

## 2.1.2 Nonlinear optical phenomenon in material

### 2.1.2.1 Second Harmonic Generation (SHG)

The wave Eq. (2.1.9) can be translated in the Fourier domain and we get:

$$\nabla^2 \mathbf{E}(\omega) - \frac{\omega^2 \varepsilon(\omega)}{c^2} \mathbf{E}(\omega) = \frac{\omega^2}{c^2} \mathbf{P}^{(NL)}(\omega) \quad (2.1.10)$$

$\varepsilon$  is the linear permittivity of the medium, or so-called dielectric constant. This equation thus describes the wave that will be yielded from the nonlinear polarization.

For very intense light, the relation between polarization and electric field is no longer linear<sup>[2-3]</sup>. In this nonlinear regime, the polarization is expanded in a Taylor

series in terms of the total applied electric field. The linearity of Maxwell's equations allows each frequency component to dispose separately. Then we can obtain

$$\begin{aligned}
 \mathbf{P}(\omega) &= \mathbf{P}^{(1)}(\omega) + \mathbf{P}^{(2)}(\omega) + \mathbf{P}^{(3)}(\omega) + \dots \\
 &= \epsilon_0 \chi^{(1)}(\omega) \cdot \mathbf{E}(\omega) \\
 &+ \epsilon_0 \chi^{(2)}(\omega = \omega_1 + \omega_2) : \mathbf{E}(\omega_1) \mathbf{E}(\omega_2) \\
 &+ \epsilon_0 \chi^{(3)}(\omega = \omega_1 + \omega_2 + \omega_3) : \mathbf{E}(\omega_1) \mathbf{E}(\omega_2) \mathbf{E}(\omega_3) \\
 &+ \dots
 \end{aligned} \tag{2.1.11}$$

$$= \mathbf{P}^{(L)}(\omega) + \mathbf{P}^{(NL)}(\omega) \tag{2.1.12}$$

$$= \mathbf{P}^{(1)}(\omega) + \sum \mathbf{P}^{(n)}(\omega) \tag{2.1.13}$$

The Eq. (2.1.11) can be grouped into two parts, linear and nonlinear part, as shown by Eq. (2.1.12) or Eq. (2.1.13). Here  $\mathbf{P}^{(n)}(\omega)$  is the  $n$ th order electric-dipole polarization and  $\chi^{(2)}$  and  $\chi^{(3)}$  are the second- and third-order susceptibilities, characterizing the nonlinear optical response of the medium.

Here,  $\chi^{(2)}$  is a tensor of rank 3. It contains 27 components and can be represented by a  $3 \times 3 \times 3$  matrix which is related to the symmetry properties of material. Actually, it can be easily seen that  $\chi^{(2)}$  is responsible for second-order nonlinear optical effects. Hence, due to the nonlinear interaction, an additional frequency independent term and a term at the double frequency arise. The first one is called optical rectification (OR) and frequency doubling is named second harmonic generation (SHG). More generally, if we use two input fields at different frequencies, for example  $\omega_1$  and  $\omega_2$ , terms at  $\omega_1 + \omega_2$  appears in addition to SHG and OR contributions, representing sum-frequency and difference-frequency generation, respectively.

In case of SHG, we assume that the input plane waves are monochromatic with frequency  $\omega_1 = \omega$  and harmonic waves  $\omega_2 = 2\omega$ .  $n_\omega$  is the refractive index of material at fundamental wave while  $n_{2\omega}$  is that at second harmonic waves. It is assumed that no free charge  $\rho$  and no free current  $\mathbf{J}$  are contained in the medium. Consistent with the assumption of a cubic crystal or a special geometry,  $\epsilon$  will be taken as a scalar. Moreover, the temporal variation of electric field at  $\omega$  and  $2\omega$  are neglected. Thus, waves at the second harmonic frequency will obey the wave equation

$$\nabla^2 \mathbf{E}(2\omega) - \frac{\omega^2 \epsilon(2\omega)}{c^2} \mathbf{E}(2\omega) = \frac{\omega^2}{c^2} \mathbf{P}^{(2)}(2\omega) \tag{2.1.14}$$

Where

$$\mathbf{P}^{(2)}(2\omega) = \epsilon_0 \chi^{(2)}(-2\omega; \omega, \omega) : \mathbf{E}(\omega) \mathbf{E}(\omega) \quad (2.1.15)$$

With  $\mathbf{E}(\omega) = \hat{e}_1 \cdot E_\omega \cdot e^{i\bar{k}_1 \bar{r}}$  and  $\mathbf{E}(2\omega) = \hat{e}_2 \cdot E_{2\omega} \cdot e^{i\bar{k}_2 \bar{r}}$

$\hat{e}_1, \hat{e}_2$  : Unite vectors of electric fields;

$\bar{k}_1, \bar{k}_2$  : Wave vectors, with  $k_1 = (n_\omega/c)\omega$  and  $k_2 = (n_{2\omega}/c)2\omega$ .

$E_\omega, E_{2\omega}$  : Amplitudes of fundamental electric field and second harmonic electric fields, respectively;

It is important to note that this is the usual linear wave equation augmented by a source tem on the right-hand side. If we recall the equation (2.1.14), the general solution of  $\mathbf{E}$  and  $\mathbf{H}$  consists of the solution of homogeneous equation plus one particular solution of the inhomogeneous equation. The magnitude of the reflected and transmitted amplitudes can be determined from the Fresnel's law and boundary conditions<sup>[4]</sup>. The intensity of second harmonic waves can be obtained through a nonlinear medium with thickness  $L$  with supposing that the intensity of fundamental beam is constant and the incident beam is normal to the entry surface of material<sup>[5]</sup>,

$$I_{2\omega}(L) = \frac{(2\omega)^3}{8\epsilon_0 c^3} \frac{|\chi^{(2)}|^2}{n_\omega^2 n_{2\omega}} \cdot I_\omega^2 \cdot L^2 \cdot \frac{\sin^2((2k_1 - k_2) \cdot L/2)}{((2k_1 - k_2) \cdot L/2)^2} \quad (2.1.16)$$

With  $I_\omega = \frac{1}{2} \epsilon_0 c n_\omega |E_\omega|^2$  and  $I_{2\omega} = \frac{1}{2} \epsilon_0 c n_{2\omega} |E_{2\omega}|^2$

After this equation, the intensity of second harmonic is modulated by the difference of two assumed collinear wave vectors,  $2\bar{k}_1$  and  $\bar{k}_2$ . We define that:

$$\Delta k = 2k_1 - k_2 = 2\omega(n_\omega - n_{2\omega})/c \quad (2.1.17)$$

This parameter  $\Delta k$  determines the phase matching conditions.

### 2.1.2.2 Symmetries in second-order nonlinear optics

Indeed, the spatial symmetry of the susceptibility tensors reflects the structural properties of the nonlinear medium. For a coherent center symmetric system, since center symmetry operation leave the sign and magnitude of physical properties unchanged,  $\chi^{(2)}$  is zero. It results in null SHG when incident beam is normal to the

entry surface. Therefore, all tensor components  $\chi_{ijk}^{(2)}$  are null and no second-order nonlinear optics effects are observe. For non center symmetric crystals, the number of independent components of  $\chi^{(2)}$  that are nonzero is completely determined by symmetry which can be written as

$$P_i^{(2)}(2\omega) = \sum_{j,k} \chi_{ijk}^{(2)} E(\omega)_j E(\omega)_k \quad (2.1.18)$$

Where the subscripts  $ijk$  refer to Cartesian coordinates in the laboratory frame.  $P_i^{(2)}$  is a component of the polarization vector,  $E_i$  are components of the electric field vector. The second-order susceptibility tensor is preferentially described as a rectangular  $3 \times 9$  matrix. Actually, after Kleinman<sup>[6]</sup> has formulated the relation between components of  $\chi_{ijk}^{(2)}$ , interchanging the indices  $j$  and  $k$  in (2.1.17) leaved the expression unchanged. This intrinsic permutation symmetry allows the nonlinear susceptibility tensor to be written as a  $3 \times 6$  matrix  $d_{il}$ . It should note that for SHG, the tensor  $d_{il}$  is often used instead of the tensor  $\chi_{ijk}^{(2)}$ , two tensors being linear relationship  $d_{il} = (1/2) \chi_{il}^{[7]}$ .  $i=1=xx$  corresponds to the x axis,  $i=2=yy$  to the y axis,  $i=3=zz$  to z axis,  $4=yz=zy$ ,  $5=xz=zx$  and  $6=xy=yx$ .

The polarization components can be written as

$$P_i^{(2)}(2\omega) = \chi_{ijk}^{(2)} E(\omega)_j E(\omega)_k = 2d_{ijk}^{(2)} E(\omega)_j E(\omega)_k$$

$$\begin{bmatrix} P_x^{(2)}(2\omega) \\ P_y^{(2)}(2\omega) \\ P_z^{(2)}(2\omega) \end{bmatrix} = 2 \begin{bmatrix} d_{11} & d_{12} & d_{13} & d_{14} & d_{15} & d_{16} \\ d_{21} & d_{22} & d_{23} & d_{24} & d_{25} & d_{26} \\ d_{31} & d_{32} & d_{33} & d_{34} & d_{35} & d_{36} \end{bmatrix} \begin{bmatrix} E(\omega)_x^2 \\ E(\omega)_y^2 \\ E(\omega)_z^2 \\ 2E(\omega)_y E(\omega)_z \\ 2E(\omega)_x E(\omega)_z \\ 2E(\omega)_x E(\omega)_y \end{bmatrix} \quad (2.1.19)$$

A scalar effective d coefficient is obtained by finding the projection of the nonlinear polarization onto a chosen direction defined by the unit vector of plane wave at second harmonic frequency  $\hat{e}_2$ , giving

$$P^{(2)}(2\omega) = 2d_{eff} E(\omega)^2 \quad (2.1.20)$$

Where  $d_{eff} = \hat{e}_2 \cdot d : \hat{e}_1 \hat{e}_1$  and  $E(\omega)^2 = E(\omega)_x^2 + E(\omega)_y^2 + E(\omega)_z^2$

### 2.1.2.3 Discussion about phase matching conditions

In the nonlinear medium, the incident wave induces a coherent oscillation of dipoles of this medium. This results in a reflected wave in air at  $2\omega$  and two harmonic waves in the medium. One of harmonic waves propagates following the direction of wave vector of refracted fundamental ray which is called as bound wave [8]. This effective nonlinear wave is of frequency  $2\omega$  and wave vector is twice the wave vector of the refracted fundamental ray  $2\vec{k}_1$ . This wave is the peculiar solution of the inhomogeneous propagation equation which contains the source term with the non-linear polarisation. The wave vector  $\vec{k}_2$  corresponds to free harmonic wave that travels with velocity  $c/n_{2\omega}$  and is different from the bound wave (i.e.  $c/n_\omega$ ). It is the general solution of the homogeneous equation. These two waves at frequency  $2\omega$  interfere if both wave vector are close to be parallel.

#### Phase matching condition

The phase matching can be achieved when both free and bound waves are synchronized in phase to optimize the transferred energy to second harmonic waves. Thus, this condition is possible if  $\Delta k = 2k_1 - k_2 = 2\omega(n_\omega - n_{2\omega})/c = 0$  with  $n_\omega = n_{2\omega}$  and assuming that vectors  $\vec{k}_1$  and  $\vec{k}_2$  are collinear.

These conditions are achievable for birefringent crystals whose refractive index depends on the propagation and polarization direction of beam rays. For instance, in a negative uniaxial birefringent crystal, two refractive indexes exist: ordinary index  $n_o$  and extraordinary  $n_e$ . Therefore, the phase matching condition becomes achievable for that incident waves  $\omega$  and harmonic waves  $2\omega$  propagate in the same direction, if the oscillating field at  $\omega$  has an ordinary propagation while oscillating field at  $2\omega$  has an extraordinary propagation such as  $n_{o(\omega)} = n_{e(2\omega)}$  [9-10]. The solution of this problem can be represented schematically as below:

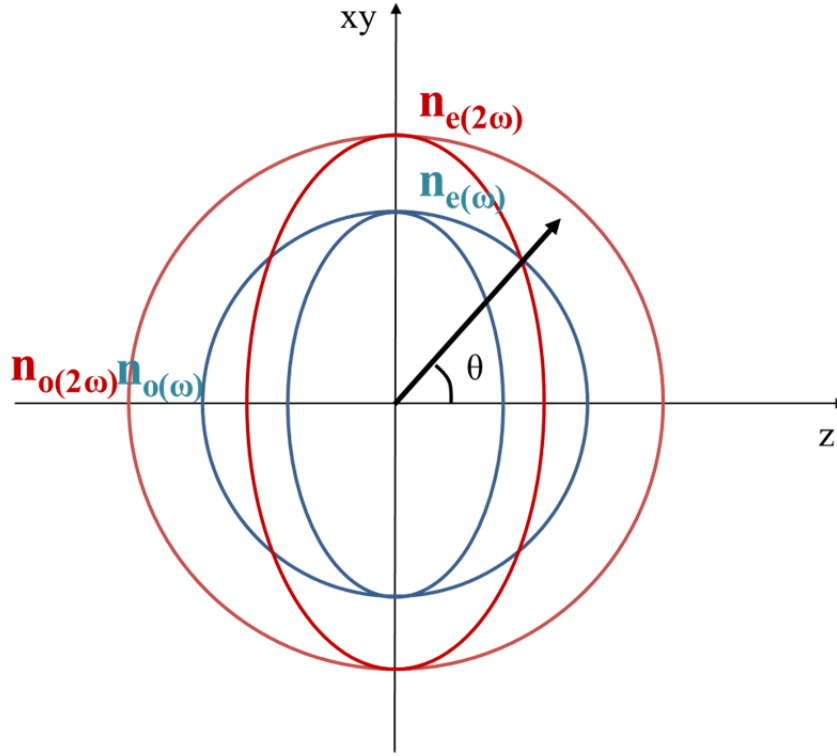


Figure 2.1 Index surface of fundamental wave (blue) and second harmonic wave (red) of a negative uniaxial crystal. The angle  $\theta$  indicate the propagation direction of waves for phase matching with respect to the  $z$  axis of crystal.

### Quasi-Phase matching condition

However, in dispersive and transparent medium, as glassy materials, the refractive indices are different over the energy range from  $\omega \rightarrow 2\omega$ . The phase matching can't be realized in this mechanism. Because of interference, the amplitude of  $I_{2\omega}$  oscillates during its travelling as shown by Eq. (2.1.16).

We introduce the definition of coherent length  $l_c$  as  $l_c = |\pi / \Delta k|$ . It is accumulation of phase shift between the nonlinear polarization and the harmonic free wave. The harmonic intensity  $I_{2\omega}$  is built in terms of a coherent length  $l_c$ . The Eq. (2.1.16) can be rewritten as

$$I_{2\omega}(L) = \frac{(2\omega)^3}{8\epsilon_0 c^3} \frac{|\chi^{(2)}|^2}{n_\omega^2 n_{2\omega}} \cdot I_\omega^2 \cdot L^2 \cdot \frac{\sin^2(\pi L / 2l_c)}{(\pi L / 2l_c)^2} \quad (2.1.21)$$

Therefore, by varying the length of optical path  $L$ , the interference fringes are observable in case of  $L \gg l_c$ . Regarding to the problem of phase mismatching and envelope of fringes obtained with a  $L$ , one solution has been reported by Armstrong et al.<sup>[11]</sup>. They interpreted that if the thickness of medium equals to the coherent length, a quasi-phase matching can be achieved and constructive interference should be considered.

In general, the most used materials for this phase matching or quasi-phase matching process and for the phenomenon of second harmonic generation are inorganic crystals, such as  $\text{LiNbO}_3$ ,  $\text{LiTaO}_3$ , KDP ( $\text{KH}_2\text{PO}_4$ ) and KTP ( $\text{KTiOPO}_4$ ). However, the problems of these materials for applications in second-order nonlinear optics or especially in second harmonic generation exist in their difficulties. For example, the high cost of fabrication and difficulties for the development of large optical components block their widely usage in nonlinear optics. The next section will present the methods used to induce second-order nonlinear optical properties in vitreous materials.

### **2.1.3 SHG in glasses**

Glass is an amorphous solid with a glass transition temperature noted  $T_g$ . One of its characteristics is that it does not possess long-range order. Its structural character-center symmetric-does not allow it to be used as a double frequency or any other second-order nonlinear optical property. However, there are various techniques to break its center symmetry. Two main techniques are used frequently: thermal polarization (so-called thermal poling) and crystallization of non-center symmetric crystals in glass.

#### **2.1.3.1 Thermal polarization**

One of the techniques to break the center symmetry of glass is thermal polarization or thermal poling. This technique consists of an electric field applied to both sides of a sample at high temperature. The system is then cooled down to room temperature under electric field in order to freeze the adopted configuration, and then the field is moved. A SHG signal obtained in glass by thermal polarization has

discovered by Myers in 1991<sup>[12]</sup>. The origin of SH in glassy material subjected to thermal poling is still under discussed since two mechanisms have been proposed: one is in terms of charge migration and the other one is about the reorientation of dipoles.

The former mechanism claims that thermal poling induces mobile ions migrating to the cathode (light cations such as  $\text{Na}^+$ ) to weaken the applied electric field during this treatment. It forms a depletion region negatively charged at anode side. This results in a DC electric field  $E_{\text{dc}}$  of the order  $10^7 \text{V/cm}$ . It should note that this charged region is a narrow zone below the anode surface (several microns) and perpendicular to the surface<sup>[12-13]</sup>. Therefore, the isotropy of glass is broken because of this strong electrostatic field  $E_{\text{dc}}$ , and effective second-order susceptibility  $\chi_{\text{eff}}^{(2)}$  can be obtained through a coupling between third-order susceptibility  $\chi^{(3)}$  and internal electrostatic field  $E_{\text{dc}}$  which is  $\chi_{\text{eff}}^{(2)} = 3\chi^{(3)} \times E_{\text{dc}}$ <sup>[12]</sup>. The second mechanism, proposed by Mükherjee<sup>[14]</sup>, is based on the hypothesis of a directional reorientation and a Boltzmann static of hyper-polarizable polar entities under the effect of local field  $E_{\text{loc}}$ . Its second-order susceptibility can be expressed as  $\chi^{(2)} \propto \beta\mu E_{\text{loc}}$  with dipole moment  $\mu$  and hyper-polarizability  $\beta$ <sup>[14-15]</sup>.

So far, after Myers studies, so many researchers continued their investigations in fused silica<sup>[16]</sup> and focused on the effect of thermal polarization conditions on the value of second-order nonlinear susceptibility in silicate glass. For instance, the influence of applied tension and temperature<sup>[17-19]</sup>, of atmosphere<sup>[20]</sup>, of induced structural defaults or of the addition of group OH<sup>[21]</sup>, on the efficient of SHG and poling mechanism have been studied in kinds of silicate glass. They found that the intensity of SHG was increased with increased OH concentration of OH and gave an optimum thermal condition to obtain the largest SHG intensity in fused silica<sup>[21]</sup>.

However, it is reported that the maximum thickness of polarized layer possessing second-order nonlinear properties is about  $40 \mu\text{m}$  through thermal poling method<sup>[22-30]</sup>. Although Quiquempois et al<sup>[31]</sup> obtained the second-order susceptibility at  $163 \mu\text{m}$  under sample surface in Suprasil silica and Xu et al<sup>[32-34]</sup> pointed out the possibility of a thicker nonlinear layer about  $250\text{-}300 \mu\text{m}$  can be possessed in  $\text{PbO-B}_2\text{O}_3$  glass but with weak SHG intensity, there is nearly rare evident proofs to

show that the possibility of stable and strong SHG signals in volume using thermal poling method. On this point of view, more attention has been focused on the second method that is to get crystallization of non-center symmetric crystals in glass.

### **2.1.3.2 Crystallization of glass-ceramic**

The traditional method to obtain glass-ceramic is to control the cooling step during glass fabrication by melt-quenching method or is to apply an additional treatment on the prepared homogeneous glass. For instance, it has reported that glass ceramic can be achieved not only by heat treatment, but also using laser irradiation or accompanied heat treatment. There is a widely application of glass-ceramics in our daily life, so far. For example, glass-ceramics can increase the mechanical strength of the original glass material<sup>[35]</sup> and they are often used for dental prostheses or bone reconstruction because of their good mechanical properties and zero porosity<sup>[36]</sup>. Moreover, a lower coefficient of expansion than that of glass brings them good thermomechanical properties in application of cooking and ovens.

Indeed, regarding to their nonlinear optical properties, the final properties of material depend on the precipitated crystalline phase in glass. Komatsu et al. reported for the first time that it was possible to incorporate non-center symmetric crystals in a glass matrix<sup>[37]</sup> and this started the new application in aspect of nonlinear optics. Through this method, the second-order nonlinear optical properties, as SHG, can be induced by the presence of nonlinear crystals<sup>[38-41]</sup>. In addition, when the crystallization is controlled, glass-ceramics can be elaborated in keeping good quality of transparency. But in practice, transparency is too difficult to control due to different origins of diffusion loss. It is demonstrated that the diffusion loss is in terms of the crystallite size and the transparency of material containing particles should obey these two criteria<sup>[42-43]</sup>: the particle size should much smaller than wavelength and diffusion can be reduced as a type of Rayleigh diffusion with small intensity; the index difference between crystalline particles and matrix should be minimized. The fabricate glass-ceramic should satisfy one of these two criteria to be transparent. However, aiming for a nonlinear crystal phase and to generate nonlinear optical properties, the size of particles must be large enough (about 100nm)<sup>[44]</sup>.

Indeed, metallic particles containing glass possessing second-order nonlinearities has drawn attention of various research groups from the report by<sup>[45]</sup>. They pointed out that the symmetry of the crystalline structure of the material and of the shape and size of metallic particles plays an essential role in determining the nature and the intensity of the SH response. A volume dependence has been observed due to multipolar effects or field retardation for large gold particles typically above a diameter of about 40nm<sup>[46-47]</sup> Moreover, it has been figured out that the SHG signals arise from defects presenting at the surface of the particle<sup>[48]</sup> cannot be avoided because of imperfect fabrication processes.

Compared those uncertain elements in metallic particles containing glass, the precipitated non center symmetric crystals directly from silicate glassy matrix to induce the second-order optical nonlinear properties is the focus of this thesis. Detailed conditions of crystallizations to obtain the desired crystal phase, the controlled shape and size of crystals will be investigated in the following chapters. Firstly, the classic theory with respected to thermodynamics and kinetic studies of crystallization will be discussed in the next section.

## **2.2 Mechanism of crystallization in glass**

It is known that three general states of matter-gaseous, liquid and solid-represent very different degrees of atomic or molecular mobility. In the solid state, material may be crystalline or amorphous, and the crystalline state differs from the amorphous state in the regular arrangement of the constituent molecules, atoms or ions into some fixed and rigid pattern known as a lattice which results in peculiar chemical and physical properties. In this part, we will study the thermodynamic and kinetics theories of nucleation and crystallization to understand the phase separation and transformation from amorphous to crystalline, especially in glass material.

### **2.2.1 Basic theory of crystallization in glass**

The crystallization of a homogeneous phase begins and extent from dispersive centers in the bulk glass. Two steps are distinguished: the nucleation and the crystal growth.

Nucleation can often be induced by agitation, mechanical shock, friction and extreme pressures within solutions and melts. In the aspect of thermal agitation, the nucleation (or germination) is usually formed when increasing the applied temperature. It is reported that those particles in the glass must reach a critical size to form a nuclei or a germ as a depart point to obtain and develop crystals in the ordered region<sup>[49]</sup>. If the probabilities of forming a germ are identical either in bulk or on the surface in the aspect of chemical, structural or energetic environment, we call this homogeneous nucleation which is a spontaneous formation process in the system which has been reviewed by Fokin et al.<sup>[50]</sup>. However, the perfect homogeneous nucleation is too difficult to realize because of the impurity in the glass or the density fluctuation originated from technical limits during the glass fabrication. The existence of the defaults could decrease the energy of forming one germ in the system. In this case, the nucleation is called heterogeneous nucleation. The generated stable germs in glass will growth with the addition of surrounding atoms to obtain a particular crystalline phase. This process is named as crystal growth.

### 2.2.1.1 Homogeneous nucleation

This is Gibbs theory. It is a first step i.e. a basic understanding for approaching the problem but other more complex models closer to actual mechanism for accounting for the crystallization more quantitatively.

The phase transformation is accompanied with minimizing Gibbs free energy  $G$ . When the temperature  $T$  of the material is higher than  $T_m$  (melting temperature), the equilibrium phase corresponds liquid phase with a lower free energy and the crystallized state is not stable anymore. When  $T < T_m$ , the solid crystalline phase owns a lower energy than supercooling liquid and it becomes a stable phase. As we know, in supercooled liquid, the variation of free energy per volume unit ( $\Delta G_v$ , the subscripted small letter  $v$  represents free energy per volume unit while the capital letter  $V$  in  $\Delta G_V$  represents the volume free energy for a macroscopic volume) associated with the liquid-crystal transformation can be expressed in function of the change of volume enthalpy  $\Delta H_v = -L_v < 0$  (with  $L_v$  is latent heat), and of the associated change of entropy  $\Delta S_v$ .

$$\Delta G_v = \Delta H_v - T\Delta S_v \quad (2.2.1)$$

We consider that  $\Delta H_v$  is a constant corresponding to the release heat during the crystallization. If at melting temperature  $T_m$ , the  $\Delta G_v$  equals to zero because both the crystal and liquid have the same free energy. Therefore, the expression above can be transferred as:

$$\Delta G_v = -\Delta H_v \left( \frac{\Delta T}{T_m} \right) \quad (2.2.2)$$

Here, we call  $\Delta T$  is the degree of supercooling as  $\Delta T = T - T_m$ . The necessary condition for phase transformation is  $\Delta G_v < 0$ .

The overall excess free energy between a solid germ and the liquid (assumed as a sphere with radius  $r$ ),  $W$ , is equal to the sum of the surface excess free energy  $\Delta G_S$ , i.e. the excess free energy between the surface of the particle and the bulk of the particle, and the volume excess free energy,  $\Delta G_V$ , i.e. the excess free energy between a very large particle and liquid.  $\Delta G_S$  is a positive quantity, the magnitude of which is proportional to  $r^2$  while  $G_V$  is a negative quantity proportional to  $r^3$ .

$$W = \Delta G_s + \Delta G_v = 4\pi r^2 \gamma + (4\pi / 3)r^3 \Delta G_v \quad (2.2.3)$$

Here,  $\gamma$  is the interfacial tension between the developing crystalline surface and the solution where it is located.

The two terms on the right-hand side of Eq. (2.2.3) are of opposite sign and depend differently on  $r$ . Therefore, the free energy of formation curve can be obtained as shown in figure (2.2). The maximum value  $W_c$ , corresponds to the critical nucleus  $r_c$  with setting  $dW/dr=0$ . We can get that the  $r_c$  and the free energy  $W_c$  at  $r_c$  can be expressed as

$$r_c = \frac{-2\gamma}{\Delta G_v} \quad (2.2.4)$$

$$W_c = \frac{16\pi\gamma^3}{3\Delta G_v^2} \quad (2.2.5)$$

Where  $\Delta G_v$  is a negative quantity. The minimum energy to form a stable germ barrier  $W_c$  (noted as  $W_{crit}$  in the following figure) is called thermodynamic barrier of nucleation.

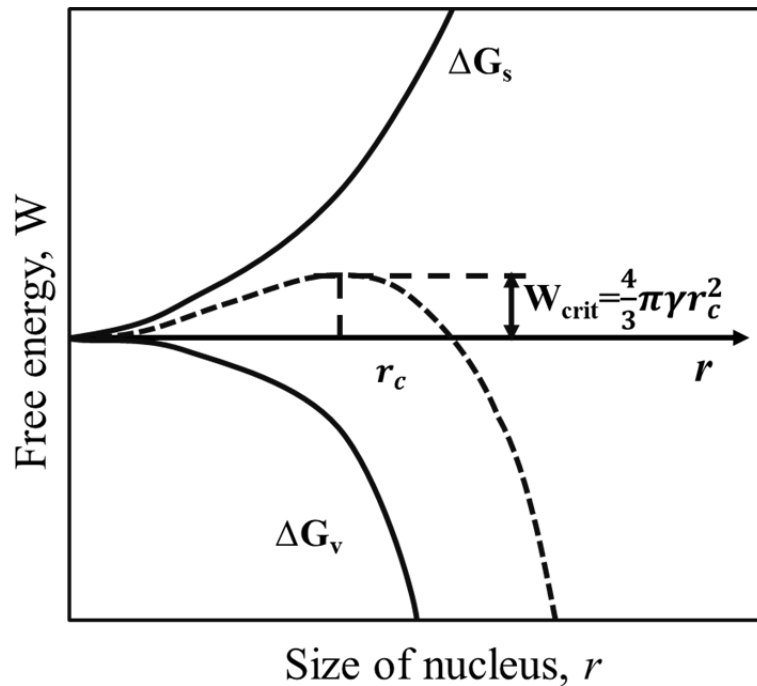


Figure 2.2 Free energy diagram for nucleation with the existence of a “critical nucleus”

From figure 2.2, it shows that the behavior of a newly crystalline lattice structure in a supercooling solution depends on its size. The contribution of surface is predominant in case of small clusters while the contribution of volume effects in major part with the increase of  $r$  and it allows decreasing the required energy for germs formation. The critical size  $r_c$ , therefore, represents the initial clusters to become germs in or the minimum size of a stable nucleus. Particles smaller than  $r_c$  will dissolve to achieve a reduction in its free energy and particles larger than  $r_c$  will continue to grow.

### 2.2.1.1.1 Nucleation rate

In order to evaluate the rate of homogeneous nucleation, two aspects of the nucleation should be considered. Indeed, the thermodynamic barrier to overcome so that the embryo can form a stable seed is to be considered with taking into account the energy potential of the material. The seed formation rate concerning to the atoms diffusion towards the crystal surface in the medium brings us the information about the kinetic factor in the nucleation process which is related to the activation energy.

Consider the relation between the number of embryo  $N_c$  with radius  $r_c$  per volume and the total number of molecules  $N$  per volume:

$$N_c = N \exp\left(-\frac{W_c}{k_B T}\right) \quad (2.2.6)$$

The formation of an embryo into a seed with critical size  $r_c$  is the result of atomic diffusion. The formation rate of these germs is then defined by the number of seeds  $N_c$  at critical size and the rate of agglomeration of molecules on the seed. The atoms diffusion is conditioned by the germ-matrix interface crossing which can be regarded as a diffusion layer. Thus, the rate  $I$  of forming nuclei at a critical size is given by:

$$I = K \exp\left(-\frac{\Delta G_D}{k_B T}\right) \times N \exp\left(-\frac{W_c}{k_B T}\right) \rightarrow I \propto \exp\left(-\frac{\Delta G_D + W_c}{k_B T}\right) \quad (2.2.7)$$

$k_B$  is the Boltzmann constant and  $\Delta G_D$  is the required activation energy to cross the glass-crystal interface and represents the kinetic barrier of reaction.

In the case of non-reconstructive transformations, or of the crystallization happening without the composition change,  $\Delta G_D$  can be written in terms of the diffusion coefficient  $D$  of supercooling liquid. This coefficient connects to the viscosity  $\eta$  with applying Stokes-Einstein relation:

$$D = \frac{k_B T}{3\pi d_\lambda \eta} \quad (2.2.8)$$

$d_\lambda$  is the diameter of the diffusing species ( $\sim 2$  times of the ionic radius).

In the system with several components that gives rise to reconstructive transformation during crystallization, the specie that diffuses much slowly limits the diffusion velocity and  $\Delta G_D$  could be regarded as the activation energy of this specie. Moreover, figure 2.3 interprets the effect of temperature on the size and free energy of formation of a critical nucleus and relation between the degree of supercooling and the nucleation rate. At low degree of supercooling ( $\Delta T \sim 0$ ), the activation barrier is high (shown in figure 2.3(a)) and will play as a dominative role and the nucleation rate is very low. When the temperature is close to  $T_g$  (Transition temperature of glass), the  $W_c$  decreases and nucleation rate  $I$  increases sharply. It might reach a maximum when  $W_c$  and  $\Delta G_D$  are the same order of magnitude. Then, when  $\Delta T$  increases, the probability of forming seeds increases ( $W$  decreases further) but the viscosity increases sharply which restricted atom movement and inhibited the formation of ordered crystal structures. This could induce the decrease of the nucleation rate. Based on the discussion above, the schematic relation among degrees of supercooling, the volume free energy and the size of critical nucleus is shown as following:

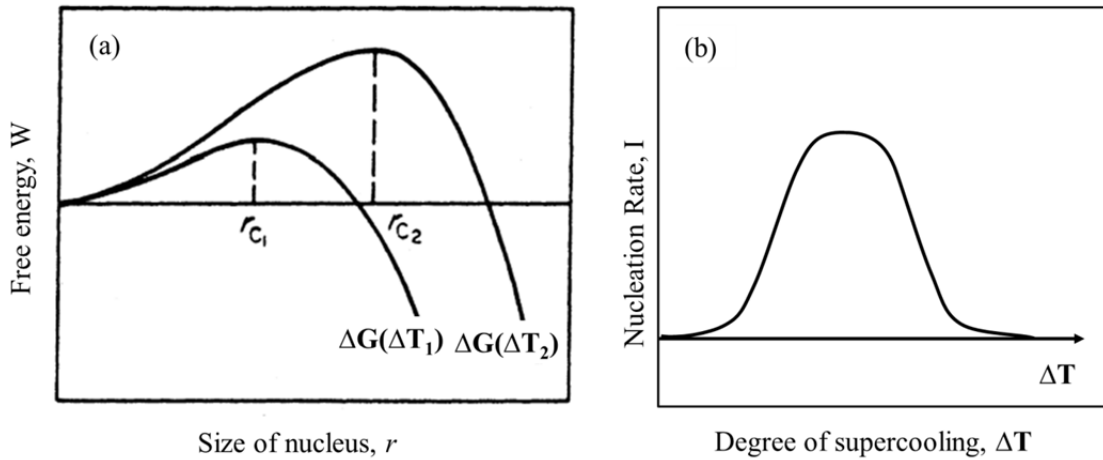


Figure 2.3 (a) Effect of temperature on the size and free energy of formation of a critical nucleus ( $\Delta T_1 > \Delta T_2$ ). (b) Relation between the degree of supercooling and the nucleation rate.

### 2.2.1.2 Heterogeneous nucleation

When calculating the nucleation rate, we have assumed that the nucleation phenomenon was homogeneous which means no difference existed in the sample. Indeed, this process is too difficult to be realized. Most of phase transformation is completed with the existence of foreign bodies in glass (preferential sites for crystallization) and is produced at the interface between the glass phase and solid substrate. The thermodynamic barrier of heterogeneous nucleation process is less or the same as that of homogeneous process. It depends on the contact angle  $\theta$  between the interfaces of crystalline surface, solid surface and liquid.

### 2.2.1.3 Crystal growth

As soon as stable nuclei, i.e. particles larger than the critical size, have been formed in supercooled system, they begin to grow into crystals of visible size. The many proposed mechanisms of crystal growth have been broadly discussed before. The surface energy theories are based on the postulation that the shape of a growing crystal is such that surface energy is minimized and showed that the equilibrium shape of a crystal is related to the free energies of the faces<sup>[51]</sup>. It is also suggested

that the crystal faces would grow at rates proportional to their respective surface energies. Another series of widely used theories, such as adsorption layer theories and the diffusion theories, has been posed after then. Among them, the diffusion theories presume that matter is deposited continuously on a crystal face at a rate proportional to the difference in concentration between the point of deposition and the bulk of the solution. Berthoud<sup>[52]</sup> suggested that there were two steps in the mass deposition, viz. a diffusion process, whereby solute molecules are transported from bulk of the fluid phase to the solid surface, followed by a first-order “reaction” when the solute molecules arrange themselves into the crystal lattice. The driving forces for diffusion and reaction were considered in diffusion-reaction mode. However, whatever it is homogeneous nucleation or heterogeneous, in point of thermodynamic consideration, this crystal growth process depends on the crystal growth rate and of which the free energy can extract from the supercooled liquid system.

Generally speaking, if the growth is continuing, all the sites of the adsorption layer of crystal are identical. The crystallization was assumed as the reverse of dissolution. During the crystal growth process, atoms will depart from the liquid and break the links with their neighbors. The velocity of absorbing an atom ( $\Delta G_D$ ) transferred from liquid to crystal  $v_{lc}$  and of detachment of an atom ( $\Delta G_D - \Delta G_v$ ) from crystal to liquid  $v_{cl}$  should be considered as shown in figure 2.4.

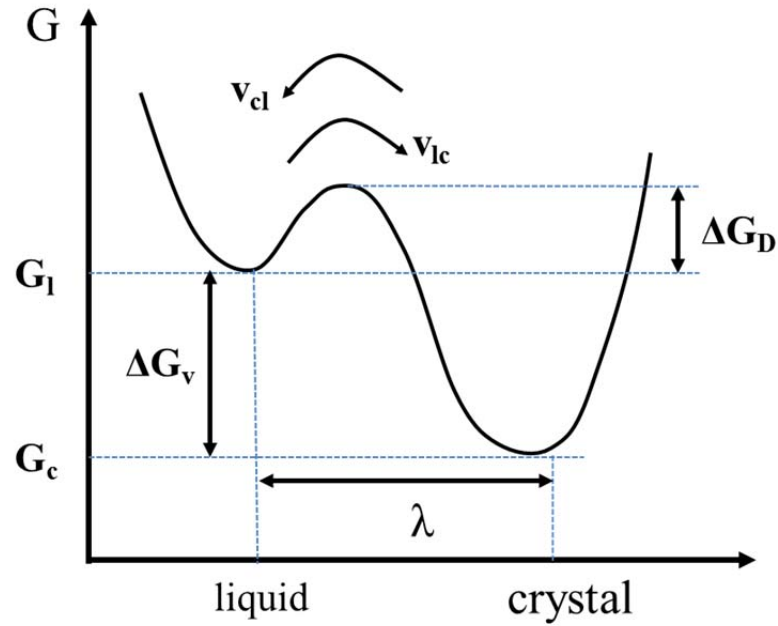


Figure 2.4 kinetic of crystal growth

We find that it is more difficult to decomposed atoms from solid to liquid because of larger energy barrier. Therefore, the atom on the crystal surface will resist to the melting and this is represented by the variation of free energy  $-\Delta G_v$ . These two velocity are expressed by the product of distance of diffusing species  $d_\lambda$ , vibration frequency of atoms  $\nu$ , and probability of diffusion driven by the thermic activation:

$$v_{lc} = d_\lambda \nu \exp\left(-\frac{\Delta G_D}{k_B T}\right) \text{ and } v_{cl} = d_\lambda \nu \exp\left(-\frac{\Delta G_D - \Delta G_v}{k_B T}\right) \quad (2.2.9)$$

Therefore, the crystal growth rate can be expressed in terms of the  $d_\lambda$  with introducing the fraction  $f^*$  of available places for growth:

$$C(T) = f^* d_\lambda \nu \exp\left(-\frac{\Delta G_D}{k_B T}\right) \left(1 - \exp\left(\frac{\Delta G_v}{k_B T}\right)\right) \quad (2.2.10)$$

And the evaluation of nucleation rate  $N(T)$  and crystal growth rate  $C(T)$  is represented in figure 2.5.

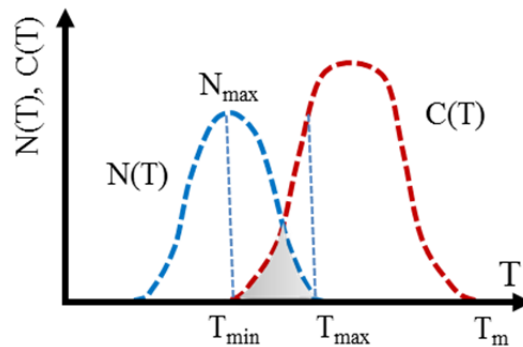


Figure 2.5 the evaluation of nucleation rate  $N(T)$  and crystal growth rate  $C(T)$

It shows that when  $T = T_m$ , the growth rate is definitely zero. In this case, degree of supercooling  $\Delta T$  is infinitesimal. After then the  $C(T)$  goes up almost linearly and arrives at  $C_{max}$  with a lower temperature. If temperature continuously decreases, the diffusion becomes particularly difficult and the  $C(T)$  drops and is closed to zero. At this moment, the crystal growth rate  $C(T)$  is less than nucleation rate  $N(T)$ . Similarly, the nucleation rate rises up at first when temperature goes down. And after it passes the maximum value, it falls down to zero when temperature is around transition temperature  $T_g$ . The crystalline nucleus can be formed and crystal growth happens between  $T_{min}$  and  $T_{max}$ . It should note that  $\Delta G_D$  of these two processes is not necessary identical.

So far, two crystal growth mechanisms have been generally discussed: the continuous growth or structural units adhere anywhere on the crystal, resulting in uniform crystallization front, or lateral growth occurs on preferential sites by a surface nucleation process or by a screw dislocation<sup>[53]</sup>. One of the limit parameters concerning to the crystal growth is latent heat of crystallization. The facility that makes the system to evacuate the heat has consequences on crystal growth: if the heating is faster than it evacuation, the temperature will rise up to form supercooled crystal-liquid interface which limits the growth rate. Another parameter is diffusion at short or long atomic distance in liquid towards the interface.

### 2.2.1.4 Phase separation

In glass, the variation of free enthalpy (energy) associated to the phase separation process is in function of temperature,  $\Delta G(T)$ . As we discussed above, the minimization of free energy of system is introduced by thermal or chemical changes [49] and it is regarded as the original of nucleation of phases in supercooled liquid. In order to interpret clearly the crystal growth and its morphology during phase separation process, we take into account a liquid-liquid phase diagram of a binary system A-B (figure 2.6). At high temperature, this system is kind of homogeneous liquid. When temperature decreases, the components A and B are immiscible and result in two distinct phases in system.

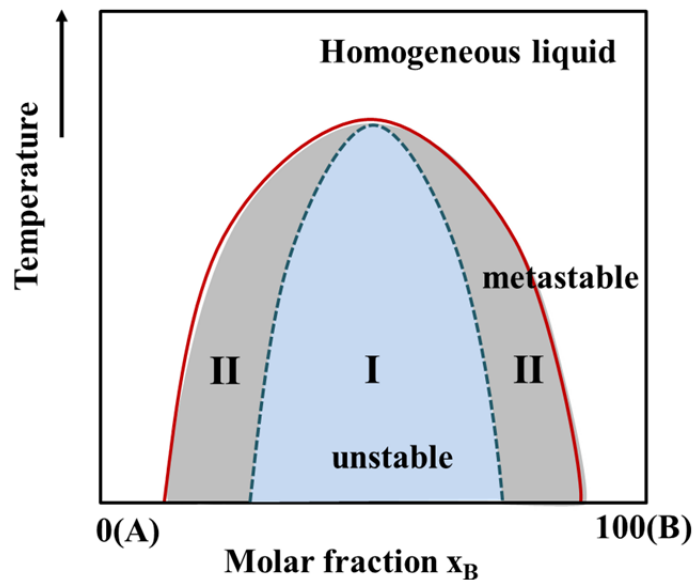


Figure 2.6 Binary diagram of system A-B

If the system is in metastable zone II which is between the coexistence curve (red curve) and spinodal curve (blue curve in dash), phase separation occurs by nucleation/growth mechanism that it needs to overcome the energy barrier to form stable nucleus and the extension of new phase. Correspondingly, if the system is in unstable zone I who is determined by spinodal curve, two separated phases definitely appear because of spinodal decomposition without the limit of energy barrier<sup>[54]</sup>.

Typical concentration profiles of these two mechanisms are shown in figure 2.7.

Figure 2.7 (a) represents the schematic concentration profile and diffusion process of phase separation in unstable zone I which is determined by spinodal decomposition mechanism. It is observed that concentration fluctuation is small but large effected space range at the beginning of phase separation process. With the process of phase separation, the fluctuation of concentration become larger and then phase separation completes in the end. Indeed, in order to minimizing system energy, the companied spontaneous crystallization occurs in one of two phases frequently. Generally, the crystallized part owns a dendritic form and crystalline are interconnected<sup>[55]</sup>. Figure 2.7(b) is related to the fluctuation of concentration during nucleation-growth process. Comparing to the (a), larger fluctuation but smaller spatial range has been observed. The concentration of the second phase is independent on the time and here is always an obvious interface between these two phases. In this case, the crystallized particles which tend to be spherical are more or less randomly distributed, while non-spherical phases generated in spinodal decomposition process are strong connected. Haller has demonstrated that assembly structure can be obtained by nucleation mechanism<sup>[56]</sup>.

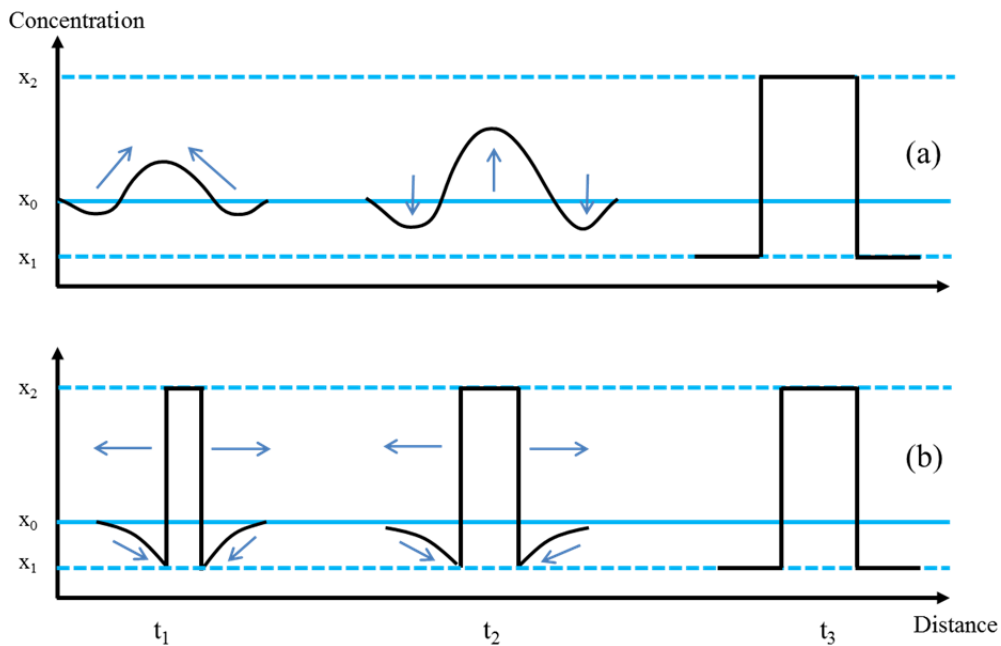


Figure 2.7 The schematic profiles of concentration and diffusion processes of two different mechanisms of phase separation: (a) spinodal decomposition and (b) nucleation-growth in function of time with  $t_1 < t_2 < t_3$ .

### 2.3.1.5 TTT diagram

TTT diagram (Time-temperature-transformation) has been widely used in order to describe phase transformation in nucleation and crystal growth process. It normally gives information in terms of required time to achieve one transformation ratio (here, it is the crystallization ratio) at a given temperature. By determining the nucleation and growth velocity calculated from Eqs. (2.2.7), (2.2.8) and (2.2.11), we can get TTT curves for volume fraction of  $y=1 \times 10^{-6}$  which corresponds to the first instant of crystallization. Moreover, if we draw TTT curves at volume fraction of 99%, a TTT curve can be obtained for quasi-total crystallization as shown in red curve in figure 2.8. The limit of crystallization front ( $T_n, t_n$ ) is concerned with the first germination in supercooled liquid at  $T_n$  for a period  $\tau$ . This point gives a critical velocity of cooling:

$$R_c = \frac{T_n}{t_n} \quad (2.2.11)$$

Here,  $R_c$  is the critical velocity of cooling process. If the velocity  $dT/dt > R_c$ , the temperature incline is fast enough to avoid crystallization area. Oppositely, if  $dT/dt < R_c$ , the temperature incline is in the crystal formation zone and the system evolves in the crystalline field.

This diagram is often built experimentally as shown in figure 2.9. The velocities are measured at a given temperature involved with the ratio of crystal size and reaction time.

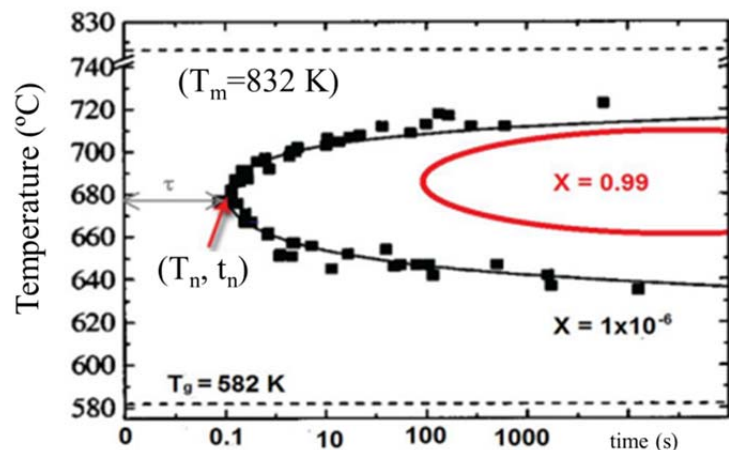


Figure 2.8 A TTT diagram of glass with fraction of crystallized volume at  $10^{-6}$  and 99%

Since TTT diagram can be used to estimate the velocities of nucleation and crystal growth, the number and size of crystals in glass can be theoretical designed and elaborated. For instance, Vigouroux et al.<sup>[57]</sup> has discussed the crystallization process in 35Li<sub>2</sub>O-25Nb<sub>2</sub>O<sub>5</sub>-40SiO<sub>2</sub> glass and reported that the maximum nucleation rate is around  $3 \times 10^{14}$  m<sup>3</sup>/s at 580° with assuming a homogeneous nucleation step in this manner.

### 2.3.2 Methods for oriented crystallization

It has been mentioned above that a traditional method to fabricate glass-ceramic is to control the crystallization process during heat treatment. It is reported that glass-ceramics possessing aligned microstructures with a preferred orientation offer interesting physical anisotropies because a number of their physical properties are dependent on microstructure<sup>[58]</sup>. However, when a glass-ceramic devitrified without any external constraint, the precipitated crystals tend to be randomly oriented. The macroscopic anisotropic properties cannot be achieved<sup>[59-60]</sup>. So, anisotropy is necessary and has been achieved by anisotropic kinetics or/and space direction dependent thermodynamics or by applying external fields like plastic deformation processes (e.g., extrusion), electric, magnetic, concentration, and light energy field, or also by a combination of several of them.

#### Controlled heat treatment

The controlled heat treatment means that the glass is heat-treated in an electric furnace using surface discontinuity or/and a thermal gradient to orient crystallization. As the surface is a source of anisotropy because of its defect concentration, Ding et al.<sup>[61]</sup> have fabricated c-axis oriented crystallized LiNbO<sub>3</sub> on the surface of 35(Li<sub>2</sub>O, K<sub>2</sub>O)-30Nb<sub>2</sub>O<sub>5</sub>-35SiO<sub>2</sub> glass with a thickness of 1.33 μm. Furthermore, various kinds of highly oriented crystals, such as Li<sub>2</sub>Si<sub>2</sub>O<sub>5</sub><sup>[62]</sup>, Ba<sub>2</sub>TiGe<sub>2</sub>O<sub>8</sub> and (Ba<sub>x</sub>Sr<sub>2-x</sub>)TiSi<sub>2</sub>O<sub>8</sub><sup>[63]</sup> and Ba<sub>2</sub>TiSi<sub>2</sub>O<sub>8</sub><sup>[39]</sup> crystals have been fabricated successfully in glasses with optimum temperature gradients. Indeed, the precipitation of crystallites from the precursor glass with a preferred direction of orientation leads to a limited average crystal size of less than 1 μm by this controlled heat treatment. But, the shortage of this process is

time consuming, requires complicated equipment and is unable to locate precipitated regions precisely.

#### **Ultrasonic surface treatment**

It was reported that the enhancement of nucleation and precipitation of desired crystals occurs when glass is subjected to ultrasonic surface treatment in suspensions containing crystalline particles before heat treatment. Via this method, the preparation of  $\text{Li}_2\text{B}_4\text{O}_7$ ,  $\beta\text{-BBO}$ ,  $\text{Ba}_2\text{TiGe}_2\text{O}_8$  and langasite-type crystals such as  $\text{Ba}_3\text{Ga}_2\text{Ge}_4\text{O}_{14}$  and  $\text{BaGa}_4\text{La}_2\text{Ge}_2\text{O}_{14}$  functional thin films on glass surface have been achieved<sup>[64-71]</sup>.

#### **Mechanical hot extrusion method**

The flow behavior of glasses hot-extruded through opposed dies at temperatures near their crystallization temperature has been investigated by Ashbee<sup>[72]</sup> and crystal alignment in  $\text{Li}_2\text{O-SiO}_2$  glass system was achieved during extensional flow and it remained aligned during subsequent drawing down to fibers. However, the apparatus used for the extrusion technique is so much complicated compared to other methods.

#### **Electrochemical synthesis**

Because of the effect of electric and of concentration field, electrochemical synthesis is used to obtain highly oriented fresnoite, lithium niobate, and lithium disilicate glass ceramics after firstly reported by Rüssel's group<sup>[41, 73-75]</sup>. It was found that nearly all of the crystals induced by electrochemical nucleation show dendritic growth in the direction of crystallographic c-axis perpendicular to the electrode surface. The applied conditions, such as electric field strength, time, or apparatus used in nucleation process have been studied to realise high degree of orientation of crystals in glass<sup>[40, 76-78]</sup>.

#### **Magnetic field effect**

This method used for oriented crystallization was firstly reported by Toyohara et al.<sup>[79-80]</sup>. Moreover, they reported that using high magnetic field the c-axis (polarization axis) orientation and second-harmonic intensity of the  $\text{Ba}_2\text{TiGe}_2\text{O}_8$  crystals in  $\text{BaO-TiO}_2\text{-GeO}_2$  glass system have been obtained. It was found that the direction of applied magnetic field affected the crystallization in glass compared to conventional crystallization in zero magnetic fields.

#### **Laser irradiation**

Recently, lasers have been widely applied for the spatial modification, and micro-manufacturing with the increasing development of laser technology. It has been regarded as a powerful tool for spatially selected structural modifications, phase change, crystallization and dissolution in transparent materials. It was reported that the function crystals could be precipitated on the surface of glasses by different kinds of continuous-wave lasers<sup>[81-94]</sup>. Besides, the controlled orientation of Strontium barium niobates like  $\text{Sr}_x\text{Ba}_{1-x}\text{Nb}_2\text{O}_6$  crystals in glass can be achieved by heat-assisted continuous-wave Nd:YAG laser irradiation<sup>[85]</sup>.

However, the continuous-wave laser induced crystallization technique was impossible to fabricate the crystal in a glass bulk in spite that it can be applied successfully for precipitating of nonlinear optical crystals in the vicinity of glass surface. Thus, ultrashort laser attracts many attentions of researchers at this point of view.

So far,  $\text{Ba}_2\text{TiSi}_2\text{O}_8$ ,  $\text{Sr}_2\text{TiSi}_2\text{O}_8$  and  $\text{Ba}_2\text{TiGe}_2\text{O}_8$  nonlinear crystals have been selectively precipitated by femtosecond laser which grow from the surface of glass to the interior along the laser movement direction when the laser focus was continuously moved perpendicular to the surface<sup>[95-97]</sup>. In addition, Stone et al.<sup>[98]</sup> reported on the direct control of three dimensional ferroelectric single crystal growth of  $\text{LaBGeO}_5$  from  $25\text{La}_2\text{O}_5$ - $25\text{B}_2\text{O}_3$ - $50\text{GeO}_2$  (mol%) glass by femtosecond laser irradiation. After then, Fan et al. has discussed the oriented crystallization induced directly by femtosecond laser irradiation<sup>[99]</sup>. It is certain that the most efficient method to realize oriented crystallization in space-selectively should be ultrashort laser irradiation. Indeed, ongoing researches are now focused on different glass systems for generalization and on the determination of laser parameters and glass composition windows for an efficient control of the shape, size and orientation growth of the crystals inside glass matrices. But, we should know laser-induced modifications in transparent glass at first and this will be discussed in next section.

## 2.3 Laser-induced modifications in transparent glass

### 2.3.1 Fs laser-induced modifications

The high intensity achieved with a fs-laser pulse is the key to precise material modification in the bulk of transparent media. The high intensity of the tightly focused fs-laser pulse can be absorbed by the material, promoting electrons from the valence band to the conduction band<sup>[100]</sup>. It is known that fs laser focused in a transparent material requires highly nonlinear light-matter interaction since a single photon energy of visible light does not exceed the bandgap energy of such materials<sup>[101]</sup>. This permits nonlinear absorption via multiphoton processes during fs laser illumination. For instance, several mechanisms of nonlinear excitation process have been discussed as a role in absorption, photoionization and avalanche ionization<sup>[102]</sup>. In addition, the nonlinear nature of the fs-laser absorption provides material modification in highly localized (micrometer sized) regions, with little collateral damage, in specified points throughout the bulk of a transparent medium<sup>[102-103]</sup>. Structural studies of the resulting modification, after fs-laser absorption, have shown damage, i.e. voids or cracks, a modification to the refractive index or induced crystallization depending on the fs-laser modification parameters<sup>[104-105]</sup>. For instance, laser-induced modification has been studied systematically and four regimes with three thresholds have been well defined depending on the laser intensity and numerical aperture (NA) of microscope objective<sup>[106-107]</sup>.

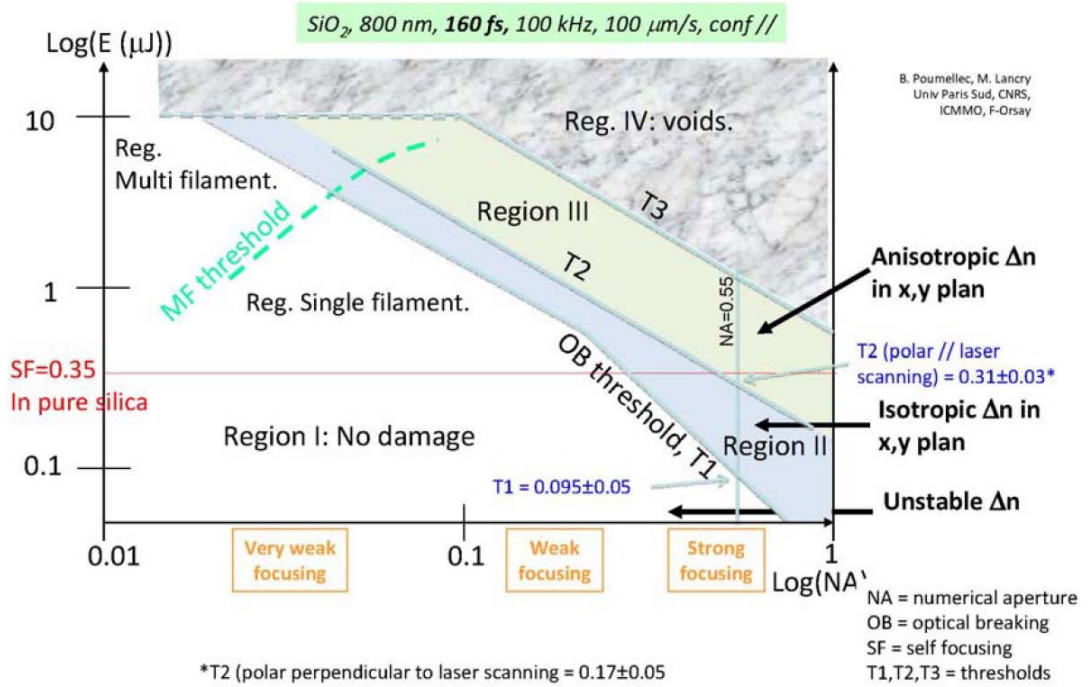


Figure 2.9 Pulse energy versus numerical aperture diagram in log-log scale defining regions with different kinds of laser interaction with pure silica. N.B.: the blue discontinuous line marks the position where we have precisely positioned the thresholds by means of different types of observations<sup>[106-107]</sup>.

T1, the first threshold damage as shown in figure 2.9, stands for the optical breaking threshold and predicts the appearance of isotropic index change in the plan perpendicular to the direction of light propagation. When a microscope objective with NA was utilized during irradiation in pure silica, the typical value of T1 was about  $0.095 \pm 0.05 \mu\text{J/pulse}$  with other parameters as 800 nm, 160 fs, and 100 kHz. The second threshold damage T2 means the appearance of anisotropic index change in the plan perpendicular to the light propagation direction, which is around  $0.31 \pm 0.03 \mu\text{J/pulse}$  in pure silica when the writing laser polarization is parallel to the laser scanning direction<sup>[106]</sup>. Above T2, the index change is highly anisotropic and a strong linear birefringence is observed. The main reason is regarded as the appearance of nanogratings<sup>[108-109]</sup>, nanoplanes<sup>[110]</sup> or residual stress accompanied with laser irradiation<sup>[111-112]</sup>. The third damage threshold T3 represents the appearance of voids

or cracks in interaction volume. We know that under a narrow set of conditions the fs-laser modification results in highly localized changes in refractive index in transparent material.

The mechanisms of fs-laser induced modification are not completely understood. While the multiphoton absorption of laser energy is fairly well understood, the models of energy dissipation are not. Dissipation models of micro-explosions and fast heating and cooling have evolved to explain different types of modification but further observations of the modification process, laser-induced crystallization, need to be made to understand how exactly the fs-laser energy leads to crystallize in glass and how to control the shape, size and orientation of crystals as permanent modifications in glass<sup>[104-105, 113]</sup> ..

### **2.3.1 Fs laser-induced crystallization**

In addition to the use of photo-induced refractive index changes for writing process, fs laser induced processes have been used to generate selective precipitation and phase change. Laser-induced crystallization of glass opens a new field with the possibility to elaborate 3D complex microstructures in volume. For understanding the effect, we have to consider that the main effect is the light energy deposition that leads to material heating. Because of the precise character and 3D crystallization of fs laser micromachining, we will discuss the process of fs laser induced crystallization in glass volume.

When such a laser is focused into a small area in a transparent material, the high light intensity enables multiphoton electron excitation (ionization i.e. interband transitions). Then, electron relaxes partially forming self-trapped exciton (STE) by coupling with a positively charged local deformation (until a fraction of ns). Then, STE's annihilate by coupling with the lattice over ns,  $\mu$ s or ms scale of time. Relaxation of electron and STE annihilation contribute to the lattice heating. The temperature at the focus center increases dramatically as a result of this nonlinear absorption and non-radiative relaxation. At the end, the irradiated matter is thermalized i.e. back to room temperature due to thermal diffusion. The localized heat accumulation happens if the repetition rate is high enough. The average temperature

is mainly determined by the pulse energy, the thermal diffusion property and the heat capacity of the material. Indeed, as we discussed in the last section, the crystallization happens only in a range of temperature, which is between the nucleation and growth rate intersection in figure 2.5.

Moreover, the accompanied phenomenon, such as self-focusing and spherical aberration, elemental migration and oriented crystallization has been discussed by many researchers<sup>[114-116]</sup> Zhong et al.<sup>[115]</sup> showed that an asymmetric distribution along the light propagation direction of multiple crystalline phases was originated from an inhomogeneous intensity distribution of applied laser which was probably due to both of self-focusing effect and spherical aberration effect. The ring-shaped crystalline phases of LiNbO<sub>3</sub> in Li<sub>2</sub>O-Nb<sub>2</sub>O<sub>5</sub>-SiO<sub>2</sub> glass system combining elemental redistribution has been obtained and exhibited<sup>[116]</sup>. The other functional crystalline phases in ring-shape with elemental migration, such as Ba<sub>2</sub>TiSi<sub>2</sub>O<sub>8</sub> and β-BaB<sub>2</sub>O<sub>4</sub>, have been discovered as well by fs laser irradiation in BaO-TiO<sub>2</sub>-SiO<sub>2</sub> and BaO-Al<sub>2</sub>O<sub>3</sub>-B<sub>2</sub>O<sub>3</sub> glass system, respectively. Nevertheless, Fan et al.<sup>[99]</sup> have exhibited another possibility that nonlinear crystal LiNbO<sub>3</sub> filling-in of the interaction volume can be obtained directly by fs laser writing and the preferential orientation of precipitated crystals is along the laser moving direction in case of polarization parallel to the moving direction. Indeed, the temperature gradient was stated as the origin of element migration, which depended on the strength of the bond between cations and oxygen ions and this phenomenon was interpreted as thermomigration i.e. Soret Effect<sup>[117]</sup>. The researchers experimentally found that the glass network formers, strongly bonded with oxygen, have tendency to concentrate in the hot region or so-called focus center while network modifiers prefers to diffuse from the center of an irradiated spot to the glass matrix<sup>[118]</sup>. In addition, regarding to the oriented crystallization, respective mechanisms have been posed according to the irradiation process. In static mode or quasi-static mode, as heating diffusing radially, the T gradient is thus oriented towards the focus center. Without other forces, the orientation of crystallization is thus towards the center<sup>[116]</sup>. However, the beam scanning modifies this radial geometry and the orientation of crystallization is probably defined by the laser writing direction, but both effects of distribution

chemical potential gradient and temperature gradient should be considered as well<sup>[99]</sup>. Because of complicated shear alignment, crystal-crystal interaction, heat accumulation and thermal diffusion effects working together during laser irradiation as interpreted above, more evidences to better understand what happens during the fs laser-induced crystallization and how to control this process become an issues of crucial importance to control the optical properties of irradiated materials further.

## Reference

- [1]. Rajeev, P. P., Gertsvolf, M., Bhardwaj, V. R., *et al.*, Memory and nanostructure formation in the intense field ionization of fused silica. *Springer Series Chem* **2007**, *88*, 680-682.
- [2]. Franken, P. A., Hill, A. E., Peters, C. W., *et al.*, Generation of Optical Harmonics. *Phys Rev Lett* **1961**, *7* (4), 118-119.
- [3]. Bloembergen, N., Surface nonlinear optics: a historical overview. *Appl Phys B-Lasers O* **1999**, *68* (3), 289-293.
- [4]. Bloembergen, N., Pershan, P. S., Light Waves at the Boundary of Nonlinear Media. *Physical Review* **1962**, *128* (2), 606-622.
- [5]. Butcher P.N., C. D., *The elements of nonlinear optics*. Cambridge University Press: Cambridge, 1990.
- [6]. Kleinman, D. A., Nonlinear Dielectric Polarization in Optical Media. *Physical Review* **1962**, *126* (6), 1977-1979.
- [7]. Guenther R., *Modern Optics*. John Wiley and Sons: New York, 1990.
- [8]. Jerphagnon J., K. K. S., Maker Fringes: A Detailed Comparison of Theory and Experiment for Isotropic and Uniaxial Crystals. *J Appl Phys* **1970**, *41* (4), 1667-1681.
- [9]. Maker, P. D., Terhune, R. W., Nisenoff, M., *et al.*, Effects of Dispersion and Focusing on the Production of Optical Harmonics. *Phys Rev Lett* **1962**, *8* (1), 21-22.
- [10]. Giordmaine, J. A., Mixing of Light Beams in Crystals. *Phys Rev Lett* **1962**, *8* (1), 19-20.
- [11]. Armstrong, J. A., Bloembergen, N., Ducuing, J., *et al.*, Interactions between Light Waves in a Nonlinear Dielectric. *Physical Review* **1962**, *127* (6), 1918-1939.
- [12]. Myers R. A., M. N., Brueck S. R. J., Large second-order nonlinearity in poled fused silica. *Optics Letters* **1991**, *16* (22), 1732-1734.
- [13]. Kazansky, P. G., Russel, P. S., Thermally Poled Glass - Frozen-in Electric-Field or Oriented Dipoles. *Opt Commun* **1994**, *110* (5-6), 611-614.
- [14]. Mukherjee, N., Myers, R. A., Brueck, S. R. J., Dynamics of 2nd-Harmonic Generation in Fused-Silica. *J Opt Soc Am B* **1994**, *11* (4), 665-669.
- [15]. Le Calvez, A., Freysz, E., Ducasse, A., Experimental study of the origin of the second-order nonlinearities induced in thermally poled fused silica. *Optics Letter* **1997**, *22* (20), 1547-1549.
- [16]. Margulis, W., Laurell, F., Lesche, B., Imaging the Nonlinear Grating in Frequency-Doubling Fibers. *Nature* **1995**, *378* (6558), 699-701.
- [17]. Quiquempois, Y., Kudlinski, A., Martinelli, G., Zero-potential condition in thermally poled silica samples: evidence of a negative electric field outside the depletion layer. *J Opt Soc Am B* **2005**, *22* (3), 598-604.

- [18]. Qiu, M., Egawa, S., Horimoto, T., *et al.*, The thickness evolution of the second-order nonlinear layer in thermally poled fused silica. *Opt Commun* **2001**, *189* (1-3), 161-166.
- [19]. Kazansky, P. G., Dong, L., Russell, P. S. J., High second-order nonlinearities in poled silicate fibers. *Optics Letter* **1994**, *19*, 701-703.
- [20]. Takebe, H., Kazansky, P. G., Russell, P. S. J., Morinaga, K., Effect of poling conditions on second-harmonic generation in fused silica. *Optics Letter* **1996**, *21*, 468-470.
- [21]. Nasu, H., Okamoto, H., Kurachi, K., *et al.*, 2nd-Harmonic Generation from Electrically Poled SiO<sub>2</sub> Glasses - Effects of OH Concentration, Defects, and Poling Conditions. *J Opt Soc Am B* **1995**, *12* (4), 644-649.
- [22]. Tanaka, K., Narazaki, A., Hirao, K., Large optical second-order nonlinearity of poled WO<sub>3</sub>-TeO<sub>2</sub> glass. *Optics Letter* **2000**, *25*, 251-253.
- [23]. Dussauze, M., Zheng, X. L., Rodriguez, V., *et al.*, Photosensitivity and second harmonic generation in chalcogenide arsenic sulfide poled glasses. *Opt Mater Express* **2012**, *2* (1), 45-54.
- [24]. Jing, R., Guang, Y., Huidan, Z., *et al.*, Second-harmonic generation in thermally poled chalcogenide glass. *Opt Lett* **2006**, *31* (23), 3492-3494.
- [25]. Dussauze, M., Malakho, A., Fargin, E., *et al.*, Large second order optical nonlinearity in thermally poled amorphous niobium borophosphate films. *J Appl Phys* **2006**, *100* (1).
- [26]. Dussauze, M., Fargin, E., Lahaye, M., *et al.*, Large second-harmonic generation of thermally poled sodium borophosphate glasses. *Opt Express* **2005**, *13* (11), 4064-4069.
- [27]. Guignard, M., Nazabal, V., Troles, J., *et al.*, Second-harmonic generation of thermally poled chalcogenide glass. *Opt Express* **2005**, *13* (3), 789-795.
- [28]. Narazaki, A., Tanaka, K., Hirao, K., Surface structure and second-order nonlinear optical properties of thermally poled WO<sub>3</sub>-TeO<sub>2</sub> glasses doped with Na<sup>+</sup>. *J Opt Soc Am B* **2002**, *19* (1), 54-62.
- [29]. Liu, Q. M., Zhao, X. J., Tanaka, K., *et al.*, Second-harmonic generation in Ge-As-S glasses by electron beam irradiation and analysis of the poling mechanism. *Opt Commun* **2001**, *198* (1-3), 187-192.
- [30]. Liu, Q. M., Gan, F. X., Zhao, X. J., *et al.*, Second-harmonic generation in Ge<sub>20</sub>As<sub>25</sub>S<sub>55</sub> glass irradiated by an electron beam. *Opt Lett* **2001**, *26* (17), 1347-1349.
- [31]. Quiquempois, Y., Martinelli, G., Duthéage, P., *et al.*, Localisation of the induced second-order non-linearity within Infrasil and Suprasil thermally poled glasses. *Opt Commun* **2000**, *176* (4-6), 479-487.
- [32]. Ye, X. W., Liu, L. Y., Xu, L., *et al.*, Second-order nonlinearities of lead borate glasses poled with different electrodes. *J Non-Cryst Solids* **2008**, *354* (12-13), 1250-1255.
- [33]. Xi, Y. G., Xu, Z. L., Hou, Z. J., *et al.*, Second-order optical nonlinearity in bulk PbO/B<sub>2</sub>O<sub>3</sub> glass. *Opt Commun* **2002**, *210* (3-6), 367-373.
- [34]. Xu, Z. L., Liu, L. Y., Fei, Y., *et al.*, Nonuniform bulk second-order optical nonlinearity in PbO/B<sub>2</sub>O<sub>3</sub> glass. *Appl Phys Lett* **2000**, *77* (1), 70-72.
- [35]. Bernardo, E., Scarinci, G., Hreglich, S., Development and mechanical characterization of Al<sub>2</sub>O<sub>3</sub> platelet-reinforced glass matrix composites obtained from glasses coming from dismantled cathode ray tubes. *J Eur Ceram Soc* **2005**, *25* (9), 1541-1550.
- [36]. Holand, W., Rheinberger, V., Apel, E., *et al.*, Principles and phenomena of bioengineering with glass-ceramics for dental restoration. *J Eur Ceram Soc* **2007**, *27* (2-3), 1521-1526.
- [37]. Komatsu, T., Tawarayama, H., Mohri, H., *et al.*, Properties and crystallization behaviors of TeO<sub>2</sub>-LiNbO<sub>3</sub> glasses. *J Non-Cryst Solids* **1991**, *135* (2-3), 105-113.
- [38]. Takahashi, Y., Saitoh, K., Benino, Y., *et al.*, Formation of Ba<sub>2</sub>TiGe<sub>2</sub>O<sub>8</sub> phase in

- BaO-TiO<sub>2</sub>-GeO<sub>2</sub> glasses and their optical non-linearities. *J Non-Cryst Solids* **2004**, *345*, 412-416.
- [39]. Maruyama, N., Honma, T., Komatsu, T., Morphology design of highly oriented nonlinear optical Ba<sub>2</sub>TiSi<sub>2</sub>O<sub>8</sub> crystals at the glass surface by crystallization in reduced atmosphere. *Opt Mater* **2009**, *32* (1), 35-41.
- [40]. Wang, H. C., Liu, Q. M., Cheng, J. S., Field-assisted Isothermal Oriented Crystallization of SrO-TiO<sub>2</sub>-SiO<sub>2</sub> Polar Glass-Ceramics. *Advanced Synthesis and Processing Technology for Materials* **2009**, *66*, 49-52.
- [41]. Anspach, O., Keding, R., Russel, C., Oriented lithium disilicate glass-ceramics prepared by electrochemically induced nucleation. *J Non-Cryst Solids* **2005**, *351* (8-9), 656-662.
- [42]. Mortier, M., Monteville, A., Patriarche, G., Devitrification of fluorozirconate glasses: from nucleation to spinodal decomposition. *J Non-Cryst Solids* **2001**, *284* (1-3), 85-90.
- [43]. Beall, G. H., Duke, D. A., Transparent glass-ceramics. *J Mater Sci* **1969**, *4*, 340-352.
- [44]. Jain, H., Transparent ferroelectric glass-ceramics. *Ferroelectrics* **2004**, *306*, 111-127.
- [45]. Rudnick, J., Stern, E. A., Second-Harmonic Radiation from Metal Surfaces. *Phys Rev B* **1971**, *4* (12), 4274-4290.
- [46]. Bachelier, G., Russier-Antoine, I., Benichou, E., *et al.*, Multipolar second-harmonic generation in noble metal nanoparticles. *J Opt Soc Am B* **2008**, *25* (6), 955-960.
- [47]. Nappa, J., Revillod, G., Russier-Antoine, I., *et al.*, Electric dipole origin of the second harmonic generation of small metallic particles. *Phys Rev B* **2005**, *71* (16).
- [48]. Canfield, B. K., Kujala, S., Kauranen, M., *et al.*, Remarkable polarization sensitivity of gold nanoparticle arrays. *Appl Phys Lett* **2005**, *86* (18).
- [49]. Zarzycki J., *Glass and the vitreous state*. Cambridge University Press: Cambridge, 1991.
- [50]. Fokin, V. M., Zanotto, E. D., Yuritsyn, N. S., *et al.*, Homogeneous crystal nucleation in silicate glasses: A 40 years perspective. *J Non-Cryst Solids* **2006**, *352* (26-27), 2681-2714.
- [51]. Gibbs J.W., Vol. I, Thermodynamics. In *Collected works*, Yale University Press: New Haven, 1948.
- [52]. Berthoud A., Theorie de la formation des faces d'un crystal. *Journal de Chimie Physique* **1912**, *10*, 624-635.
- [53]. Kirkpatrick R.J., crystal growth from the melt: a review. *Am. Mineral.*, **1975**, *60*, 798-814.
- [54]. Cahn, J., Charle, R., The initial stages of phase separation in glasses. *Physical Chemistry of Glasses* **1965**, *6*, 181-191.
- [55]. Uhlmann, D., Kolbeck, A., Phase separation and the revolution in concepts of glass structure. *Physical Chemistry of Glasses* **1976**, *17*, 176-158.
- [56]. Haller, W., Rearrangement kinetics of the liquid—liquid immiscible microphases in alkali borosilicate melts. *J Chem Phys* **1965**, *42*, 686-693.
- [57]. Vigouroux, H., Fargin, E., Fargues, A., *et al.*, Crystallization and Second Harmonic Generation of Lithium Niobium Silicate Glass Ceramics. *J Am Ceram Soc* **2011**, *94* (7), 2080-2086.
- [58]. Atkinson, D. I. H., McMillan, P. W., Glass-ceramics with random and oriented microstructures. *J Mater Sci* **1976**, *11* (6), 994-1002.
- [59]. Atkinson, D. I. H., McMillan, P. W., Glass-ceramics with random and oriented microstructures. *J Mater Sci* **1977**, *12* (3), 443-450.
- [60]. Russel, C., Oriented crystallization of glass. A review. *J Non-Cryst Solids* **1997**, *219*, 212-218.
- [61]. Ding, Y., Miura, Y., Nakaoka, S., *et al.*, Oriented surface crystallization of lithium niobate on glass and second harmonic generation. *J Non-Cryst Solids* **1999**, *259* (1-3), 132-138.

- [62]. Gardopee, G. J., Newnham, R. E., Bhalla, A. S., Pyroelectric Li<sub>2</sub>Si<sub>2</sub>O<sub>5</sub> glass-ceramics. *Ferroelectrics* **1981**, 33 (1), 155-163.
- [63]. Zhang, J. P., Lee, B. I., Schwartz, R. W., *et al.*, Grain oriented crystallization, piezoelectric, and pyroelectric properties of (Ba<sub>x</sub>Sr<sub>2-x</sub>)TiSi<sub>2</sub>O<sub>8</sub> glass ceramics. *J Appl Phys* **1999**, 85 (12), 8343-8348.
- [64]. Ding, Y., Masuda, N., Miura, Y., *et al.*, Preparation of polar oriented Sr<sub>2</sub>TiSi<sub>2</sub>O<sub>8</sub> films by surface crystallization of glass and second harmonic generation. *J Non-Cryst Solids* **1996**, 203, 88-95.
- [65]. Ding, Y., Miura, Y., Osaka, A., Stimulated surface crystallization of beta-barium borate on glass due to ultrasonic treatment and second harmonic generation. *J Mater Res* **1996**, 11 (2), 495-502.
- [66]. Ding, Y., Osaka, A., Miura, Y., *et al.*, 2nd-Order Optical Nonlinearity of Surface Crystallized Glass with Lithium-Niobate. *J Appl Phys* **1995**, 77 (5), 2208-2210.
- [67]. Ding, Y., Miura, Y., Osaka, A., Polar-Oriented Crystallization of Fresnoite (Ba<sub>2</sub>TiSi<sub>2</sub>O<sub>8</sub>) on Glass-Surface Due to Ultrasonic Treatment with Suspensions. *J Am Ceram Soc* **1994**, 77 (11), 2905-2910.
- [68]. Ding, Y., Osaka, A., Miura, Y., Stimulated Surface Crystallization of Lithium-Niobate on Tellurite Glass Due to Ultrasonic Treatment. *J Non-Cryst Solids* **1994**, 178, 103-108.
- [69]. Ding, Y., Osaka, A., Miura, Y., Surface Crystallization of Lead Titanate from Glass Enhanced by Ultrasonic Treatment with Suspension. *J Non-Cryst Solids* **1994**, 176 (2-3), 200-207.
- [70]. Ding, Y., Osaka, A., Miura, Y., Enhanced Surface Crystallization of Beta-Barium Borate on Glass Due to Ultrasonic Treatment. *J Am Ceram Soc* **1994**, 77 (3), 749-752.
- [71]. Kosaka, S., Takahashi, Y., Benino, Y., *et al.*, Crystallization of langasite-type phases in gallium germanate glasses and optical properties of crystallized glasses. *Opt Mater* **2006**, 28 (10), 1129-1135.
- [72]. Ashbee, K. H. G., Anisotropic glass-ceramics produced by extrusion through opposed dies. *J Mater Sci* **1975**, 10 (6), 911-917.
- [73]. Keding, R., Russel, C., Oriented glass-ceramics containing fresnoite prepared by electrochemical nucleation of a BaO-TiO<sub>2</sub>-SiO<sub>2</sub>-B<sub>2</sub>O<sub>3</sub> melt. *J Non-Cryst Solids* **2000**, 278 (1-3), 7-12.
- [74]. Keding, R., Russel, C., The mechanism of electrochemically induced nucleation in glass melts with the composition 2BaO center dot TiO<sub>2</sub> center dot 2.75SiO<sub>2</sub>. *J Non-Cryst Solids* **2005**, 351 (16-17), 1441-1446.
- [75]. Keding, R., Russel, C., Electrochemical nucleation for the preparation of oriented glass ceramics. *J Non-Cryst Solids* **1997**, 219, 136-141.
- [76]. Shyu, J. J., Chen, Y. H., Effect of electric field on the crystallization of lead titanate in a glass. *J Mater Sci* **2004**, 39 (1), 159-163.
- [77]. Pernice, P., Aronne, A., Sigaev, V. N., *et al.*, Crystallization behavior of potassium niobium silicate glasses. *J Am Ceram Soc* **1999**, 82 (12), 3447-3452.
- [78]. Pernice, P., Esposito, S., Aronne, A., *et al.*, Structure and crystallization behavior of glasses in the BaO-B<sub>2</sub>O<sub>3</sub>-Al<sub>2</sub>O<sub>3</sub> system. *J Non-Cryst Solids* **1999**, 258 (1-3), 1-10.
- [79]. Toyohara, N., Benino, Y., Fujiwara, T., *et al.*, Enhancement and depression in second-order optical nonlinearity of Ba<sub>2</sub>TiGe<sub>2</sub>O<sub>8</sub> in crystallized glass prepared in a high magnetic field. *J Appl Phys* **2006**, 99 (4).
- [80]. Toyohara, N., Benino, Y., Fujiwara, T., *et al.*, Improvement of second-order optical nonlinearity in transparent Ba<sub>2</sub>TiGe<sub>2</sub>O<sub>8</sub> crystallized glasses prepared in high magnetic field. *Aicam 2005* **2006**, 11-12, 193-196.
- [81]. Fujiwara, T., Takahashi, M., Ikushima, A.J. , Second-harmonic generation in germanosilicate

- glass poled with ArF laser irradiation. *Appl Phys Lett* **1997**, *71*, 1032-1034.
- [82]. Matsumoto, S., Fujiwara, T., Ohama, M., *et al.*, Crystallization of GeO<sub>2</sub>-SiO<sub>2</sub> glass by poling with ArF-laser excitation. *Opt Lett* **1999**, *24* (20), 1404-1406.
- [83]. Tanaka, H., Honma, T., Benino, Y., *et al.*, YAG laser-induced beta-BaB<sub>2</sub>O<sub>4</sub> crystalline dot formation in Sm<sub>2</sub>O<sub>3</sub>-BaO-B<sub>2</sub>O<sub>3</sub> glasses. *J Phys Chem Solids* **2003**, *64* (7), 1179-1184.
- [84]. Sugita, H., Honma, T., Benino, Y., *et al.*, Formation of LiNbO<sub>3</sub> crystals at the surface of TeO<sub>2</sub>-based glass by YAG laser-induced crystallization. *Solid State Commun* **2007**, *143* (6-7), 280-284.
- [85]. Sato, M., Honma, T., Benino, Y., *et al.*, Line patterning of (Sr,Ba)Nb<sub>2</sub>O<sub>6</sub> crystals in borate glasses by transition metal atom heat processing. *J Solid State Chem* **2007**, *180* (9), 2541-2549.
- [86]. Oikawa, T., Honma, T., Komatsu, T., Laser-induced crystal growth of nonlinear optical Ba<sub>3</sub>Ti<sub>3</sub>O<sub>6</sub>(BO<sub>3</sub>)<sub>2</sub> on glass surface. *Cryst Res Technol* **2008**, *43* (12), 1253-1257.
- [87]. Komatsu, T., Koshiba, K., Honma, T., Preferential growth orientation of laser-patterned LiNbO<sub>3</sub> crystals in lithium niobium silicate glass. *J Solid State Chem* **2011**, *184* (2), 411-418.
- [88]. Kioka, K., Honma, T., Komatsu, T., Fabrication of (K, Na)NbO<sub>3</sub> glass-ceramics and crystal line patterning on glass surface. *Opt Mater* **2011**, *33* (8), 1203-1209.
- [89]. Ihara, R., Honma, T., Benino, Y., *et al.*, Writing of two-dimensional crystal curved lines at the surface of Sm<sub>2</sub>O<sub>3</sub>-Bi<sub>2</sub>O<sub>3</sub>-B<sub>2</sub>O<sub>3</sub> glass by samarium atom heat processing. *Solid State Commun* **2005**, *136* (5), 273-277.
- [90]. Honma, T., Komatsu, T., Patterning of two-dimensional planar lithium niobate architectures on glass surface by laser scanning. *Opt Express* **2010**, *18* (8), 8019-8024.
- [91]. Honma, T., Ihara, R., Benino, Y., *et al.*, Writing of crystal line patterns in glass by laser irradiation. *J Non-Cryst Solids* **2008**, *354* (2-9), 468-471.
- [92]. Honma, T., Benino, Y., Fujiwara, T., *et al.*, Spatially selected crystallization in glass by YAG laser irradiation. *J Non-Cryst Solids* **2004**, *345*, 127-131.
- [93]. Hirose, K., Honma, T., Benino, Y., *et al.*, Glass-ceramics with LiFePO<sub>4</sub> crystals and crystal line patterning in glass by YAG laser irradiation. *Solid State Ionics* **2007**, *178* (11-12), 801-807.
- [94]. Honma, T., Benino, Y., Fujiwara, T., *et al.*, Line patterning with large refractive index changes in the deep inside of glass by nanosecond pulsed YAG laser irradiation. *Solid State Commun* **2005**, *135* (3), 193-196.
- [95]. Dai, Y., Ma, H. L., Lu, B., *et al.*, Femtosecond laser-induced oriented precipitation of Ba<sub>2</sub>TiGe<sub>2</sub>O<sub>8</sub> crystals in glass. *Opt Express* **2008**, *16* (6), 3912-3917.
- [96]. Dai, Y., Zhu, B., Qiu, J. R., *et al.*, Direct writing three-dimensional Ba<sub>2</sub>TiSi<sub>2</sub>O<sub>8</sub> crystalline pattern in glass with ultrashort pulse laser. *Appl Phys Lett* **2007**, *90* (18).
- [97]. Dai, Y., Zhu, B., Qiu, J. R., *et al.*, Space-selective precipitation of functional crystals in glass by using a high repetition rate femtosecond laser. *Chem Phys Lett* **2007**, *443* (4-6), 253-257.
- [98]. Stone, A., Sakakura, M., Shimotsuma, Y., *et al.*, Directionally controlled 3D ferroelectric single crystal growth in LaBGeO<sub>5</sub> glass by femtosecond laser irradiation. *Opt Express* **2009**, *17* (25), 23284-23289.
- [99]. Fan, C. X., Poumellec, B., Lancry, M., *et al.*, Three-dimensional photoprecipitation of oriented LiNbO<sub>3</sub>-like crystals in silica-based glass with femtosecond laser irradiation. *Opt Lett* **2012**, *37* (14), 2955-2957.
- [100]. Ashcroft, N. W., Mermin, N.D., *Solid state physics*. Holt Rinehart and Winstom: New York, 1976.

- [101]. Brabec, T., Krausz, F., Intense few-cycle laser fields: Frontiers of nonlinear optics. *Rev Mod Phys* **2000**, *72* (2), 545-591.
- [102]. Schaffer, C. B., Brodeur, A., Mazur, E., Laser-induced breakdown and damage in bulk transparent materials induced by tightly focused femtosecond laser pulses. *Meas Sci Technol* **2001**, *12* (11), 1784-1794.
- [103]. Glezer, E. N., Mazur, E., Ultrafast-laser driven micro-explosions in transparent materials. *Appl Phys Lett* **1997**, *71* (7), 882-884.
- [104]. Chan, J. W., Huser, T. R., Risbud, S. H., *et al.*, Modification of the fused silica glass network associated with waveguide fabrication using femtosecond laser pulses. *Appl Phys a-Mater* **2003**, *76* (3), 367-372.
- [105]. Chan, J. W., Huser, T., Risbud, S., *et al.*, Structural changes in fused silica after exposure to focused femtosecond laser pulses. *Opt Lett* **2001**, *26* (21), 1726-1728.
- [106]. Poumellec, B., Lancry, M., Chahid-Erraji, A., *et al.*, Modification thresholds in femtosecond laser processing of pure silica: review of dependencies on laser parameters [Invited]. *Opt Mater Express* **2011**, *1* (4), 766-782.
- [107]. Lancry, M., Poumellec, B., Chahid-Erraji, A., *et al.*, Dependence of the femtosecond laser refractive index change thresholds on the chemical composition of doped-silica glasses. *Opt Mater Express* **2011**, *1* (4), 711-723.
- [108]. Bricchi, E., Klappauf, B. G., Kazansky, P. G., Form birefringence and negative index change created by femtosecond direct writing in transparent materials. *Opt Lett* **2004**, *29* (1), 119-121.
- [109]. Shimotsuma, Y., Kazansky, P. G., Qiu, J. R., *et al.*, Self-organized nanogratings in glass irradiated by ultrashort light pulses. *Phys Rev Lett* **2003**, *91* (24).
- [110]. Canning, J., Lancry, M., Cook, K., *et al.*, Anatomy of a femtosecond laser processed silica waveguide [Invited]. *Opt Mater Express* **2011**, *1* (5), 998-1008.
- [111]. Bhardwaj, V. R., Corkum, P. B., Rayner, D. M., *et al.*, Stress in femtosecond-laser-written waveguides in fused silica. *Opt Lett* **2004**, *29* (12), 1312-1314.
- [112]. Poumellec, B., Sudrie, L., Franco, M., *et al.*, Femtosecond laser irradiation stress induced in pure silica. *Opt Express* **2003**, *11* (9), 1070-1079.
- [113]. Glezer, E. N., Milosavljevic, M., Huang, L., *et al.*, Three-dimensional optical storage inside transparent materials. *Opt Lett* **1996**, *21* (24), 2023-2025.
- [114]. Stone, A., Jain, H., Dierolf, V., *et al.*, Multilayer aberration correction for depth-independent three-dimensional crystal growth in glass by femtosecond laser heating. *J Opt Soc Am B* **2013**, *30* (5), 1234-1240.
- [115]. Zhong, M. J., Du, Y. Y., Ma, H. L., *et al.*, Crystalline phase distribution of Dy-2(MoO<sub>4</sub>)<sub>3</sub> in glass induced by 250 kHz femtosecond laser irradiation. *Opt Mater Express* **2012**, *2* (8), 1156-1164.
- [116]. Yonesaki, Y., Miura, K., Araki, R., *et al.*, Space-selective precipitation of non-linear optical crystals inside silicate glasses using near-infrared femtosecond laser. *J Non-Cryst Solids* **2005**, *351* (10-11), 885-892.
- [117]. Shimizu, M., Sakakura, M., Kanehira, S., *et al.*, Formation mechanism of element distribution in glass under femtosecond laser irradiation. *Opt Lett* **2011**, *36* (11), 2161-2163.
- [118]. Miura, K., Shimizu, M., Salakura, M., Kurita, T., Shimotsuma, Y., Hirao, K. In *Formation Mechanism and Applications of Laser Induced Elemental Distribution in Glasses*, PIERS Proceedings, Moscow, Russia, August 19-23; Moscow, Russia, 2012.

## Chapter 3 Experimental section

In this chapter, a short description of glass fabrication method and additional field treatments, such as isothermal heating procedure and illumination by femtosecond laser in virgin glass sample, will be given in 3.1 and 3.2, respectively. To understand well laser-induced modification in the irradiated sample, a series of characterization has been done as illustrated in the following parts. Scanning electron microscope (SEM) is used for observing the morphology of laser tracks cross-section to analysis the internal constraint induced by ultra-short irradiation. X-ray diffraction (XRD), Micro-Raman and electron backscattered diffraction (EBSD) are employed to determine the crystal phase and orientation of crystals. Energy-dispersive X-ray spectroscopy (EDX) has been taken to verify the induced-elemental variation. Moreover, birefringence measurement based on Sénarmont method is to measure the change of the refractive index. And with respect to the nonlinear optical properties, second harmonic (SH) probing such as micro-SHG and SH microscopy measurement are realized on the cross-section and in laser lines, respectively.

### 3.1 Glass fabrication

The  $\text{Li}_2\text{O-Nb}_2\text{O}_5\text{-SiO}_2$  system has been prepared for investigation of photo-induced oriented crystal in nano-size by femtosecond laser. Another glass system,  $\text{SrO-TiO}_2\text{-SiO}_2$ , has been fabricated to understand what happened in the glass when thermal treatment and ultra-fast laser irradiation are used.

#### 3.1.1 Preparation of $\text{Li}_2\text{O-Nb}_2\text{O}_5\text{-SiO}_2$ glass

Basing on the previous work by Fan et al<sup>[1-2]</sup>, the composition of silica-based glass  $33\text{Li}_2\text{O-33Nb}_2\text{O}_5\text{-34SiO}_2$  (mol%) was chosen to be prepared by traditional melt-quenching method. After the reagent grade  $\text{Li}_2\text{CO}_3$ ,  $\text{Nb}_2\text{O}_5$  and  $\text{SiO}_2$  were mixed and melt in Pt crucible at  $1430\text{ }^\circ\text{C}$  for 2 hr, approximately 50 g batches, the obtained melt was poured onto a steel plate heat-treated at  $500\text{ }^\circ\text{C}$ , and transferred to another

electronic furnace pre-set at 540 °C cooling down to room temperature. The transparent glass was annealed to release the stress at the decreasing rate of 20°C/hr for the first 6 hr. The glass transition temperature  $T_g$ , crystallization onset  $T_x$  and crystallization peak temperature  $T_c$  were determined by differential scanning calorimeter (DSC) as 570°C, 648°C and 682°C, respectively<sup>[2]</sup>. The temperature difference of  $T_c-T_g$ , as a measure of thermal stability of glass, is about  $112\pm 4^\circ\text{C}$  to indicate that it takes a shorter time to generate crystals in  $33\text{Li}_2\text{O}-33\text{Nb}_2\text{O}_5-34\text{SiO}_2$  than that in glasses  $32.5\text{Li}_2\text{O}-27.5\text{Nb}_2\text{O}_5-40\text{SiO}_2$  and in  $30\text{Li}_2\text{O}-10\text{Nb}_2\text{O}_5-60\text{SiO}_2$ <sup>[3]</sup>.

### 3.1.2 Preparation of SrO-TiO<sub>2</sub>-SiO<sub>2</sub> glass

Several compositions of SrO-TiO<sub>2</sub>-SiO<sub>2</sub> bulk glasses have been prepared using the conventional melt-quenching method presented in red points in the glass-forming region as shown in the Figure 3-1. The glass compositions were in Table 3.1.

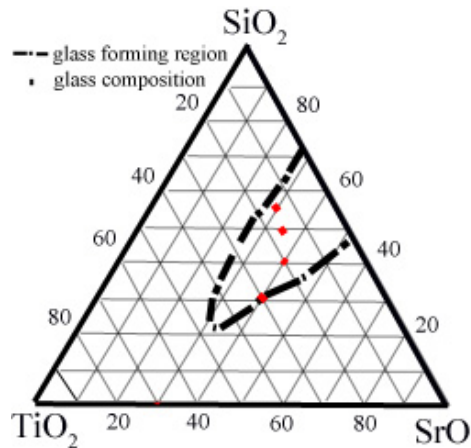


Figure 3.1: glass forming diagram of SrO-TiO<sub>2</sub>-SiO<sub>2</sub> system.

Table 3.1 Glass composition of SrO-TiO<sub>2</sub>-SiO<sub>2</sub> system

	SrO (mol%)	TiO <sub>2</sub> (mol%)	SiO <sub>2</sub> (mol%)	
STS-1	40	20	40	transparent
STS-2	33.3	16.7	50	transparent
STS-3	30	15	55	demi-opaque
STS-4	40	30	30	opaque

The reagent grade SrCO<sub>3</sub> (99.95%), TiO<sub>2</sub> (99.9%), and SiO<sub>2</sub> (99.9%) were

mixed and well mixed in a Pt crucible at 1450°C for 2 hours and then quenched on a steel plate at 200°C. A subsequent annealing was taken at 650 °C for 12 h which is higher than  $T_g$  but lower than their  $T_c$ ). Differential scanning calorimetry (DSC) curve of 33.3SrO-16.7TiO<sub>2</sub>-50SiO<sub>2</sub> has been presented in figure 3.2 that the  $T_g$  is about 483.4 °C while  $T_c$  is 806.4 °C.

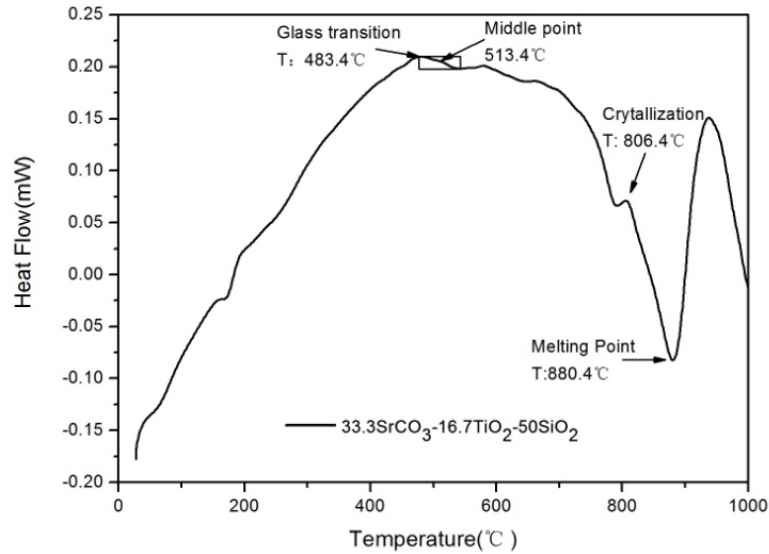


Figure 3.2: DSC curve of 33.3SrO-16.7TiO<sub>2</sub>-50SiO<sub>2</sub> system.

### 3.1.3 Polishing of glass samples

After the glass materials were cut by Labcut 150 with diamond disc cutter into 10 mm×10 mm×1.5 mm, the cut flat samples were mounted in epoxy resin for the polishing. The primary rough polishing was carried out with polishing paper from P240 to P1500 at 200 r/min. Subsequently, to reach optical quality ( $\lambda/10$ ), the polishing of two surfaces of specimen was taken with different grainsized diamond lapping films (15  $\mu\text{m}$ , 6  $\mu\text{m}$ , 3  $\mu\text{m}$ , and 1  $\mu\text{m}$ , UltraPrep Diamond lapping films). The final polishing, used to eliminate all the scratches from the surface, was realized on a soft felt pad wet by a colloidal silica suspension, which contains very thin grain (0.25 $\mu\text{m}$ ). The typical parameters are reported in Table 3.2.

Table 3.2 Typical polishing parameters of glass samples

Treatment	Time	Turning speed (t/min)	Diluents
Mounting in the model of epoxy resin	3hr or even more	-	-
polishing with SiC papers	5 min for each	170	water
polishing with 15 $\mu$ m diamond lapping film	5 min	70	water
polishing with 6 $\mu$ m diamond lapping film	5 min	40	water
polishing with 3 $\mu$ m diamond lapping film	5 min	20	water
polishing with 1 $\mu$ m diamond lapping film	10 min	minimum speed	water
polishing with 0.25 $\mu$ m soft felt pad	20~30 min	70	colloidal silica suspension
HF acid etching	LNS-10%HF, 10 min		water
	STS-2%HF, 30 s		

### 3.2 The treatment by additional fields

In order to get crystallization on the sample surface or in volume, different types of additional field treatments have been chosen, such as heat treatment by electric furnace or irradiation by femtosecond laser.

#### 3.2.1 Thermal treatment

According to the DSC curve of 33.3SrO-16.7TiO<sub>2</sub>-50SiO<sub>2</sub> system presented in figure 3-2, we put samples to be thermal treated in electric furnace during different periods at varied temperatures to get crystallization. The detail were described in the ref<sup>[4]</sup>.

### 3.2.2 Irradiation set-up by femtosecond laser

A high repetition rate femtosecond laser used for direct inscription experiments to get crystallization both in  $\text{Li}_2\text{O-Nb}_2\text{O}_5\text{-SiO}_2$  glass and  $\text{SrO-TiO}_2\text{-SiO}_2$ , is a kind of Yb-doped fiber amplify femtosecond laser system (Satsuma, Amplitude system Ltd.) operating at 1030 nm with pulse duration around 300fs. The repetition rates ranging from several kHz up to 5 MHz was utilized in the experiments. Figure 3.3 is the experimental set-up for direct laser writing in the material and SHG imaging. The energy of laser beam was controlled by assembled half-wave plate and a polarizer in the path way figured out in the red rectangle. Varying linear polarization was performed with the help of the second half-wave plate after the light passing through the shutter. The laser beam was focused at different depth inside glasses below the entry surface with a NA=0.6 microscope objective for 3D stage writing with varied energies from 0.1 up to 2.5  $\mu\text{J}/\text{pulse}$  measured after it as shown in figure 3.4. The laser motion velocity was varied from 5 up to 100 $\mu\text{m}/\text{s}$ . Typically, the deviation of the polarizer orientation respected to the scanning direction is less than 1 degree and “purity” of polarization state is 0.1% in linear state. The precision on the relative change of pulse energy is 0.1% while that on the absolute value of pulse energy is better than 3% with considering the laser energy fluctuations with time per day.

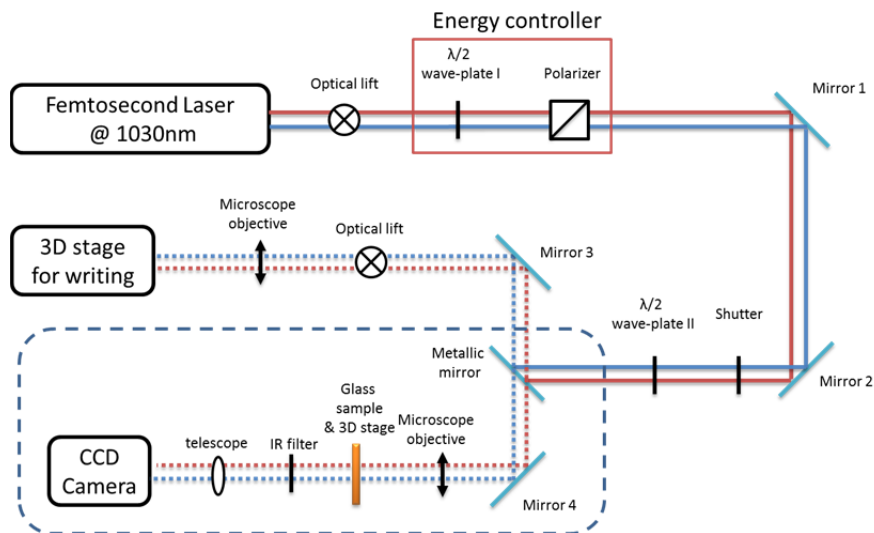


Figure 3.3 Experimental set-up of 3D laser writing inside glass.

The rectangle in dashed-line presents the additional dispositive for SHG measurement.

In addition, the writing configuration was defined concerning the motion directions and laser polarizations. The first capitalized letter denoted the motion along X-axis or in Y-axis. Actually, there were two moving directions along one axis, towards positive direction or negative direction. Therefore, the second lower case letter p and n was used to present the facing these two directions, respectively. The linear polarization direction applied during the inscription procedure was denoted by the third capitalized letter. Hence, Xp-Y indicated for instance that the laser lines were written along x-axis (from the origin of the coordinate axes) facing the positive direction with a perpendicular polarization in y-axis.

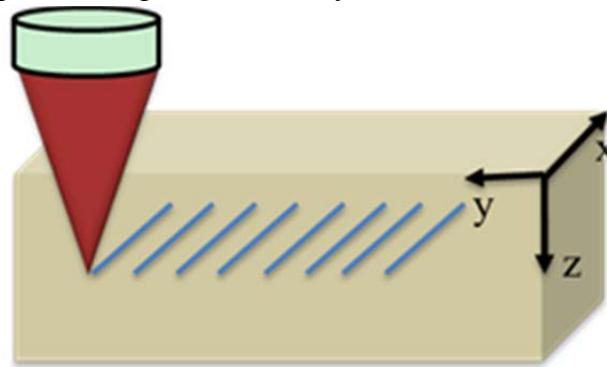


Figure 3.4 Scheme of laser irradiation inside glass. Laser propagates: **z**-axis, writing and polarization direction: **x**-axis or **y**-axis

### 3.3 Characterization of induced structural modification

The common characterization method, including polarized optical microscope, EDX, nuclear microprobe, Micro-Raman, SEM equipped with EBSD and Maker fringes were implemented for understanding the induced structural modification by additional field treatment. Glass samples illuminated by laser should be cleaved along perpendicularly to the written lines, polished to the optical quality and subsequently etched by hydrogen fluoride acid indicated in Table 3-2.

### 3.3.1 Chemical analysis

#### 3.3.1.1 Energy Dispersive X-ray Spectrometry (EDX or EDS)

EDX is a kind of method using the X-ray spectrum emitted by a solid sample bombarded with a focused beam of electrons to obtain a localized chemical analysis. All elements from atomic number 4 (Be) to 92 (U) can be detected in principle, though not all instruments are equipped for “light elements” ( $Z < 10$ ). Qualitative analysis involves the identification of the lines in the spectrum and is fairly straightforward and quantitative analysis entails measuring line intensities for each element in the sample. Typically, the overall analytical accuracy is commonly nearer  $\pm 2\%$ . The nominal spatial resolution is about  $1\sim 2\ \mu\text{m}$  under typical conditions in the case of silicate glass. The non-conducting glass sample must be coated using vacuum-evaporated carbon ( $\sim 20\ \text{\AA}$  thick).

#### 3.3.1.2 WDS

A wavelength-dispersive (WD) spectrometer is used to isolate the X-rays of interest for quantitative analysis because of its superior energy resolution as well as high count rate capability without compromising energy resolution compared to the EDX. Typically, individual WDS spot analyses include information on the ratio of the WDS detector counts of the sample relative to the counts on a standard for each element (k-Ratio), a measure of the minimum detection limits of an element (MDL), the weight % of each element (El-Wt%), the weight % of each element expressed as an oxide (Ox-Wt%) that results after the matrix correction is made and the atomic proportions (At-Prop) based on a fixed oxygen normalization basis. The El-Wt% or Ox-Wt% are typically used as input for a subsequent calculation of the stoichiometry of a material that is most appropriate to the nature of the material. For this point of view, several WDS measurements have been taken with high quality resolution for chemical analysis in illuminated samples containing Li element in this thesis.

### 3.3.1.2 Nuclear microprobe

Indeed, light elements could not be detected using the normal chemical analysis method, such as EDX and WDS. In this case, the nuclear elemental analysis was performed at the nuclear microprobe of the CEA/Saclay to display directly the local stoichiometry of lithium in the LNS glass.

A classic ion beam condition for quantitative analysis of Lithium was applied firstly at 2.6 MeV with beam size  $2 \times 2 \mu\text{m}^2$  and intensity 300 pA. A lower energy at 1.65 MeV was chosen to get cartographies of Si concentration with the same beam size and intensity. The experimental set-up was reported in detail in ref<sup>[5]</sup> as shown in figure 3-5.

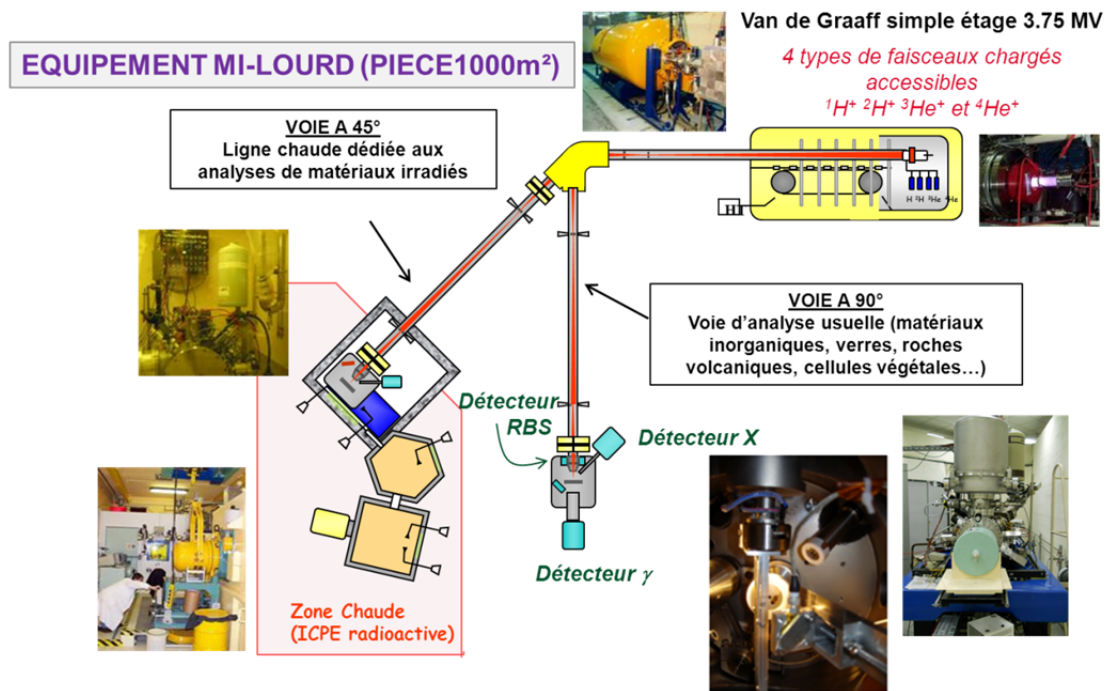


Figure 3.5 Scheme of nuclear microprobe set-up in CEA/Saclay in Orsay.

### 3.3.2 XRD

XRD is a common method used for determining the crystal structure and/or crystals orientation by measuring the angles and intensities of diffracted beams which results from destructive interference of electromagnetic wave (the X-ray) impinging on regular arrays of scatterers (the repeating arrangement of atoms within the crystal

measurements). The following XRD measurements on the thermal treated samples were realized at room temperature using Cu-K $\alpha$  radiation. (D/max-rB; X-ray: Cu-K $\alpha$ ; 40kV $\times$ 50mA; 10 $^\circ$ ·min $^{-1}$ , step by 0.02 $^\circ$ , Santachi Ltd.).

### 3.3.3 Combined Micro-Raman and Micro-SHG mapping

The laser light, in the visible, near infrared or near ultraviolet range, interacts the molecular vibrations, phonons or other excitation in the systems, resulting in different kinds of the scattering, such as inelastic scattering or Raman scattering. As a consequence, the energy of laser photons shifts up or down. Raman spectroscopy is used to, among other things, characterize materials, measure temperature, and find the crystallographic orientation of a sample. It also gives information on the population of a given phonon mode in the ratio between the Stokes (downshifted) intensity and anti-Stokes (upshifted) intensity in solid-state physics. Raman scattering by an anisotropic crystal gives information on the crystal orientation. The polarization of the Raman scattered light with respect to the crystal and the polarization of the laser light can be used to find the orientation of the crystal, if the crystal structure is known. Moreover, as SHG intensity of nonlinear crystal is sensitive to the orientation of polar axis, the micro-SHG can be employed to investigate the micro-structure and orientation of nonlinear crystal in transparent glass.

The modified experimental set-up<sup>[6]</sup> of micro-Raman (HR 800, Horiba/Jobin-Yvon) instrument equipped two laser sources: a picosecond laser at 1064 nm for SHG measurement and a continuous wave (CW) laser at 532 nm for Raman excitation. The combination of micro-Raman scattering spectroscopy and micro-SHG measurement in the reflection mode could be realized by employing the same setup to get a direct link between physical properties and local structure. The 3D mapping involving Raman and SHG signals could be realized by motorizing the sample stage in (X, Y, Z). Typical spectral resolution of Raman spectroscopy is 2.5 cm $^{-1}$  in the backscattering geometry at room temperature. The used microscopy objective is 100 $\times$  (NA=0.5) and laser energy was controlled below the threshold of glass by a filter in order to keep from destroying the sample surface.

The combined micro-Raman and micro-SHG experimental dispositive is shown

in the figure 3.6.

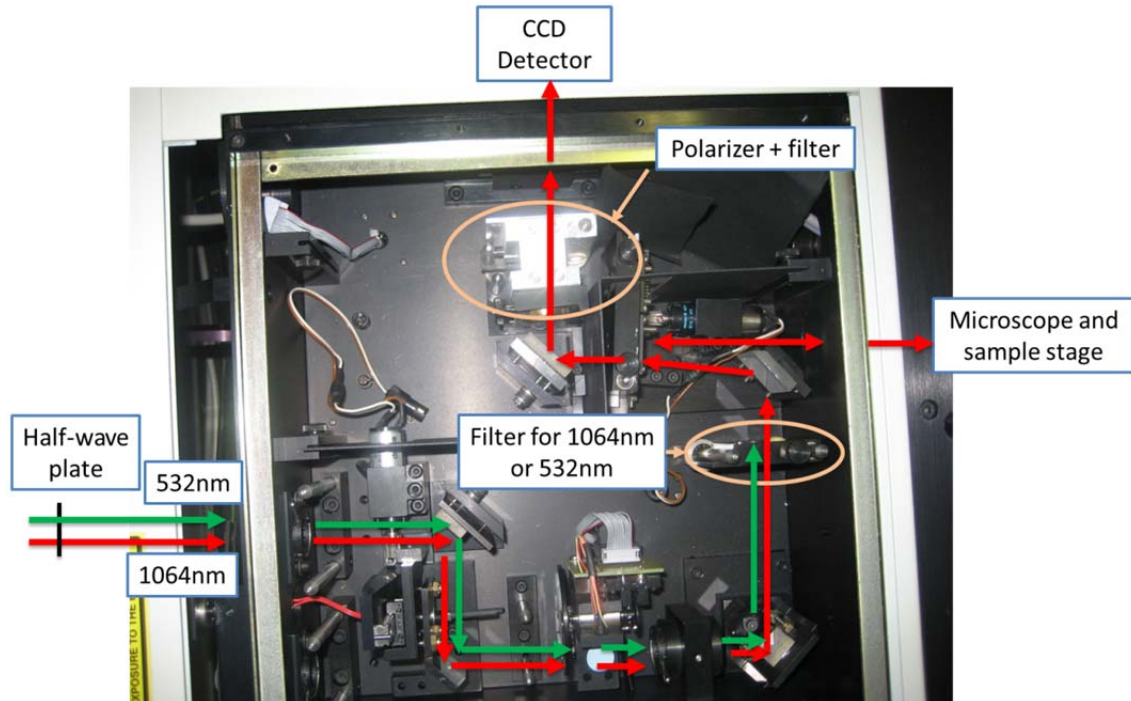


Figure 3.6 The photo of micro-Raman and micro-SHG experimental set-up

### 3.3.4 SEM-EBSD

There are many methods which can be used to measure the local orientation within a microstructure in material. However, among these methods, Electron BackScattered Diffraction (EBSD) equipping with Scanning Electron Microscopy (SEM) became a useful and widespread tool so far. As known as backscatter Kikuchi diffraction (BKD), EBSD is used to examine the crystallographic orientation of many materials, index and identify the seven crystal systems, and as such it is applied to crystal orientation mapping, defect studies, phase identification, grain boundary, etc.

It's important to note that EBSD permits to analyze in a depth below the surface of the sample in the order of a few tens of nanometers. Therefore, this measurement requires a good preparation regarding the characterized surface. Experimentally, a flat /well-polished sample was placed in the SEM chamber at a highly tilted angle ( $\sim 70^\circ$  from horizontal) towards the diffraction camera, to increase the contrast in the resultant electron backscatter diffraction pattern. The phosphor screen was located

within the specimen chamber of the SEM at an angle off approximately  $90^\circ$  to the pole piece and was coupled to a compact lens which focuses the image from the phosphor screen onto the CCD camera. Electrons can backscatter within the material as these backscattering electrons exit the crystal and they may exit at the Bragg condition related to the spacing of the periodic atomic lattice planes of the crystalline structure. Due to the angle of the specimen these diffracted electrons are directed towards and impinged upon the phosphor screen of the diffraction camera causing it to fluoresce, which is then detected by the CCD.

A Field-Emission Gun Scanning Electron Microscope (FEG-SEM ZEISS SUPRA 55 VP) was used for imaging and for analyzing the size and orientations of crystals (EBSD) in the cross section of the laser lines in our work. This equipment allows examining uncoated insulating or dielectric specimens using low accelerating voltage (typ. in the range of 1 kV) and very low current (a few pA). The scanning resolution was about 200nm in our experiments and then all of the EBSD data was analyzed by the OIM<sup>TM</sup> software. The indexed Kikuchi pattern involving the information of crystalline plan in the material is used to determine the symmetries of point group of crystalline phase and crystallographic orientation in dots while EBSD mapping is to analyze the considered crystallographic orientation in volume. Based on EBSD mapping data, the preferential crystallographic orientation of nonlinear crystals in material will analyzed directly with exporting pole figures of polar axis.

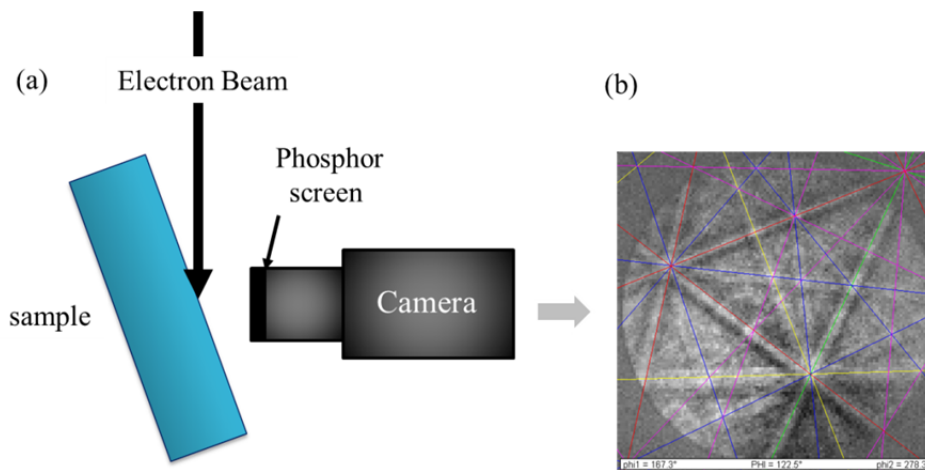


Figure 3.7 the schematic diagram of EBSD implementation (a) and an indexed Kikuchi pattern (b) of SrTiO<sub>3</sub> crystal obtained by SEM-EBSD

### 3.3.5 Refractive index information

The optical microscope is usually used to provide information on absorption color and optical path contrast in a manner similar to bright field illumination. The technique can also distinguish between isotropic and anisotropic substances when using crossed polarization. It leads to the determination of the orientation of neutral optical axis of sample. When inserting a full wavelength plate in the optical path, it is possible to define the slow and fast axis. Then, using a quarter wavelength and the Senarmont method, it is possible to quantify the retardance between the two axes which we talked about.

An Olympus BX-60 optical microscope equipped with a fixed quarter-wave plate ( $\lambda/4$  plate) has been used for that purpose. The method is described in the figure below:

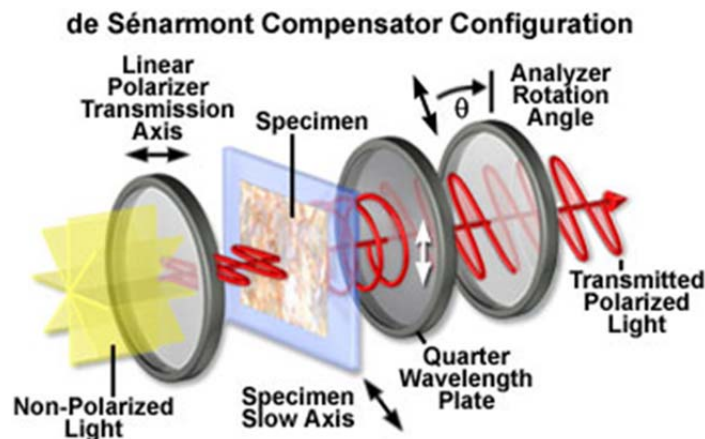


Figure 3.8 schematic drawing of Senarmont compensator configuration

When the specimen is placed diagonally between two crossed polarizers, the linearly polarized light becomes elliptical when passing through the sample with the neutral axis at  $45^\circ$  from the first polarizer. The use of  $\lambda/4$  plate placed with its slow axis vertically, can transform the elliptical light into a linearly polarized waves again. The E vectors of these waves are tilted at some azimuth  $\theta$  depending on the amount of retardation from the specimen. A rotatable analyzer with the accessible precision of 0.1 degree was utilized to measure the azimuth angle and to deduce the amount of retardation from a specimen, which is proportional to birefringence. The relative

retardation (in nanometers) is described by the following equation:

$$R = (\lambda_{mono} \cdot \theta) / 180 \quad (3.1.1)$$

$R$  is retardation of the sample,  $\lambda_{mono}$  is the wavelength of monochromatic light (here is 551.5 nm). Then, the birefringence of the sample can be calculated by:

$$B = R / l \quad (3.1.2)$$

Where  $l$  is the thickness of the object and  $B$  is the birefringence of the sample. Typically, the values  $R$  below 20nm measured by this method have a 10% uncertainty and the ones above 20 nm have a 3 nm uncertainty. Additionally, we assumed that the thickness of the birefringent layer is the whole length of the laser tracks measured on the cross-section, we computed a minimum of birefringence as it is probably not extending on the whole laser tracks.

### 3.3.7 Nonlinear optical properties

The nonlinear optical properties mentioned in this thesis involve particularly second-order nonlinear optical properties of glass. The SHG, also called frequency doubling is a nonlinear optical process, in which photons interacting with a nonlinear material are effectively “combined” to form new photons with twice the energy, and therefore twice the frequency and half the wavelength of the initial photons. Two methods have been employed to investigate the crystals structures (or crystallographic orientation) and SHG in the transparent material. The One is Maker fringe method which is a traditional method used for bulk transparent material. The other one is microscopic SHG measurement especially for irradiated transparent glass by fs laser.

#### 3.3.7.1 Maker fringe method

The Maker fringe method is usually used to characterize the optical properties (linear or nonlinear) of the material, such as the susceptibility  $\chi^{(2)}$ , the refractive index of material at fundamental frequency  $n_{\omega}$  and at double frequency  $n_{2\omega}$ . In comparing the Maker fringes results of a given quartz, the magnitude of absolute value of the tensor  $\chi^{(2)}$  can be obtained. The measurements consist of transmitted SH intensity produced by the nonlinear sample and the rotation angle  $\theta$  of the sample supporter.

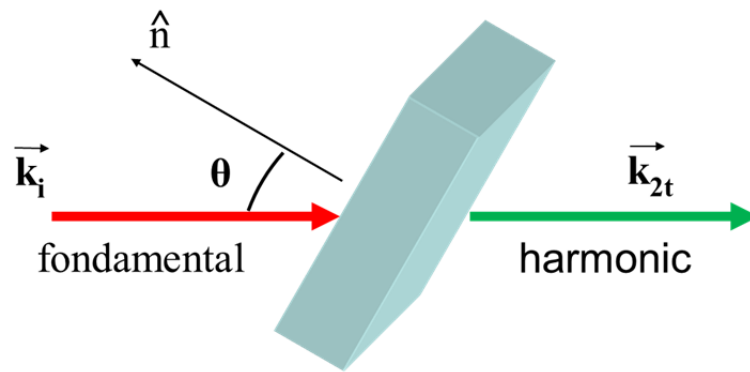


Figure 3.9 The schema of Maker fringes experiments principle in transmission mode.  $k_i$  is the wave vector of incident beam at fundamental wavelength (1064 nm).  $k_{2t}$  is the wave vector of transmitted beam at double frequency (532 nm). The  $\theta$  of the sample supporter is the angle between the  $k_i$  direction and normal direction  $n$  to the sample surface.

The experimental set-up of Maker fringes measurement is described in figure 3.10. It consists of one CW YAG-laser source at 1064 nm with repetition rate 30 Hz. Two dichroic mirrors are used to change the propagation route of laser beam. In order to have large signals, a focusing lens with a 28cm length is used here. The polarizer is set so as to obtain as a horizontal polarization. The focal length of collimating lens is 12.5cm with IR anti-reflect treated. PM involves the Hamamatsu R928 photomultiplier. The response time is about 30 ns, so we can assume that the received intensity is directly proportional to the instantaneous optical power.

During the experiments, it has to keep the beam parallel to the table and the axis of rotation of the support is perpendicular to the table which should be also included in the input face of the sample. Experimentally, there are still some improvements. For example, change another lens with a larger focal length to increase the resolution.

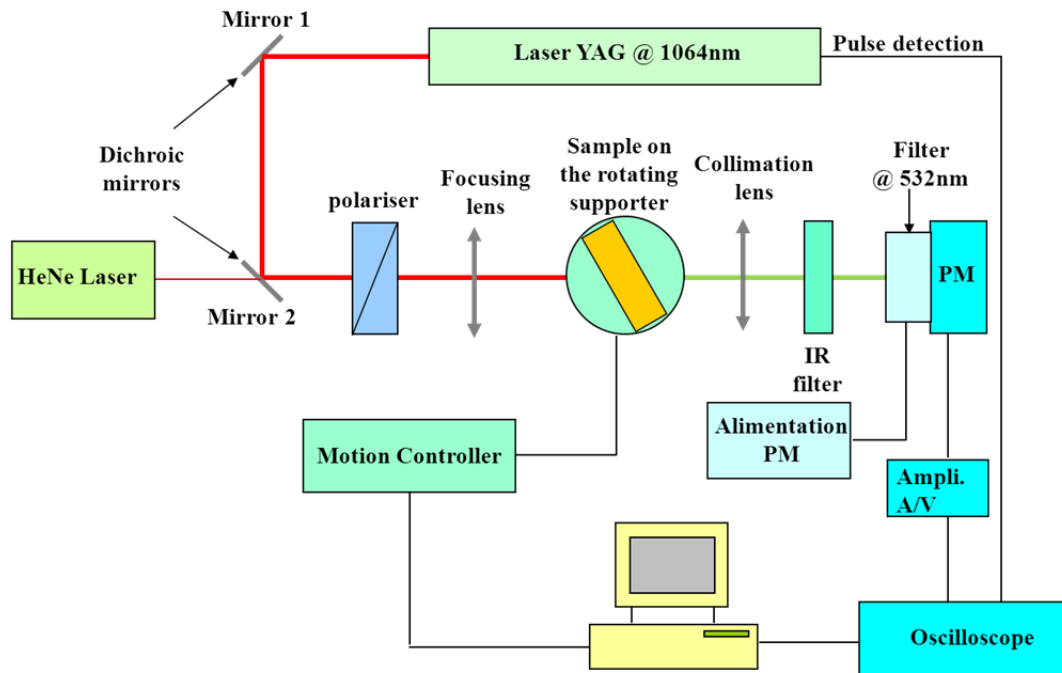


Figure 3.10 The experimental set-up of Maker fringes measurement

### 3.3.7.2 SHG measurement

The microscopic SHG images and SHG probe polarization dependence measurements were realized based on the fs writing set-up as shown in figure 3-3. The rectangle in dashed-line exhibits the experimental dispositive for microscopic SHG images. A PM was used to replace CCD camera in SHG intensity measurement. In this thesis, in order to avoid the laser lines from damage of laser irradiation, the laser parameters were used below threshold of glass modification such as: 1030nm, 300fs, 100 kHz and pulse energy around 0.2  $\mu\text{J}$ . The used objective has been decreased to a smaller NA for a larger imaging. The polarization was also linearly controlled by the front half-wave plate.

## Reference

- [1]. Fan, C. X., Poumellec, B., Lancry, M., et al., Three-dimensional photoprecipitation of oriented LiNbO<sub>3</sub>-like crystals in silica-based glass with femtosecond laser irradiation. *Opt Lett* 2012, 37 (14), 2955-2957.
- [2]. Fan, C. X. Contribution to nano or micro crystallization induction in silica-based glasses by femtosecond laser irradiation. Université de Paris Sud 11 & East China University of Science

- and Technology 2012.
- [3]. Yonesaki, Y., Miura, K., Araki, R., et al., Space-selective precipitation of non-linear optical crystals inside silicate glasses using near-infrared femtosecond laser. *J Non-Cryst Solids* 2005, 351 (10-11), 885-892.
  - [4]. Liu, Q. M., He, X., Sui, X.T., Lu, B.Q., Zhao, X.J., Thermally induced nanocrystallization in SrO-TiO<sub>2</sub>-SiO<sub>2</sub> glasses tracking by the Maker fringe patterns analysis. *J Optoelectron Adv M* 2012, 14, 905-909.
  - [5]. Khodja, H., Berthoumieux, E., Daudin, L., et al., The Pierre Süe Laboratory nuclear microprobe as a multi-disciplinary analysis tool. *Nuclear Instruments and Methods in Physics Research Section B: Beam Interactions with Materials and Atoms* 2001, 181 (1-4), 83-86.
  - [6]. Rodriguez, V., Talaga, D., Adamietz, F., et al., Hyper-Raman macro- and micro-spectroscopy in materials: Towards high quality signals and good spatial resolution. *Chem Phys Lett* 2006, 431 (1-3), 190-194.

## Chapter 4 Thermally induced Nano-crystallization in SrO-TiO<sub>2</sub>-SiO<sub>2</sub> glasses

Since there are few reports to investigate the dynamics of thermal crystallization in Sr<sub>2</sub>TiSi<sub>2</sub>O<sub>8</sub> glasses with Maker Fringe patterns, in this chapter, we synthesized Sr<sub>2</sub>TiSi<sub>2</sub>O<sub>8</sub> glasses with Fresnoite-type crystalline structure by the melt-quenching method, and discussed the influence of thermal conditions on second harmonic(SH) intensity to investigate the dynamics of thermal induced crystallization by the means of Maker fringe patterns.

### 4.1 Experimental details

Fresnoite-type crystallized 2.0SrO-1.0TiO<sub>2</sub>-2.9SiO<sub>2</sub> (mol %) bulk glass was prepared using the conventional melt-quenching method. In a typical experiment, SrCO<sub>3</sub>(99.95%), TiO<sub>2</sub>(99.9%) and SiO<sub>2</sub>(99.9%) were mixed and well melted in a platinum crucible at 1450°C for 2 hours and then quenched on a steel plate at 200°C. The annealing was performed at 650°C for 12h. Glass plates of dimensions of  $\Phi 20 \times 1 \text{ mm}^2$  were cut from bulk glass and mechanically polished to optical quality on both sides. Crystallization was carried out by heating samples with different temperatures ( $T_{\text{HT}}=790^\circ\text{C}$ ,  $810^\circ\text{C}$ ,  $830^\circ\text{C}$ ,  $850^\circ\text{C}$ ,  $870^\circ\text{C}$ ,  $890^\circ\text{C}$ ,  $910^\circ\text{C}$ ) with the heating rate of  $5^\circ\text{C}/\text{min}$  and different period (2h, 3h, 4h and 5h). The optical absorption spectra were recorded with a UV-Vis-near IR Spectrophotometer (Shimadzu UV-1601) in the region of 200-1100 nm with the resolution of 0.5nm. The SH intensities of samples were measured using a pulsed Nd:yttrium-aluminum-garnet (YAG) laser with a pulse width of 10 ns<sup>[1]</sup>. The fundamental wave at 1064 nm was used as the incident light. The output light from the glass plate passed through a filter to split the SH wave at 532 nm from the fundamental wave. The measurements were performed at consecutive angles of incidence from  $-80^\circ$  to  $80^\circ$  with the samples placed on a rotating stage. An  $\alpha$ -quartz (Z-cut, thickness=0.782 mm) was used as reference to adjust the Maker fringe measurements. The crystalline

phase was examined by X-Ray Diffraction (XRD, XRD-Rigaku Ultima III) at room temperature using Cu K $\alpha$  radiation and the thickness of crystallization layer in the surface layer was characterized by Scanning Electron Microscope (SEM, JSM-5610LV).

## 4.2 Experimental results

### Thermally induced nano-crystallization in STS glass

Wang et al<sup>[2]</sup> reported that Sr<sub>2</sub>TiSi<sub>2</sub>O<sub>8</sub> crystal performed oriented growth with polarizability along c-axis. This kind of fresnoite-type structure is flat sheets made up of [Si<sub>2</sub>O<sub>7</sub>]<sup>6-</sup> which are linked to TiO<sub>5</sub> pyramidal units. These stacks of sheets are held by large ions presented in coordination polyhedra<sup>[3]</sup>. The research of crystallization process in these transparent crystallized glasses usually needs more microscopy photos or spectra to provide the evidence of changes occurred in materials. Tanakashi et al<sup>[4]</sup> also reported that the temperature of the crystallization was a key factor in the second-order nonlinearity of Sr<sub>2</sub>TiSi<sub>2</sub>O<sub>8</sub>, but the proper ranges of temperature and time in the heat-treatment have not given yet for a good performance on nonlinear optical properties. At the same time, it will be better to perform a direct method to investigate the thermal crystallization process of these materials. So in this paper, we tried to make full use of Maker fringe patterns of transparent 2.0SrO-1.0TiO<sub>2</sub>-2.9SiO<sub>2</sub> glasses to study their crystallization dynamics at different annealing conditions.

The UV-vis-near IR transmission spectra of 2.0SrO-1.0TiO<sub>2</sub>-2.9SiO<sub>2</sub> glass samples are shown in Figure 4. 1. The transparent crystallized glasses were annealed for 2 hours at 790°C, 810°C, 830°C, 850°C, 870°C, 890°C and 910°C, respectively. All samples have a wide transmission window from NIR to UV with an absorption edge around 340nm which meant that these samples have almost the same optical band gap as as-treated glasses. The transmittance of these samples decreases quickly with increasing heat-treatment temperature from 830°C to 870°C comparing to the ranges from 0°C to 830°C and from 870°C to 910°C. These transmission spectra give the evidence of the information of crystallization in glass with heat-treatment.

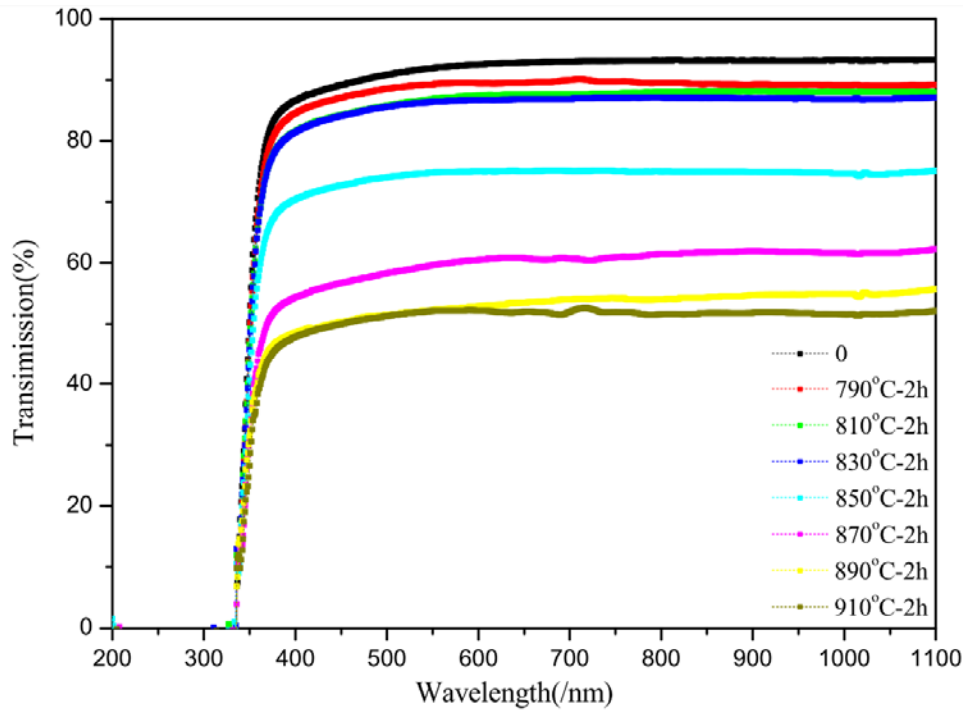


Figure 4.1 UV-Vis-near IR optical transmission spectra for as-treated samples and heat-treated glasses at  $T_{HT}=790^{\circ}\text{C}$  - $910^{\circ}\text{C}$  for 2 h.

The Maker fringe patterns of transparent crystallized glasses with annealing from  $790^{\circ}\text{C}$  to  $910^{\circ}\text{C}$  for 2 hours are shown in figure 4. 2. Obvious SH signals were observed at  $T_{HT}=850\text{-}910^{\circ}\text{C}$  for 2 hours, while no SH signal was detected at  $T_{HT}=790\text{-}830^{\circ}\text{C}$ . It was reported that TiO<sub>5</sub> pyramidal unit included one short Ti-O bonds along the c-axis and four longer Ti-O bands along the a-axis<sup>[3]</sup>, which was the origin of large SHG in fresnoite-type crystals such as Ba<sub>2</sub>TiGe<sub>2</sub>O<sub>8</sub> crystal. So it was speculated that enough non-central symmetry crystals appearing in glass would interrupt the symmetry and induce SHG in glasses. And the intensity of SH increased with the increasing of temperature. Moreover, the maximum SH intensity was at  $\theta=\pm 40^{\circ}$  and minimum was at  $\theta=0^{\circ}$  at  $T_{HT}=850\text{C-}2\text{h}$ . This might be due to the formation of oriented nonlinear crystals with a specific thickness in glass. When temperature was higher than  $890^{\circ}\text{C}$ , the obtained curves tended to become broader and the maximum intensity appeared at  $\theta=0^{\circ}$ . The presumed reason might be due to the appearance of randomly distributed nonlinear crystals in glass and form a thicker

thickness of crystallized layer which induced incoherent SH signals at 0°.

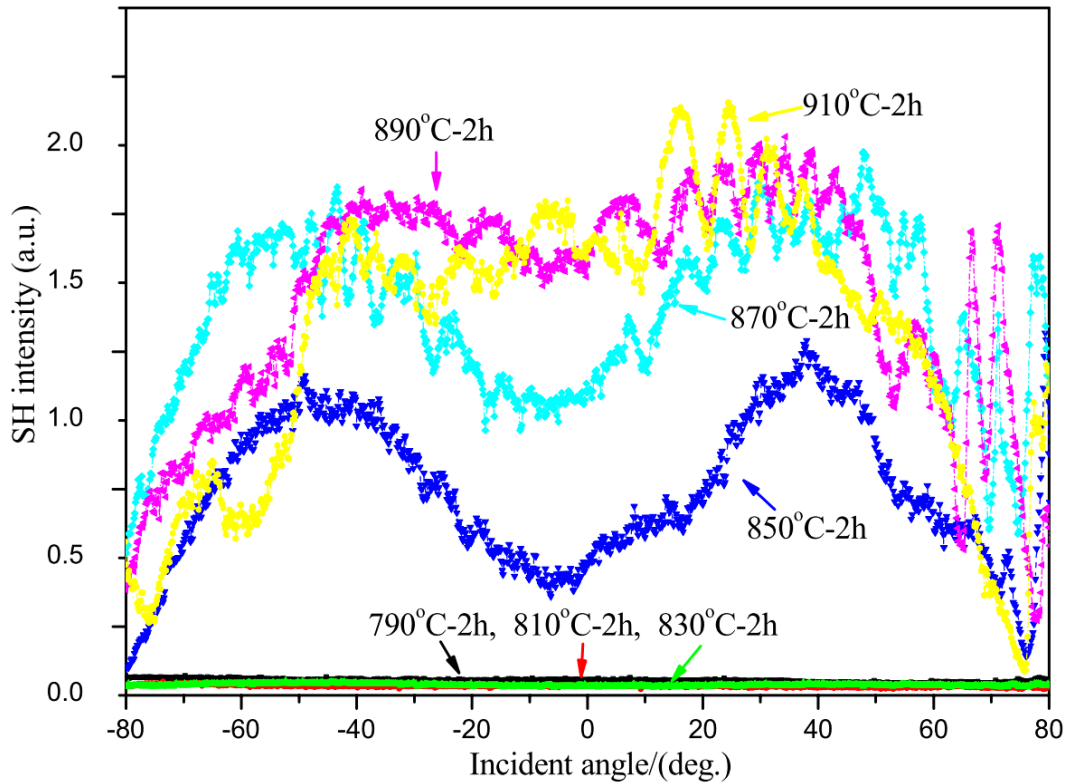


Figure 4.2 Maker fringe patterns for transparent crystallized glasses obtained by heat-treatments at  $T_{HT}=790^{\circ}\text{C}$  - $910^{\circ}\text{C}$  for 2 h.

To clarify our speculation, the surface XRD analyses were done in the as-treated and treated samples at  $850^{\circ}\text{C}$ . We chose three samples with characteristic Maker fringe patterns to investigate: as-treated glass, and heat-treated samples at  $850^{\circ}\text{C}$  and  $910^{\circ}\text{C}$ , both for 2 hours. It is clearly shown in figure 4.3 that there is no obvious crystallite phase for the as-treated glass. At  $850^{\circ}\text{C}$ , the relative intensity of peaks related to  $\text{Sr}_2\text{TiSi}_2\text{O}_8$  phase increased strongly. When the temperature was up to  $910^{\circ}\text{C}$ , the intensity of this strong peak increased slightly but the other tiny peaks corresponding to different plans became obvious.

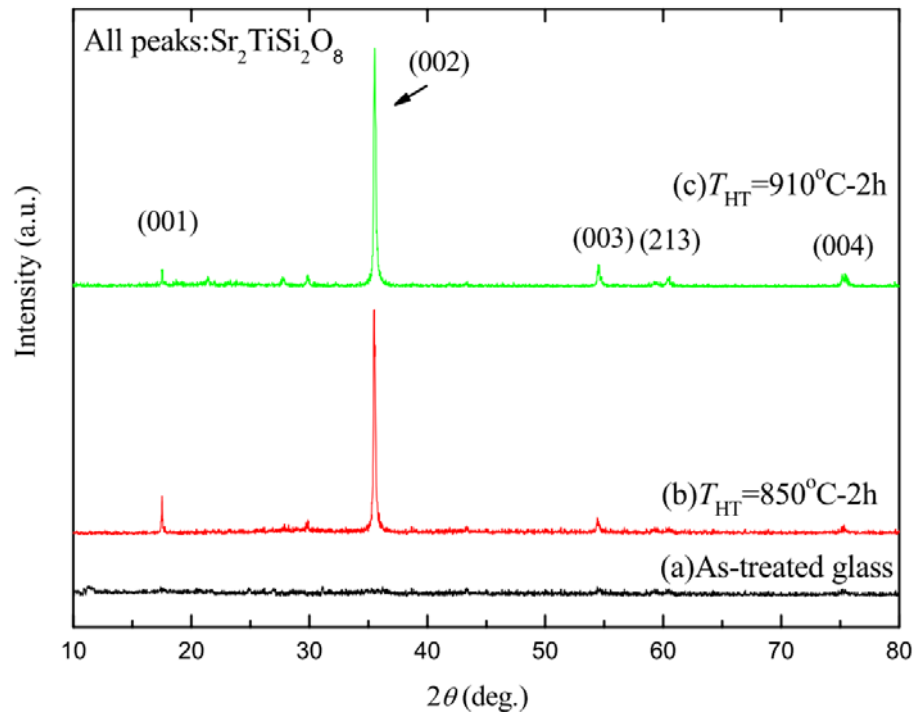


Figure 4.3 XRD patterns for the (a) as-treated glass and the surface region of transparent crystallized glasses heat-treated at (b) 850°C for 2h and (c) 910°C for 2h.

In order to observe the thickness of crystallization layer in glasses, figure 4.4 shows the SEM image of the surface and the cross-section (insert picture) of the heat-treated sample at 850°C for 2h. White points in the image represent crystallites, which are distributed almost homogeneously in the sample surface layer. The thickness of the layer is 15  $\mu\text{m}$  from the cross-section photograph, it indicated that the nucleus of crystallite grew and crystallized firstly at the surface and later in the interior of samples.

In the view of the SH signal appearance at 850°C for 2h, the temperature 850°C was selected as a significant temperature to investigate crystallization process by Maker fringe patterns. Figure 4.5 gives the result of Maker fringe measurements of samples annealed at 850°C for 2, 3, 4 and 5 hours. The SH intensity increased drastically with heat-treatment time from 2 to 3 hours. However, when the heat-treated time increased, the relative SH intensities of samples with heat-treatment time from 3 to 5 hours did not increase drastically. But, the pattern of fringes became

broader and the maximum value appeared at  $\theta=0^\circ$ , which was similar to the crystallization of samples annealed at different temperatures in figure 4.2. It probably originated from the appearance of a thick nonlinear layer of nonlinear crystals and the incoherent SH responses induced by randomly distributed nonlinear crystals in sample.

### 4.3 Discussion

In our experiments, when the samples were heat-treated in a critical condition, the nucleus grew and crystalline phase began to appear in glasses. It is observed from figure 4. 2 that there is no SH signal detected when the temperature increased from 0 to 830°C, which means that there is no or little non-central symmetric crystalline phase in glasses. When the temperature was up to 850°C, SH signals could be detected as shown in figure 4. 2. At this time, the nucleuses were formed easily in the surface layer because its nucleation energy was lower than that in the interior of glasses, and then grew freely in different direction. Small crystallites appeared and the surface crystallization was predominant.

The XRD patterns for 850°C-2h in figure 4.3 showed that the crystallization of Sr<sub>2</sub>TiSi<sub>2</sub>O<sub>8</sub> crystallite phase corresponding to plan (002) appeared well in the surface layer due to the presence of impurities that plays the role of nucleating agents and/or of the interface glass/air. Moreover, since the energy of Sr-O bond (402kJ/mol) which is parallel to c-axis is smaller the others (Si-O: 787kJ/mol; Ti-O: 703kJ/mol) and in order to minimization of the variation in the surface energy<sup>[5]</sup>, these precipitated crystallites preferred to grow along the direction of c-axis which was perpendicular to the sample surface. When Sr<sub>2</sub>TiSi<sub>2</sub>O<sub>8</sub> crystallites own tetragonal structures with a space group P4bm at room temperature and TiO<sub>5</sub> units in which bond length along c-axis is much shorter than that in other directions, its lattice energy along c-axis is also larger than that in other directions which leads this kind of crystal to perform second-order nonlinear property<sup>[6]</sup>, and the appearance of crystals in glass also results in that the transmission decreases drastically in figure 4.1. While the T<sub>HT</sub> increased continuously, larger SH intensities in transparent glass was observed in figure 4.2 and

4.5. Meanwhile, when the samples were treated at higher temperature or with longer time, more nonlinear crystals appeared in sample and different densities between crystalline phase and glassy phase shown in figure 4.4 affected the dimension (e.g. ratio  $c/a$ ) of the TiO<sub>5</sub> unit cell. As the second-order nonlinearity increased with increasing ratio  $c/a$ <sup>[7]</sup>, the performed larger SH intensities in figure 4.2 and 4.5 indicated that the occurrence of in unit cell dimension variation in glasses. Moreover, SH intensity increased because of the appearance of larger numbers of nonlinear crystals in spite of the decrease of transmittance at the same time. But with increasing the temperature or time continuously, for example, when the treated temperature was higher than 890°C or the time was longer than 3 hours, there were no large differences of SH intensity among these samples. It is speculated that the nucleuses are formed more stably and epitaxy are fuller in glasses. Meanwhile, the amount of surface nucleation becomes larger and then tends to be saturated. Small granular crystals begin to appear in the interior of glasses. These granular crystals induce the disordered growth in glasses, but also prevent the grain orientating near to the surface. These were confirmed in figure 4.3 that the intensity of tiny peaks corresponding different plans of the sample treated at 910°C for 2h became larger and the intensity of this strong peak increased slightly comparing to the sample treated at 850°C for 2h. At the same time, these randomly distributed nonlinear crystals making up a thicker effective nonlinear layer and the scattering of SH waves by crystallites precipitate in the interior of glasses were both contributed to broader Maker fringes patterns and maximum SH intensity at 0°. Moreover, when the existence of grain boundary of crystals, the scattering of the incident and SH waves became minimum which induced the maximum SH intensity at the angle of 0° as well<sup>[8]</sup>. Therefore, the crystallization started from the surface to the interior of our glassy sample which was analyzed from Maker fringe patterns.

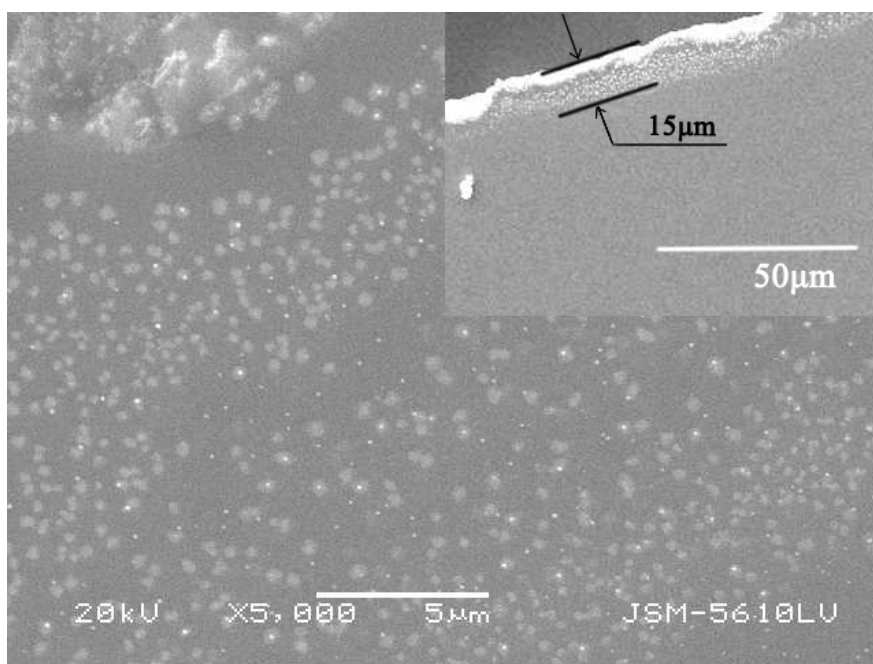


Figure 4.4 SEM images of the surface and the cross-section (insert picture) heat-treated at  $T_{HT}=850^{\circ}\text{C}$  for 2h.

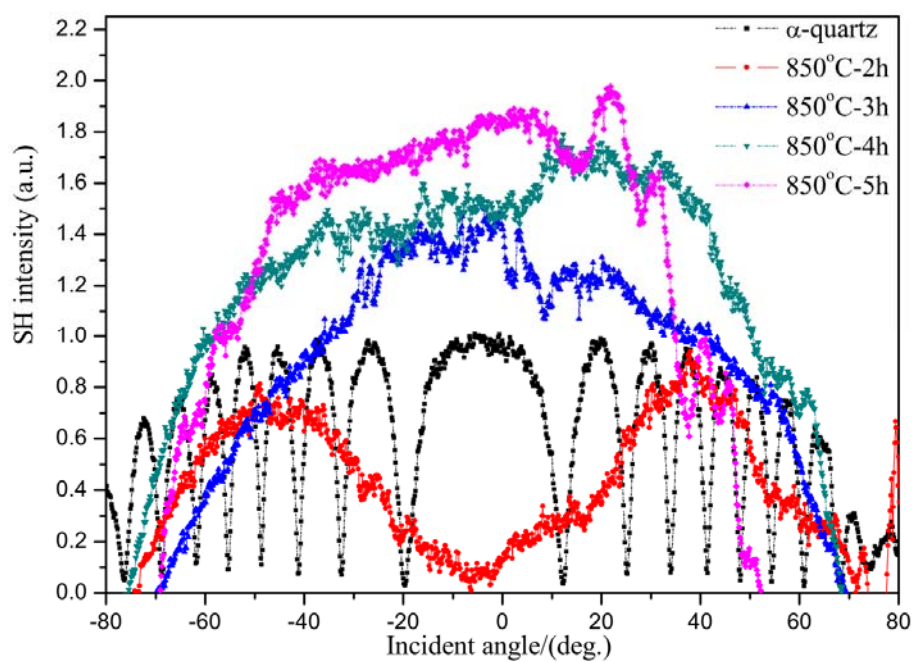


Figure 4.5 Maker fringe patterns of  $\alpha$ -quartz and transparent crystallized glasses obtained by heat-treatments at  $T_{HT}=850^{\circ}\text{C}$  for 2h-5h.

### Maker Fringes simulations

Furthermore, in order to understand well the mechanism of induced SHG in thermally induced glass, we also have taken simulation in Maker fringes method and calculation is presented in Annex I.

Maker fringes measurement was carried out at first using a referred quartz cut parallel to Z-axis (included in cut plane) with thickness  $L=1.830$  mm. The other parameters used in the simulation were  $n_o=1.534$ ,  $n_{2o}=1.547$ ,  $d_{11}=0.34$  pm/V and  $d_{14}=0.006$  pm/V respectively. The experimental and simulated results are presented in figure 4.6 (a) and 4.6 (b).

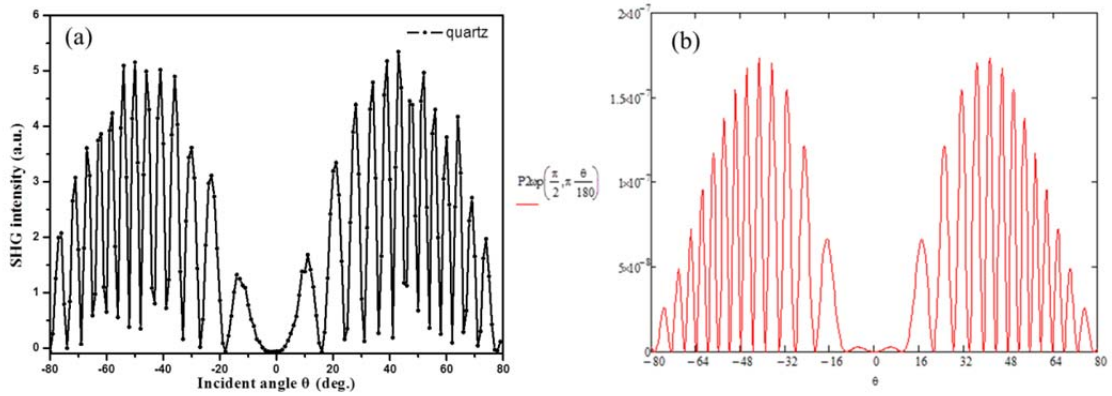


Figure 4.6 Maker fringe patterns of a commercial z-cut quartz plate with polarization “p” (a) and calculated Maker fringe patterns (b) with the same polarization and thickness

The coherent length of quartz is  $L_{\text{coh}} = \lambda / 4(n_{2o} - n_o) = 20.46\mu\text{m}$ . Comparing the figures above, between  $-80^\circ$  to  $80^\circ$ , we can see that the number of fringes of simulated curves goes well with that of experimental data when parameters for calculation are the same as that used in experiments. The form of intensity envelope of these two curves is also similar to each other.

Furthermore, we also compared the simulated patterns with that of thermally poled niobium borophosphate glasses<sup>[9]</sup> with applying the same parameters for calculation:  $\lambda=1064\text{nm}$ ,  $n_o=1.93$ ,  $n_{2o}=1.98$ , waist of beam= $100\mu\text{m}$ , thickness  $L=4.4\mu\text{m}$ ,  $d_{31}=1.25$  pm/V= $3d_{33}$ <sup>[9]</sup>,

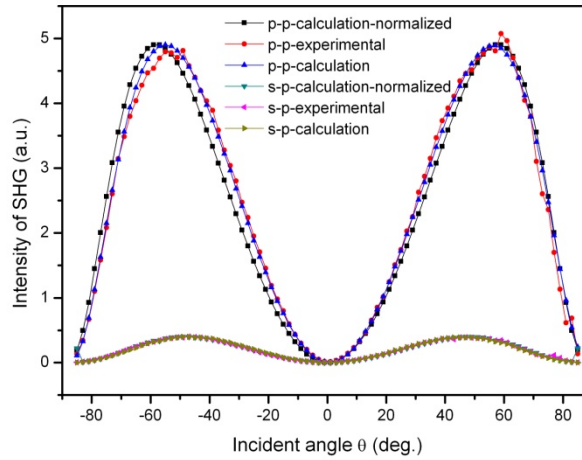


Figure 4.7 Calculated transmitted SHG Maker-fringes patterns (@ MAP/LPCES/ICMMO/PSUD, black and green lines) and experimental and calculated transmitted SHG Maker-fringes patterns (@ Bordeaux, red, blue, pink and brown lines) for thermally poled glass<sup>[9]</sup>

The black line with square presents the calculated transmitted SHG Maker-fringes pattern in MAP/LPCES/ICMMO/PSUD, which is normalized with respect to the calculated data of blue line by Bordeaux ( $p$ - $p$ :  $I_{@MAP} / I_{@Bordeaux} = 8$  and  $s$ - $p$ :  $I_{@MAP} / I_{@Bordeaux} = 6.62$ ). As it is shown in the figure 4.7, even though the shape and number of the fringe of our simulated curve and theirs are similar or nearly the same, there is always a small displacement of the maxima position in the case of  $p$ - $p$ : at the side between  $-80^\circ$  and  $0^\circ$ , the maxima position of calculated pattern by Bordeaux moves a little towards to the  $0^\circ$ . Between  $0^\circ$  to  $80^\circ$ , at the right side, the displacement of maxima position is less than that of the left side (but normally, it should be symmetric as shown by our simulation). Contrarily, our simulated result in case of  $s$ - $p$  matches well with that of published results.

Actually, the intensity of harmonic wave is proportional to the product of effective susceptibility tensor  $d_{eff}$ , sample thickness  $L$  and the term  $\Delta k$  related to mismatched-phase which can be expressed as follows:

$$I_{2\omega} \propto L_e^2 d_{eff}^2 \left( \frac{\sin\left(\frac{\Delta k L_e}{2}\right)}{\frac{\Delta k L_e}{2}} \right)^2 \quad (4.3.1)$$

This expression reveals that, when incident angle  $\theta$  is zero, the two necessary conditions to get nonzero  $I_{2\omega}$  are non-vanished value  $d_{eff}$  and nonzero oscillated term  $\sin(\Delta k L_e / 2)$ .

Figure 4.8 shows the evolution of SH intensity in terms of sample thickness when the incident beam is normalized to the input face. The minimums ( $I_{2\omega}=0$ ) appear at  $2nL_{coh}$  ( $n=1, 2, \dots, N$ ) while the maximums at  $(2n-1)L_{coh}$ . Therefore, When the polarization is perpendicular to the plan of incidence (in the direction “s”), because of the effective tensor  $d_{eff}=d_{11} \neq 0$ , we can get the s component of  $I_{2\omega}$  at  $0^\circ$  is nonzero with assuming that sample thickness is not  $2nL_{coh}$ . But in case of “p” component here, as  $d_{eff}=0$ , we can only obtain zero intensity on this configuration.

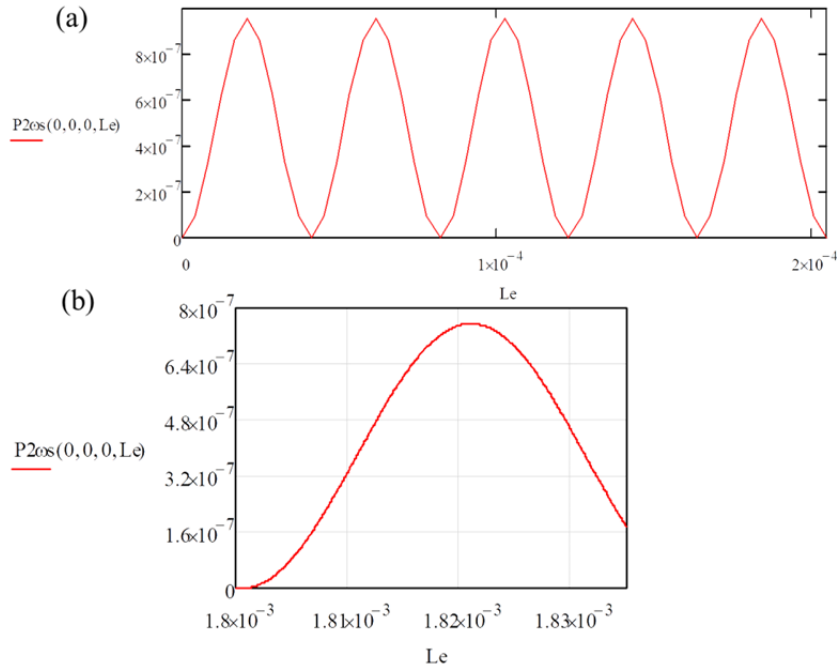


Figure 4.8 Calculated transmitted SHG Maker-fringes intensity as function of sample thickness  $L_e$  of Z-cut quartz at “s”, and (b) is a magnification of (a).

We go back to simulate the second-order nonlinear property of thermally

induced nano-crystallized STS. The refractive indexes at harmonic wave  $n_{2\omega}$  and at fundamental wave  $n_{\omega}$  are 1.738 and 1.718, respectively. The point group of thermally treated STS glass at 850°C-2h is  $C_{\infty v}^{[10]}$  and its second-order tensor matrix should be:

$$\begin{pmatrix} 0 & 0 & 0 & 0 & d_{31} & 0 \\ 0 & 0 & 0 & d_{31} & 0 & 0 \\ d_{31} & d_{31} & d_{33} & 0 & 0 & 0 \end{pmatrix}$$

The simulated Maker fringes as shown in figure 4.9

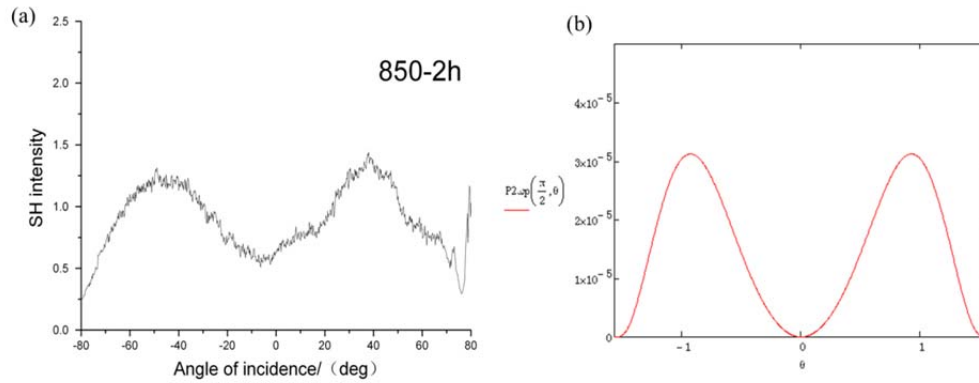


Figure 4.9 The obtained Maker fringes in experiment (a) and in simulation (b) of the sample heated at 850°C for 2h

Two similar envelopes of patterns can be observed and the maximum can be found around  $\pm 45^\circ$  both in figure 4.9(a) and (b). But low SH intensity obtained at  $0^\circ$  in the experiment might mostly come from incoherent SH signals due to the randomly distributed crystals inside or the uncertain interface defects between the amorphous matrix and crystallized layer. If bulk crystallization occurs then, high SH intensity at  $0^\circ$  can be obtained. Since the second-order nonlinear property depends on the thickness of nonlinear layer, the key point to modulate it in case of heat treated glass is to control well the temperature and time of thermal treatment.

## 4.4 Conclusions

Fresnoite-type crystallized 2.0SrO-1.0TiO<sub>2</sub>-2.9SiO<sub>2</sub> glass was prepared by conventional melt-quenching method. The Maker fringe patterns of different heat-treatment conditions were used to discuss the time-dependence and

temperature-dependence of crystallization dynamics. The appearance of crystallite phase in glass induced the decline of transmittance with the augmentation of treated temperature. The different trends of Maker fringe patterns corresponded with different crystallization process, which was verified by XRD analyses and SEM images. It was indicated that the surface crystallized firstly and then the crystalline phase appeared in the interior of glasses. So Maker fringes measurement can be used as not only a characterization method for SHG but also a means to study the crystallization process with the help of related simulation in crystallized transparent glasses.

## Reference

- [1]. Liu, Q. M., Zhao, X. J., Tanaka, K., *et al.*, Second-harmonic generation in Ge-As-S glasses by electron beam irradiation and analysis of the poling mechanism. *Opt Commun* **2001**, *198* (1-3), 187-192.
- [2]. Wang, H. C., Liu, Q. M., Cheng, J. S., Field-assisted Isothermal Oriented Crystallization of SrO-TiO<sub>2</sub>-SiO<sub>2</sub> Polar Glass-Ceramics. *Adv Mat Res* **2009**, *66*, 49-52.
- [3]. Moore, P. B., Louisnathan, John, Fresnoite: Unusal Titanium Coordination. *Science* **1967**, *156*, 1361-1362.
- [4]. Takahashi, Y., Benino, Y., Fujiwara, T., *et al.*, Formation mechanism of ferroelastic Ba<sub>2</sub>TiGe<sub>2</sub>O<sub>8</sub> and second order optical non-linearity in transparent crystallized glasses. *J Non-Cryst Solids* **2003**, *316* (2-3), 320-330.
- [5]. Maury, N., Cambier, F., Gonon, M., Bulk crystallisation of (001) oriented fresnoite Sr<sub>2</sub>TiSi<sub>2</sub>O<sub>8</sub> in glass-ceramics of the Sr-Ti-Si-K-B-O system. *J Non-Cryst Solids* **2011**, *357* (3), 1079-1084.
- [6]. Hoche, T., Neumann, W., Esmailzadeh, S., *et al.*, The crystal structure of Sr<sub>2</sub>TiSi<sub>2</sub>O<sub>8</sub>. *Journal of Solid State Chemistry* **2002**, *166* (1), 15-23.
- [7]. Takahashi, Y., Benino, Y., Fujiwara, T., *et al.*, Large second-order optical nonlinearities of fresnoite-type crystals in transparent surface-crystallized glasses. *J Appl Phys* **2004**, *95* (7), 3503-3508.
- [8]. Gu, S. X., Hu, H. P., Guo, H. T., *et al.*, Second-harmonic generation in transparent surface crystallized GeS<sub>2</sub>-Ga<sub>2</sub>S<sub>3</sub>-CdS chalcogenide glasses. *Opt Commun* **2008**, *281* (9), 2651-2655.
- [9]. Malakho, A., Dussauze, M., Fargin, E., *et al.*, Effect of sodium to barium substitution on the space charge implementation in thermally poled glasses for nonlinear optical applications. *J Solid State Chem* **2009**, *182* (5), 1156-1163.
- [10]. Ding, Y., Masuda, N., Miura, Y., *et al.*, Preparation of polar oriented Sr<sub>2</sub>TiSi<sub>2</sub>O<sub>8</sub> films by surface crystallization of glass and second harmonic generation. *J Non-Cryst Solids* **1996**, *203*, 88-95.

## Chapter 5 Photo-induced oriented nano-crystals in LNS glass by fs laser irradiation

In this chapter, the space-selectively induced oriented  $\text{LiNbO}_3$ -like crystals from  $\text{Li}_2\text{O-Nb}_2\text{O}_5\text{-SiO}_2$  (LNS) silica-based glasses with fs laser irradiation will be investigated. We will focus on the oriented  $\text{LiNbO}_3$ -like crystals in nano-size by fs laser irradiation. Optical properties have been also investigated in nano-crystallization range.

### 5.1 Experimental details

#### Sample preparation

The precursory  $33\text{Li}_2\text{O-33Nb}_2\text{O}_5\text{-34SiO}_2$  (LNS glass) was elaborated in traditional method as introduced in chapter 3. After that, the glass samples were cut and mirror-polished with a size of 2 mm x 10 mm x 10 mm, which were then used for the irradiation experiments using a microscopic objective (NA=0.6).

Laser lines writing process was undertaken using the femtosecond laser system (Satsuma, Amplitude Systèmes Ltd.) at 1030 nm and delivering pulses of 300 fs. The laser beam motion ( $v$ ), pulse energy ( $E$ ) and polarization ( $e$ ) were controlled by a 5D stage-control software (Gol3D from GBCS). To avoid surface ablation due to the presence of the glass sample surface, the beam was focused at 350  $\mu\text{m}$  in depth using a microscopic objective (NA=0.6). All of the laser lines were written with first static irradiation for 5 seconds and then written continuously at different scanning velocities.

#### Static irradiation

Firstly, by doing static irradiation, the crystallization «boundaries» in our glass composition have been determined (see figure 5.1) according to pulse energy (0.1 up to 2.5  $\mu\text{J}$ ), repetition rate (1-500 kHz) and writing speed (1-500  $\mu\text{m/s}$ ). At higher frequency, e.g. 500 kHz, the crystallization occurs at 0.3 $\mu\text{J}$  and large cracks were generated around 2.2 $\mu\text{J}$ . At low repetition rate, 200 kHz, no cracks appeared but

nonlinear crystals were firstly formed at 1.3  $\mu\text{J}$ . Hence, a moderate frequency 300 kHz was chosen for laser writing. In laser writing experiments, we varied laser beam pulse energy ranging from 0.1 up to 2.5  $\mu\text{J}/\text{pulse}$  with a scanning speed at  $5\mu\text{m}/\text{s}$ . Laser pulses passed through energy and polarization controller and then they were focused by a microscopy objective in the sample. We defined that the laser lines were written along the x-axis, the laser beam propagating along the z-axis with the linear polarization along the x-axis (polarization parallel to writing direction) or along the y-axis (polarization perpendicular to writing direction). Therefore, the cross-section of laser tracks is in the y-z plane.

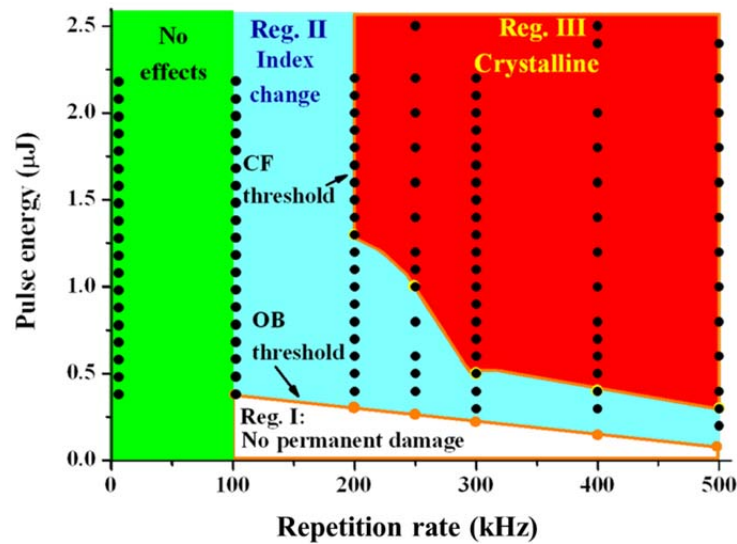


Figure 5.1. Pulse energy versus repetition rate with different processing thresholds of femtosecond laser interaction with LNS glass. Other laser parameters: OB: optical breakdown; CF: crystallization formation. Dots in the graph indicate the investigations performed in this work<sup>[1]</sup>.

## 5.2 Experimental results

### 5.2.1 Photo-induced oriented crystallization in glass

#### Laser-induced oriented crystallization

In order to understand the laser-induced crystallization process, series of EBSD mapping according to laser pulse energy were carried out. As shown figure 5.2(a), all

of the laser tracks were profiled in red dashed-line. It exhibited that the width of the interaction volume became smaller from  $9\mu\text{m}$  to  $3\mu\text{m}$  when the pulse energy decreased from  $2.0\ \mu\text{J}$  down to  $0.6\ \mu\text{J}$ . Meanwhile, the significant development of crystal size and orientation were revealed by the EBSD images as well. It was pronounced that a large part of pink color in the trace appeared at  $2.0\ \mu\text{J}$ . It indicates that polar axis, i.e. c-axis  $\langle 0001 \rangle$ , of crystals at the center of laser trace orients in the x-axis with a small dispersion. When decreasing the pulse energy to  $1.2\ \mu\text{J}$ , the big red part disintegrated into several micro-sized pieces with different colors and the size of this laser trace decreases in micro scale sharply. Moreover, c-axis of nonlinear crystals located at the center of laser trace began to lie in the y-z plane as indicated by the green colored sector. After then, when energy is decreased, for example from  $1.0\ \mu\text{J}$  to  $0.6\ \mu\text{J}$ , the size of those green colored pieces turned to be much smaller than  $1\ \mu\text{m}$  and down to  $100\ \text{nm}$ .

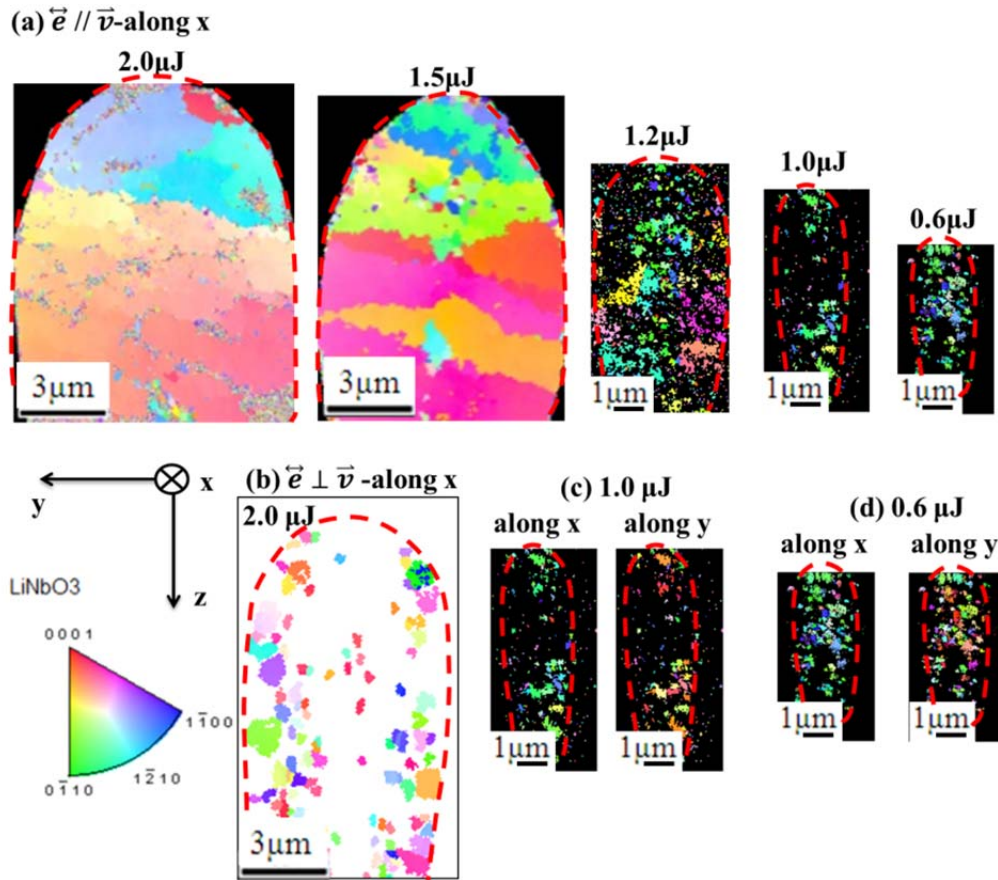


Figure 5.2 EBSD scan images of written line cross-sections irradiated at 2.0 to 0.6  $\mu\text{J}$  (with polarization parallel  $\vec{e}$  to the laser motion direction  $\vec{v}$ ) coding the crystal orientation along x (a). (b) EBSD images coding crystal orientation along x of written line cross-sections irradiated at 2.0  $\mu\text{J}$  with a polarization perpendicular to the scanning direction. EBSD scan image coding the crystal orientation are along x axis and along y axis at 1.0 $\mu\text{J}$  (c) and 0.6 $\mu\text{J}$  (d), respectively. The polarization for writing is parallel to the laser motion direction. Laser tracks were profiled in red dashed-line. Other laser parameters: 300 kHz, 5  $\mu\text{m/s}$ , 300 fs, 1030 nm, NA = 0.6

### Laser-induced oriented nano-crystallization

Similarly, the influence of the writing polarization orientation (parallel or perpendicular) on the orientation of fs laser-induced  $\text{LiNbO}_3$ -like crystals was investigated. The writing polarization was turned at 90 degree i.e. perpendicular to the writing direction, and it was surprising to discover very different crystallization

results as shown in figure 5.2(b). The laser tracks exhibiting a needle shape with a maximum width of 6  $\mu\text{m}$  which was smaller than that at 2.0 $\mu\text{J}$  in figure 5.2(a). Furthermore, EBSD image of the cross-section showed that fragmental crystallization of nano-size or smaller than 1  $\mu\text{m}$  takes place. A large portion of disoriented  $\text{LiNbO}_3$ -like crystals were randomly distributed. These results indicate fs laser-induced crystallization in LNS glass strongly depends on the polarization direction of the incident laser radiation.

Moreover, as observed from figure 5.2(a), nano-crystallization can be obtained at low pulse energy. For precising the nano-crystals orientation, EBSD images of laser track cross-section coding crystals orientation along x and along y were compared as shown in figure 5.2(c). Most of the crystals were green color coded in “along x” image but several red colored pieces could be still observed at 1.0 $\mu\text{J}$ . This means a small fraction of crystals orientates parallel to laser scanning direction. In case of laser writing at 0.6 $\mu\text{J}$ , despite the fact that the exhibited majored green color was similar to that at 1.0 $\mu\text{J}$  in “along x” image of figure 5.2(d), the presence of red and green colors in “along y” image suggested that part of crystals oriented along y-axis and parts along z-axis, respectively. This indicates that they are always in the perpendicular plane to the laser lines.

## 5.2.2 Chemical analysis of laser-induced crystallization

### Micro-Raman spectroscopy results

Although the space group symmetry of precipitated crystals can be analyzed SEM-EBSD technology, the crystal type should be still verified through other methods. In this point of view, Micro-Raman measurement has been carried out in the irradiated sample to give some information of precipitated crystals.

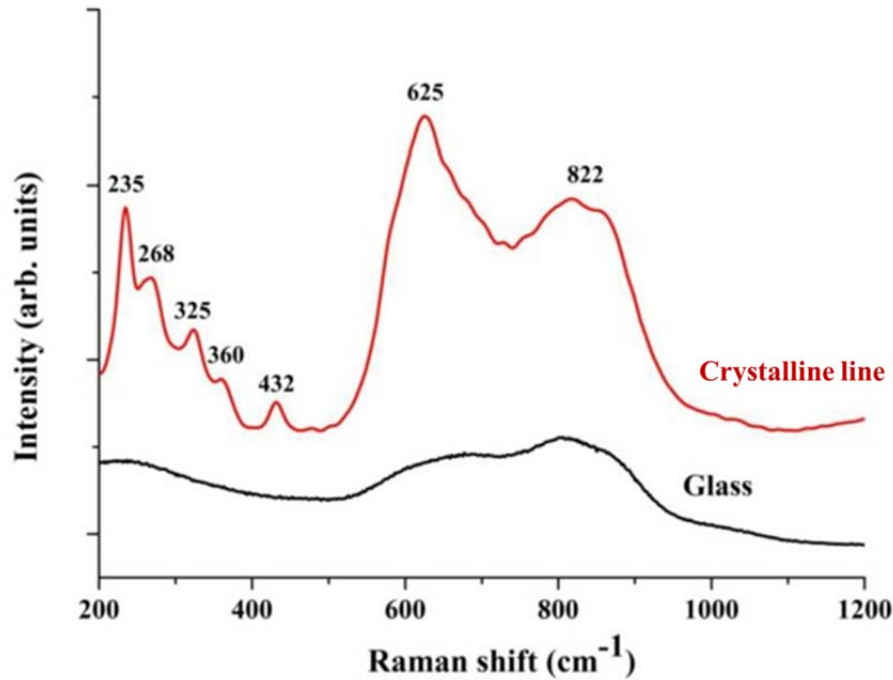


Figure 5.3 Micro-Raman scattering ( $\text{Ar}^+$  laser 515 nm) spectra at room temperature for unirradiated area (black curve) and the irradiated crystalline line (red curve) in LNS glass. Laser parameters: 300 kHz, 1.5  $\mu\text{J}$ , 5  $\mu\text{m/s}$ , 300 fs, 1030 nm,  $\text{NA} = 0.6$ ,  $\vec{e} \parallel \vec{v}$ .

The characterized peaks of  $\text{LiNbO}_3$  are exhibited at 237, 268, 325, 360, 432, 625  $\text{cm}^{-1}$ <sup>[2]</sup> in figure 5.3 in red line while the black presents Raman spectra of amorphous glass substrate. The bands exhibited at 237, 268 325, 360, and 432  $\text{cm}^{-1}$  are attributable to the  $E_1(\text{TO})$  modes which is a characteristic vibrational modes of  $[\text{NbO}_6]^{7-}$  octahedra in  $\text{LiNbO}_3$  crystals. The  $A_1(\text{TO})$  mode, another characteristic vibrational mode, emerges at 625  $\text{cm}^{-1}$  and it is associated with the stretching vibration of the Nb-O bond. The broad band near 822  $\text{cm}^{-1}$  is assigned either to the short vibration of Nb-O in  $\text{NbO}_6$  octahedral with non-bridging oxygen or a quantity distortion of  $\text{NbO}_6$  octahedra<sup>[3]</sup>.

### EDX and WDS results

From the previous EBSD maps and Raman spectroscopy results, the formation of  $\text{LiNbO}_3$  crystal in glass by fs laser irradiation is proved. However, inasmuch as the existence of  $\text{SiO}_2$  (nearly 1/3 in mol%) in original glass composition while no  $\text{SiO}_2$

appears in  $\text{LiNbO}_3$  crystalline phase, two hypothesis have been identified regarding the composition of this photo-induced crystallized glass. It may be either:

- i) unique phase  $\text{LiNbO}_3$ : in this case, Si must depart from the crystallized zone to form  $\text{LiNbO}_3$  phase without Si;
- ii) majority phase  $\text{LiNbO}_3$  mixed with other Si-based nano-sized crystals which is not detectable by EBSD and Raman spectra. Noticeably, Si has the possibility to stay in the crystalline zone in the latter case.

To take an insight to this, a series of chemical analysis has been taken as EDX (Energy-dispersive X-ray), WDS (wavelength-Dispersive spectroscopy) and nuclear microprobe on the cross section (in y-z plane) and also along the laser (in x-axis).

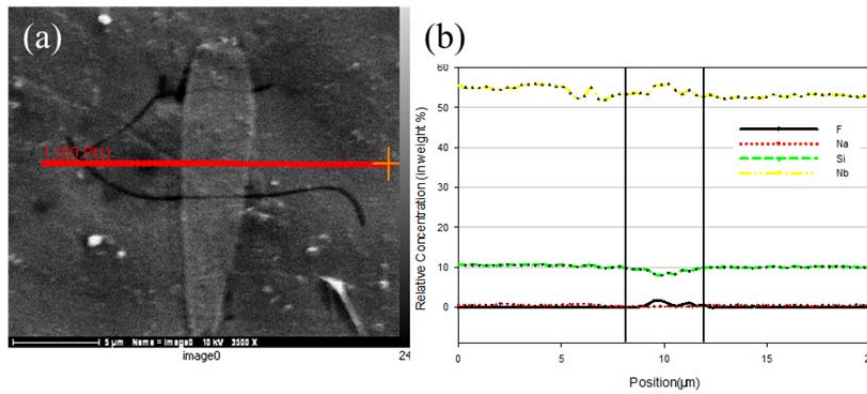


Figure 5.4: SEM image (a) and EDX line-scanning spectra (b) of the cross-section of laser trace written at  $0.9\mu\text{J}$ ,  $5\mu\text{m/s}$ ,  $300\text{ kHz}$ ,  $300\text{ fs}$ ,  $\text{NA}=0.6$ ,  $\vec{e} \parallel \vec{v}$ . The position of laser trace in (a) corresponds to the region between the two black lines in (b).

#### On the cross-section:

The relative concentration (in wt. %) of elements, such as Nb, Si, Na and F (and sometimes Na and F were induced by etching process), was obtained by EDX spectra which have been recorderd along the crossing line (y-z plane) with a  $1\mu\text{m}$  step. The concentrations (in wt. %) of Nb and Si in the virgin glass are about 52% and 10%, respectively. Considering the concentration profiles of Nb and Si, there is no obvious difference between the virgin and irradiated areas of the sample. Furthermore, the concentration of element O was measured independently by WDS as shown in figure 5.5. Similarly, no evident fluctuation of concentration of Si has been observed from

WDS spectra. However, the behavior of light element cannot be determined by these two methods. Therefore, nuclear microprobe has been taken in the laser cross-section to provide insight on the Li behavior as well as other elements.

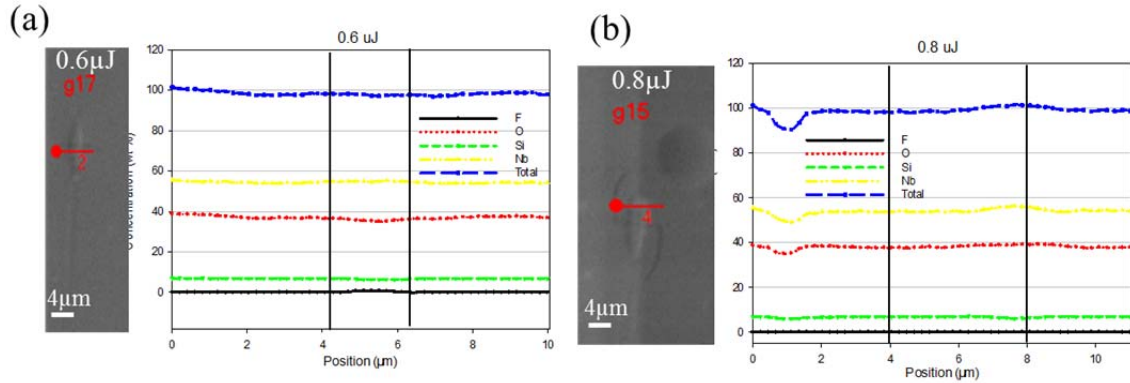


Figure 5.5: SEM image (left) and WDS line-scanning spectra (right) of the cross-section of laser trace written at 0.6  $\mu\text{J}$  (a) and at 0.8  $\mu\text{J}$  (b). Other laser parameters: 5  $\mu\text{m/s}$ , 300 kHz, 300 fs, NA=0.6,  $\vec{e} \parallel \vec{v}$ . The position of laser trace in (a) involves the region between the two black lines in (b).

As shown in figure 5.6, the concentration of Li in the cross-section was detected firstly by nuclear microprobe in using protons beam at 2600 keV. The scanned area is 14 x 14  $\mu\text{m}^2$  including one laser trace inside. The homogeneous cartography of distribution of Li element implies that no migration occurred after fs laser irradiation at 0.9  $\mu\text{J}$ .

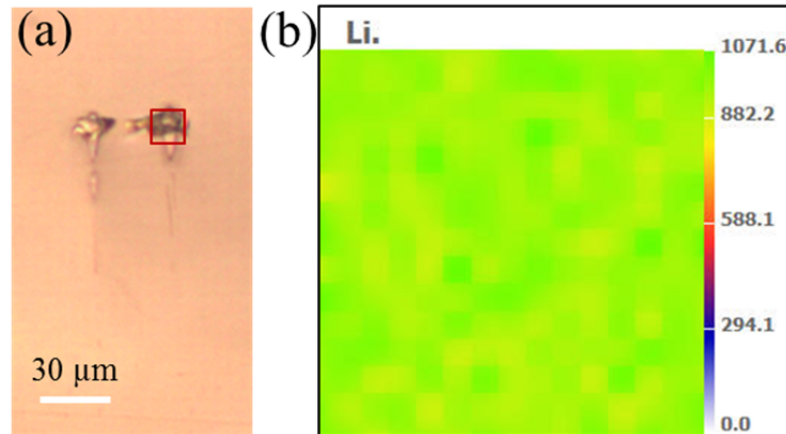


Figure 5.6: Optical image (a) of pairs of laser traces in y-z plane and concentration mapping of Li element (b) of one laser trace written at  $0.9 \mu\text{J}$  (the one inside the red box in fig. 5a). Other laser parameters:  $5 \mu\text{m/s}$ ,  $300 \text{ kHz}$ ,  $300 \text{ fs}$ ,  $\text{NA}=0.6$ ,  $\vec{e} \parallel \vec{v}$ . The cartographic area is  $14 \times 14 \mu\text{m}^2$  in red rectangle.

Similarly, another pair of laser traces was also examined by nuclear microprobe at  $1650 \text{ keV}$  to obtain the distribution of both Si and Li at the same time as shown in figure 5.7. A larger scanned area  $70 \times 35 \mu\text{m}^2$  was achieved. From figure 5.7, the homogeneous distribution of colors represents no fluctuation of Si and Li concentration in the detected area. This resemblant result to that exhibited in figure 5.6 implies that neither Li nor Si migrates in glass after fs laser irradiation, and this process is independent on the applied pulse energy.

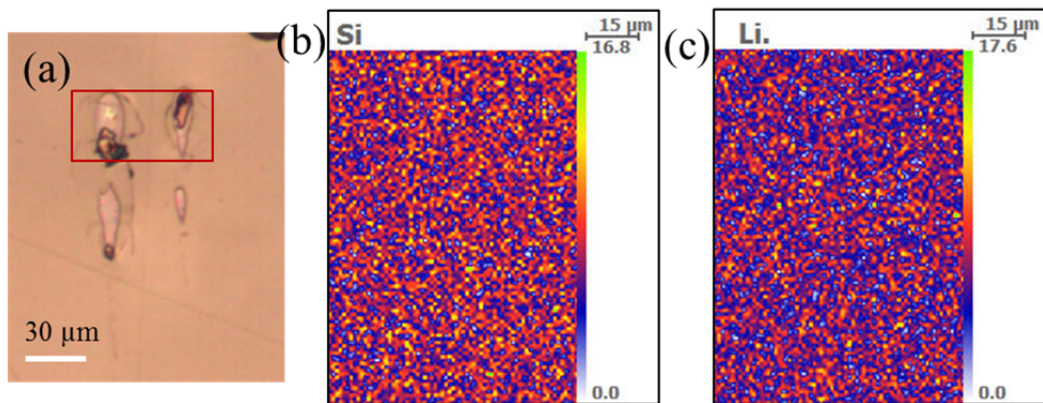


Figure 5.7: Optical image (a) of pairs of laser traces in y-z plane and concentration mapping of Si (b) and Li elements (c) of laser traces written at  $1.9 \mu\text{J}$ . Other laser parameters:  $5 \mu\text{m/s}$ ,  $300 \text{ kHz}$ ,  $300 \text{ fs}$ ,  $\text{NA}=0.6$ ,  $\vec{e} \parallel \vec{v}$ . The cartographic area is  $70 \times 35 \mu\text{m}^2$  in red rectangle.

**Along the laser lines:**

This irradiated sample was polished in xy plane. After etched by HF acid at the same condition in chapter 3, pairs of laser tracks in xy plane can be observed by SEM and the transversal and longitudinal EDX line-scanning were achieved and images in figure 5.8. In transversal line-scanning spectra, the relative concentration of Si remains nearly unchanged while that of Nb oscillates unregularly. In longitudinal spectra, no obvious change of relative concentration of Si and Nb is observed excepted that a dip of Si curve (figure 5.8 (b)) was formed on account of defects on the surface as noted in red circle.

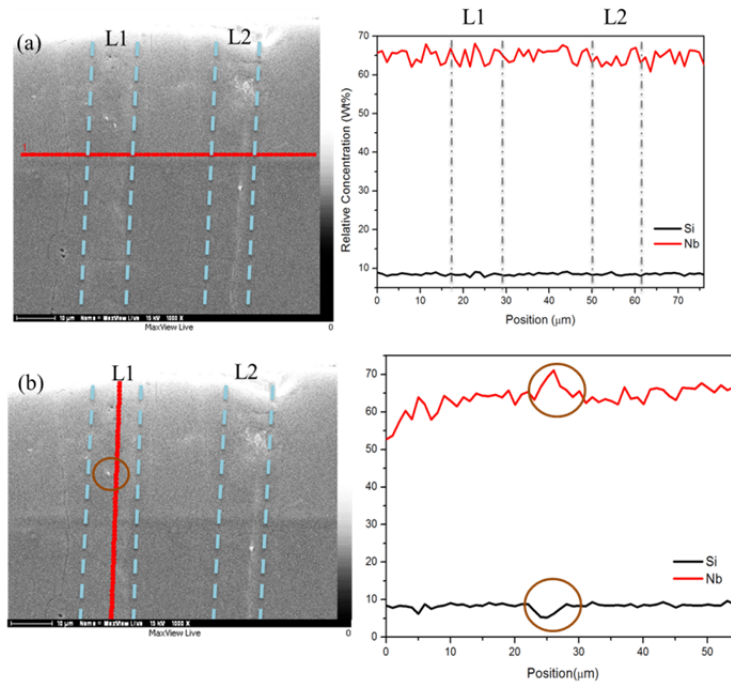


Figure 5.8: SEM image of pair of laser traces in xy plane (left) and EDX line-scanning spectra of Si and Nb elements (right) of laser traces written in transversal (a) and in longitudinal (b) direction, respectively. Other laser parameters:  $2.0 \mu\text{J}$ ,  $5 \mu\text{m/s}$ ,  $300 \text{ kHz}$ ,  $300 \text{ fs}$ ,  $\text{NA}=0.6$ ,  $\vec{e} \parallel \vec{v}$ . The blue dashed lines gave the outlines of these two laser tracks in glass.

**5.2.3 The orientation of nano-crystallization by SHG**

$\text{LiNbO}_3$  carries a polar axis with a strong and dominant nonlinear coefficient  $d_{33}$ . This allows us to consider approximately a small crystal lithium niobate as a macro

dipole with nonlinear coefficient  $d_{33}$ . Therefore, only crystallites oriented with the c axis parallel to polarization direction can give a strong SHG signal. In this case, a series of SHG experiments has been taken to demonstrate the orientation of crystals induced by fs laser irradiation.

### **Polarization dependence**

SHG microscopy images were carried out with the same experimental set up as laser writing process but at lower repetition rate i.e. 100 kHz. Two parallel laser lines were spaced with 30  $\mu\text{m}$  as shown in figure 5.9(a), where linear polarized fundamental waves were introduced parallel to the writing direction. The appearance of green light demonstrates that the acquired crystals here possess second-order nonlinear optical property which also prefigure that the crystallization was not homogeneous because of non-uniform distributed green light. As a consequence, we discovered that the orientation of polar axis was more uniform at 0.5  $\mu\text{J}$  than at higher pulse energies although weaker.

Although the direction of crystals can be investigated along a cross section by EBSD analysis, the nonlinear optical property in macroscopic way of laser-induced crystallized lines was still unknown. Moreover, the SH intensity is sensitive to the orientation of polar axis of nonlinear crystal. Therefore, the quality of the orientation of crystals in lines was studied here by normalized SH intensity measurement as a function of probing polarization azimuth in figure 5.9(b). For example, for a given single crystal, SH intensity is maximum when probing polarization is parallel to the polar axis of crystals and minimum in the perpendicular case. If the crystals are randomly oriented, there is no angular dependence. In the case of textured material which may exhibit different preferential orientations, the situation is intermediate. From figure 5.9(b), a characteristic sine-form pattern was observed at 0.5 J and 0.7 J. This means that the line is textured i.e. there is a preferential orientation of the c-axis in one direction. The maximum and minimum SH intensity was obtained at  $90^\circ$  and  $0^\circ$ , respectively. It figured out that the preferential orientation of polar axis was perpendicular to the laser motion direction. Besides, the minimum intensity at 0.5 J closer to 0 indicated that a larger fraction of crystals orientated perpendicularly to the laser lines than at 0.7 J. These were roughly coincident with the results deduced by

EBSM at low pulse energy (i.e. at 0.6 J) as seen in figure 5.2(d). When the pulse energy was increased to 1.0 J, the maximum intensity was obtained at  $90^\circ$  as well. However, a pronounced small peak of SH intensity appeared at the angle of  $0^\circ$ . This was mostly due to a small fraction of  $\text{LiNbO}_3$  crystals orientated parallel to the laser lines with remaining the dominant preferential orientation perpendicular to the scanning direction as displayed by EBSM image in figure 5.2(c). Because EBSM is recorded from a thin layer in depth (here the cross section of the line is in y-z plan) and SH measurements display homogeneity along x-axis going through the line along z-axis, so the analyzed volume is different. The observation of a discrepancy between figure 5.2(d) and figure 5.9 (a) is thus not surprising.

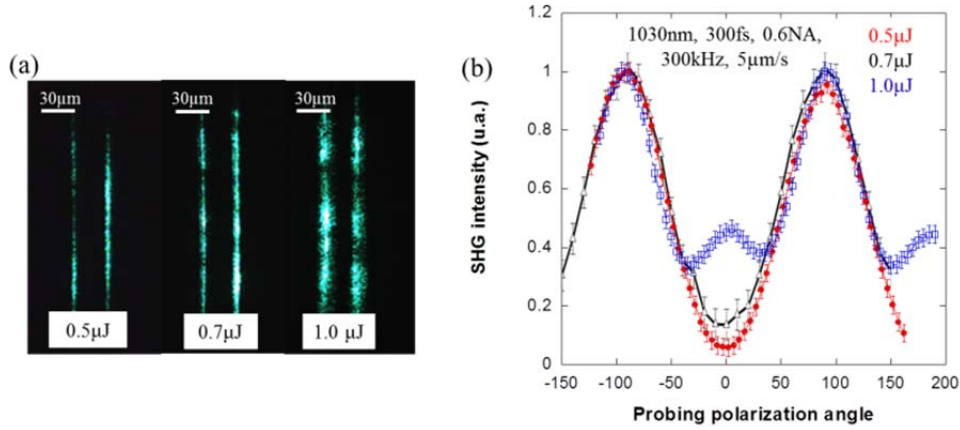


Figure 5.9 (a) Second harmonic microscopy images of 2 written lines at different pulse energies below the glass surface of  $350 \mu\text{m}$ ; (b) Polarization dependence of normalized SH intensity of the written lines at  $0.5 \mu\text{J}$  (red),  $0.7 \mu\text{J}$  (black) and  $1.0 \mu\text{J}$  (blue) as a function of probing polarization angle. The line direction is at  $0^\circ$  ( $\parallel x$ ). Other laser parameters:  $300 \text{ kHz}$ ,  $5 \mu\text{m/s}$ ,  $300 \text{ fs}$ ,  $1030 \text{ nm}$ ,  $\text{NA} = 0.6$ ,  $\vec{e} \parallel \vec{v}$ .

### Coherent or incoherent response of the nanoparticles

The origin of SH signals of nanoparticle assembly in a medium have been discussed as incoherent response recently. An assembly of metallic nanoparticles have been studied by Awada et al<sup>[4]</sup>. It is figured out that the unavoidable interface defects between centrosymmetric nanoparticles and substrate leads to symmetry breaking and

SHG. In addition, the anisotropy of the refractive index for the fundamental as well as for the harmonic wave results in the loss of phase relationship between randomly oriented nanoparticles<sup>[4]</sup>. This leads to an incoherent SH response of each nanoparticles. The global SH intensity is therefore obtained by simple addition of individual nanoparticles<sup>[5]</sup>. For an assembly of non-center symmetric nanoparticles, it is the same process. In this case, the SH intensity is independent on the spatial arrangement of the particles in the substrate.

For a good averaging, it is assumed that the probe beam diameter is much larger than the non-linear material thickness. This is actually the case here. Then if the size of non-phase matchable particles (like it is for LiNbO<sub>3</sub>) is much less than the coherent length ( $l_c$  of LiNbO<sub>3</sub> is about 10 $\mu$ m), the second harmonic intensity is proportional to the average size of particles and to the angular averaged second harmonic polarizability tensor<sup>[6]</sup>.

Otherwise, if two nanoparticles are oriented oppositely, the SH response vanishes due to the cancellation of two coherently opposite responses. From this concept, we took out a series of SH intensity measurements in terms of input beam-sizes to determine whether the orientation of polar axis of induced-crystals (especially nanocrystals) in laser lines depends on the orientation of writing.

The schematic illustration resolving orientation dependence of crystallization on orientation of writing is given in figure 5.10.  $w$  is the width of each laser trace and  $W$  is the distance between the edge of two lines. The probe beam size 1 must be not less than  $W+2w$  while the smallest size 2 is much less than  $W$ . The probe beam size 3 is intermediate between size 1 and 2 which is around  $W+w$  displayed by blue circle.

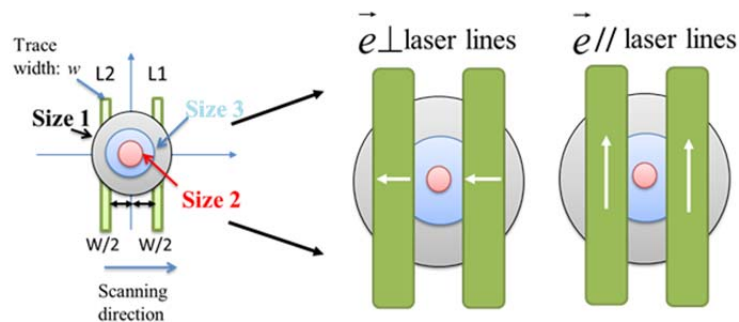


Figure 5.10 The schematic illustration of investigation of orientational writing dependence of crystallization using different sizes of probe laser beam. The written distance

between the two lines L1 and L2 is fixed at 30 μm by writing program. This pair of laser lines was written in two orientations along x-axis (Xp-x and Xn-x defined in chapter 3). The white arrows correspond to possible orientation of polar axis detected in the measurement.

Inasmuch as the coherent SH responses are obtained according to the polarization dependence curves, it makes sense to consider the exact orientation of crystallization in each line, in the opposite or the same direction. As displayed by the two enlarged laser lines in figure 5.10, the linear polarization perpendicular to laser lines was used to investigate the orientation of polar axis in y-z plane and the polarization parallel to laser lines to investigate the polar axis in x-axis. With the largest size 1 covering two lines completely, the SH responses due to the opposite orientations of polar axis of crystals should be declined or even vanished although SH responses can be obtained from each line during the passage of laser beam with size 2. The intermediate size 3 is applied to verify the assumption obtained from former cases.

The experimental and simulated studies of beam size dependence of SH intensity curves of laser lines written at 1.5 (a), 1.0 (b) and 0.6μJ (c) with two polarizations are given in figure 5.11, respectively. The simulation is carried out basing on the assumption that both of laser intensity and SH intensity of each laser line are simplified as Gaussian distribution. It is expressed as:

$$I(A, \varepsilon, x_0, \Omega, w_1, w_2, \Delta_1, \Delta_2) = A \left| \int f(x, x_0, \Omega) * [\varepsilon * f(x, \Delta_1, w_1) + f(x, \Delta_2, w_2)] dx \right| \quad (5.2.1)$$

$$\text{With } f(x, \mu, F) = \frac{2\sqrt{\ln 2}}{F\sqrt{\pi}} \cdot \exp\left(-\frac{4 \ln 2 \cdot (x - \mu)^2}{F^2}\right)$$

Here,

A: Intensity normalized coefficient in case 2 (with size 2) in terms of the beam size correction (be both related to the pulse energy and beam size);

ε: SH intensity ratio between two lines L<sub>1</sub> and L<sub>2</sub> which is regarded as a reference line in this simulation;

x<sub>0</sub>: the position of center spot of laser beam;

Ω: Full width at half maximum (FWHM) of Gaussian laser beam;

$w_n$ : width of the n-th laser trace;

$\Delta_n$ : the distance from the 0 to the center of the n-th laser trace;

The negative sign of  $\varepsilon$  involves the opposite orientation of polar axis in two lines while the positive sign indicates the crystals in two lines orientate in the same direction. The simulated values of these variants are presented in table 5.1 and 5.2. During the simulation, all of the variants could be fixed at first in comparing with the experimental result at size 2 and then be verified by the size 1 and 3, particularly the sign of  $\varepsilon$ .

In “p” case, two  $\varepsilon$  values are obtained due to the inhomogeneous distribution of crystals in two lines at 1.5  $\mu\text{J}$ . Besides, the different values of  $\Delta_1$  and  $\Delta_2$  requested for accounting the position of line center is another evidence of non-uniformed crystallization. This set of value translates that the preferential orientation of polar axis of crystals perpendicular to x-axis in each line is in the same orientation. At 1.0  $\mu\text{J}$  and 0.6  $\mu\text{J}$ , additional simulated results with negative  $\varepsilon$  have been done as shown in figures and the vanishing SH intensity for 0 position is obtained in all of these three cases: size 1-2 and size 3-2 at 1.0  $\mu\text{J}$ , size 3-2 at 0.6  $\mu\text{J}$ . From the apparent contradiction with the experimental results, we deduce that the major orientation of crystals perpendicular to the laser lines are in the same orientation between each crystallized line of a pair.

Table 5.1 The simulated variants of SH intensity curves at “p”.

	@1.5 $\mu\text{J}$			@1.0 $\mu\text{J}$					@0.6 $\mu\text{J}$			
	Size 1	Size 2	Size 3	Size 1	Size 2	Size 3	Size 1-2	Size 3-2	Size 1	Size 2	Size 3	Size 3-2
A	4.046	17	3.587	4.508	46	10.396	4.508	10.4	12.843	27.5	10.478	10.478
$\varepsilon$	1.85	1.355	1.85	1	1	1	-1	-1	1.31	1.31	1.31	-1.31
$\Omega$	30	6	8.85	40	10	14.5	40	14.5	32	10	18	18
$w_1$	8.12	8.12	8.12	3	3	3	3	3	2.5	2.5	2.5	2.5
$w_2$	5.8	5.8	5.8	3	3	3	3	3	2.5	2.5	2.5	2.5
$\Delta_1$	15	14	15	15	15	15	15	15	15	17	15	15
$\Delta_2$	-15	-19.8	-15	-15	-15	-15	-15	-15	-15	-13	-15	-15

In “s” case, additional simulation was carried out as shown by curve named size 1-2 at 1.5  $\mu\text{J}$ . It observes that a declined trend of SH near the “0” point appears in this curve due to  $\varepsilon=-0.62$ . We deduce that the preferential orientation of crystals parallel to the x axis in each line is also in the same orientation at this pulse energy, as well as the other two cases at 1.0  $\mu\text{J}$  and 0.6  $\mu\text{J}$  for lines in a pair.

Table 5.2 The simulated variants of SH intensity curves at “s”.

	@1.5 $\mu\text{J}$				@1.0 $\mu\text{J}$			@0.6 $\mu\text{J}$		
	Size 1	Size 2	Size 3	Size 1-2	Size 1	Size 2	Size 3	Size 1	Size 2	Size 3
A	4.046	22	14.42	14.42	5.94	17	10.88	6	9.8	4.033
$\varepsilon$	0.62	0.62	0.62	-0.62	0.49	0.49	0.49	1.8	1.8	1.8
$\Omega$	30	6	8.85	8.85	40	12	15	32	10	18
$w_1$	8.12	8.12	8.12	8.12	3	3	3	2.5	2.5	2.5
$w_2$	5.8	5.8	5.8	5.8	3	3	3	3	3	3
$\Delta_1$	15	15	15	15	15	15	15	15	15	15
$\Delta_2$	-15	-15	-15	-15	-15	-15	-15	-17	-17	-17

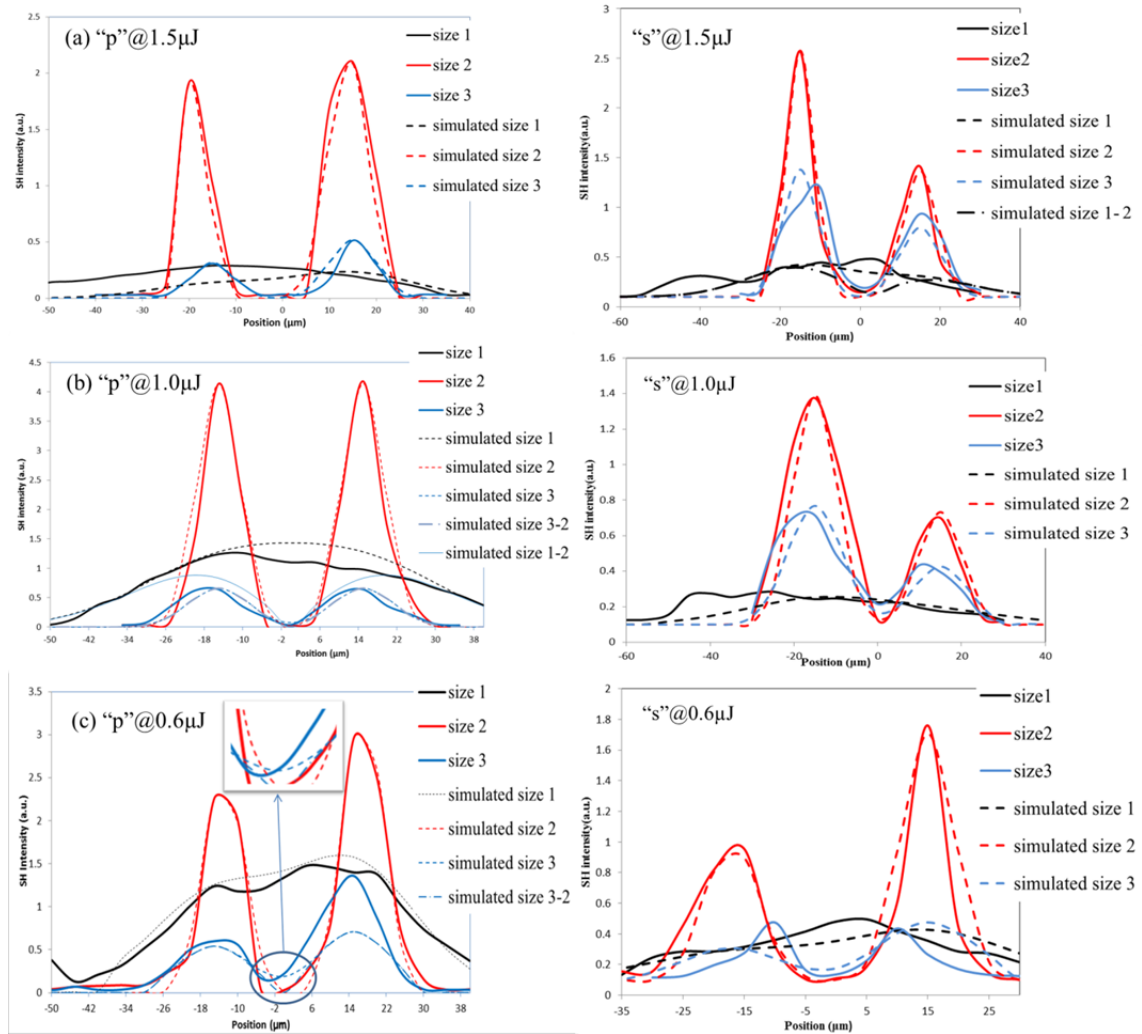


Figure 5.11 The experimental (solid line) and simulated (dash line or dotted dash line) SH intensity curves at different probe beam sizes of laser lines written at 1.5 (a), 1.0 (b) and 0.6 $\mu$ J (c). The noted “p” on the left side presents the input linear polarization along y-axis (perpendicular to laser lines) while the “s” indicates the polarization along x-axis (parallel to the laser lines).

## 5.3 Discussion

### 5.3.1 Fs laser-induced crystallization mechanism

In order to better understand the mechanism leading to the precipitation and the

orientation of the crystals in the case of fs laser irradiation, it is of importance to recall here a few words about the theory of nucleation and growth. In principle, the crystallization of glasses is dominated by two factors based on the theory of crystallization: nucleation frequency and crystal growth rate. The speed to transform the amorphous state into crystal is relevant from both the thermodynamics and the kinetics is determined by two steps: the nucleation and then the growth of the nuclei.

It is known that when such an ultra-short laser is focused in a small area in a transparent glass, the temperature ( $T$ ) at the focus center increases dramatically as a result of nonlinear absorption and subsequent non radiative relaxation. The localized heat accumulation happens if the repetition rate is high enough (typ. >200kHz in LNS glass). Consequently, the time averaged temperature at any irradiated point increases. We assumed that heating in the interaction volume is uniform (needle-shaped heat resource). Let us consider first the static case (the beam is not moving). The temperature distribution is defined in and out of the interaction volume is defined by the thermal diffusion, the heat capacity and the specific density. We have computed it. If the energy source is just from one pulse, we can see that the energy of the interaction volume is dissipated in a few microseconds i.e. the matter returns to room temperature during this short time. When pulses are separated by less this time (less than a few microsecond), the temperature at any point in or out of the interaction volume does not return to room  $T$  but reaches a steady state. If now we consider that the interaction volume (or the beam) is scanned, due to the fast response of the matter (a few microsec) compared to the scanning speed, the  $T$  of a given point  $A$  is just dependent on the distance to the center of the interaction volume schemed in figure 5.12(a). Its  $T(t)$  profiles shown in figure 5.12(b) is just obtained by dividing this distance by the scanning speed. We can see that the plateau duration is of the order of 3 microns divided by 5 micron/s, hence a fraction of sec. On the other hand, from the static computation, we have seen that the temperature is 5 times lower than in the center of interaction volume, for points distant of 1.5 microns from the interaction volume. This means a rising time of the order of 0.3 sec for the speed used here. So, finally the rising, the decreasing time is of the same order than the plateau duration. This successive step of heating-steady state-cooling behavior is similar to the classic

crystallization process. In that case, crystal shape and size are defined by the nucleation and growth rate.

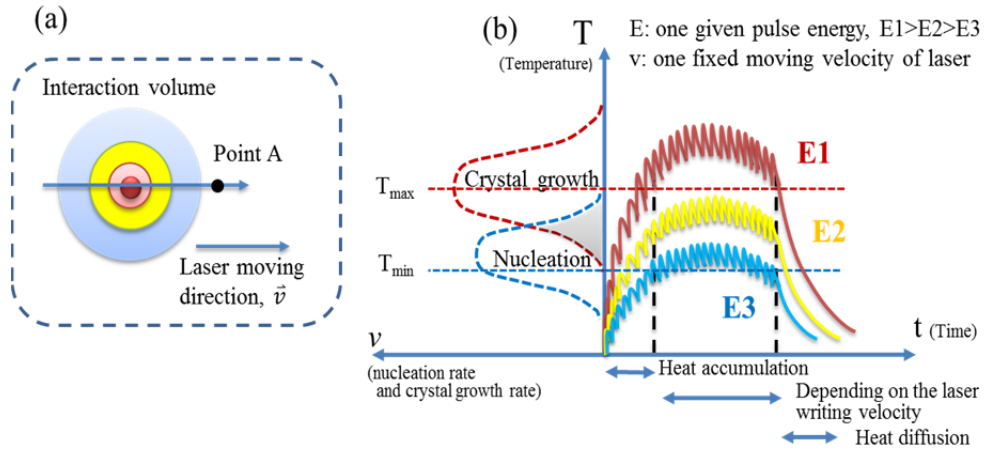


Figure 5.12 (a) the schema of interaction volume passing a given point A (b) Temperature-nucleation and crystal growth rate diagram (left) and Temperature-time profiles at point A at different pulse energies (right): E1 (red)> E2 (yellow)>E3(blue)

The diagram in terms of nucleation and crystal growth rate is given in figure 5.12(b) and the gray region between  $T_{max}$  and  $T_{min}$  is the crystallization temperature range in glass. For energy E1, the nucleation is achieved during heating process. If E1 is too high, the plateau temperature will overcome the melting temperature. So, the generated seeds are remelted during the irradiation. However, the region behind the interaction volume meets the suitable temperature for crystal growth and allows the previous crystal to grow. It is the same situation than in floating zone technique. In that case, the trace is completely filled with large crystal.

For E3, the lower plateau temperature may lie in the crystallization range but close to the  $T_{min}$ . The nucleation may occur during the plateau, so in the interaction volume. If the scanning speed is low enough, the nano-size crystals may be obtained on this occasion. At intermediate pulse energy E2, its plateau temperature situates in the crystallization range and it favors nucleation and growth in the same time. The plateau temperature mostly depends on the applied pulse energy and thermal property

of material but not on the scanning velocity, the estimated temperature in the interaction volume at  $1.5\mu\text{J}$  is about  $1000^\circ\text{C}$  <sup>[7]</sup> which is in crystal growth range<sup>[8]</sup>. One difference with E1 is that the nucleation occurs inside the interaction volume and thus many crystals can grow in the same time. A second difference is that the temperature gradient is different in E1 and E2 case, as the places of growth are different. Moreover, EBSD images at  $1.0\mu\text{J}$  and  $0.6\mu\text{J}$  in figure 5.2 exhibit isolated crystallization in the interaction volume. It is consistent with a homogenous nucleation step inside the interaction volume like for E1 and E2 cases.

Additionally, it is considered that the femtosecond laser irradiation can result in the local heating and elemental migration. If the thermal gradient occurs inside glass during irradiation, the constituent elements of the glass may spread or migrate in a specific direction. In contrast to demonstrated elemental migration of Si and Nb by fs laser irradiation<sup>[9]</sup>, no similar evidence was obtained in our laser traces written neither at high pulse energy nor at low pulse energy as shown in figures 5.4-5.7. It might be interpreted that the homogenous nucleation step at the beginning of irradiation doesn't need to drive elements in the interaction volume. Or, as demonstrated by Yonesaki and his coworkers<sup>[9]</sup>, Si element prefers to migrate to the center of the irradiated area while Nb element migrates to the outside from center. The thermo-migration induced by laser irradiation and elemental diffusion for nucleation and growth turns to be balance and no evidence elemental redistribution occurs in our case. As a consequence, with the development of nucleus till to be full of the laser trace, the Si still resides there but in nano-sized that is not detectable by EBSD or Raman spectra.

To sum up shortly, the size of crystals can be controlled directly by adjusting applied pulse energy of fs laser irradiation and crystals in nano-size can be obtained in particular by fixing the plateau temperature in the crystallization range close to  $T_{\text{min}}$ .

### **5.3.2 Oriented crystallization**

Possibilities to orient the crystallization arise from anisotropy in the free enthalpy expression on one hand, and from gradients in kinetics on the other hand<sup>[10]</sup>.

With respect to the former term, the anisotropy can be introduced by external fields, like electric or magnetic field if molecules bear an electric or magnetic dipole. Meanwhile, it is well known that nucleation and growth involve atom migrations. These diffusions are driven, not only by the gradient of free enthalpy (i.e. gradients of chemical potentials, gradient of concentrations), of electric potential, or of stress but also by gradient of mobility that can be produced by temperature or light intensity gradient. It is also worthwhile to note that non-linear absorption to intense electromagnetic field can introduce a DC like field and thus changes the moving velocity<sup>[11]</sup>. Therefore, by controlling the orientation of the fields, especially the temperature gradient orientation, we are able to control the precipitation and the crystal growth orientation.

During the writing procedure by femtosecond laser irradiation, the orientation of the growth takes place after nucleation in static mode. Heat accumulating rapidly at high repetition and then diffusing radially, the T gradient is thus oriented towards the focus center. Without other forces, the orientation for the crystallization is probably towards the center as a consequence<sup>[12]</sup>. When the laser spot is moved at high pulse energy, the crystallization might happen after the stop of the irradiation. The temperature gradient at the focus center is always towards the laser moving direction and results in well-oriented crystals. At the adjacent region, because of lower temperature than that at the focus center and other effects such as propagation of the crystallization front and the orientation of the T gradient, the crystals preferred to be randomly oriented<sup>[7]</sup>. But when the moving velocity is low enough (5 $\mu$ m/s) at low pulse energy (<1 $\mu$ J), the crystallized volume was approximately identical to the illuminated region because the low temperature, normally in the range of 580°C to 625 °C [23], was induced at the interacted zone. The distribution of T gradient at this moment can be regarded as in static case and become the principal factor on the orientation of crystallization. Therefore, it is easy to obtain the nano-sized crystals lying in the cross-section of laser tracks as shown in figure 5.2(b).

At high pulse energy (at 2.0 $\mu$ J), it is interesting to observe oriented crystallization dependency on the polarization in figure 5.2(a) and figure 5.2(b). In the case of polarization parallel to the writing direction, the induced high T gives rise

to a larger interaction volume and a high mobility. The large T gradient along the laser writing direction in region I lead to crystals orientated along writing direction<sup>[7]</sup>. Moreover, according to the investigation by Stone et al.<sup>[13]</sup>, the polar c-axis of LaBGeO<sub>5</sub> was determined by the motion of laser irradiation during 2D laser patterning procedure. And single-crystal architecture on Sm<sub>0.5</sub>La<sub>0.5</sub>BGeO<sub>5</sub> glass has been achieved by CW laser irradiation in u-shape. However, the polarization dependence and orientation writing dependence of SHG intensity exhibited in figure 5.9 and 5.11 present a contradicted proof that the polar axis of functional crystals in each line orientate in the same direction. Indeed, although the EBSD mapping in figure 5.2 pointed out that at high pulse energy, such as at 1.5 μJ, the preferential orientation of crystals in line is along x-axis, the randomly oriented crystals appeared at the head and at the tail in laser track<sup>[7]</sup>. This leads to the observation of SH responses when polarization is perpendicular to the laser lines written at 1.5 μJ. As the same reason, at low pulse energy as at 1.0μJ and 0.6 μJ, some pieces of nano-crystals coded in red color displayed in EBSD images result in the SH signals in “s” case. It assumes that the primarily inscription of the first line might dominate the whole process of laser-induced crystallization by fs laser irradiation.

Besides, randomly oriented nano-size crystallization was observed in the figure 5.2(b) just by flipping the polarization perpendicular to the writing direction. We have also to precise that the lines were written horizontally.

Effect of laser polarization is not an obvious problem. It is worth noticing that laser polarization exists only during a very short period (here 300fs), then there is a quite period of 3 μs before the next pulse. Looking at the literature, the closest experiment describing polarization effect on glass transformation is Kazansky et al<sup>[14]</sup>. The authors invoke a combination of polarization and Pulse Front Tilt (usual for ultra short laser) in the expression of a direct non-linear heat current. In this model, the current amplitude is maximum for laser polarization parallel to plasma density gradient induced by PFT. When active, this current might heat more one side of the interaction volume than the other one. So, under movement, heat accumulates more in one orientation than in the other one. When laser polarization is perpendicular to writing, no effect is expected. It is important to note that this assumes that PFT lies in

the horizontal plane. The laser polarization direction dependence appears consistent with this work but there is doubt that this asymmetric heat current during a such short period of time can induced anisotropy large enough in front of T and thermochemical gradient to influence the nano-crystallization that is achieved at least after fraction of heating.

Rather, we would suggest that a memory process is necessary. Starting from Kazansky et al. proposal that PFT acting in ponderomotive force, creating a plasma density gradient, we underline that a space charge is created<sup>[11]</sup>) that is stored in the glass and remains after the pulse vanished at least until the next pulse. The high temperature (580°C)<sup>[8]</sup> is not high enough for erasing the space charge in a few  $\mu\text{s}$ . Then, as in Kazansky's expression of the heat current, the space charge is asymmetric and its direction is defined by combination of laser polarization and PFT. Now, if we consider that seeds of ferroelectric crystal carry a permanent dipole, the seed experiences a torque where the electric field of the space charge is. This torque is zero when both vectors are parallel i.e. when the polar axis is in the direction of the positive combination of laser polarization and PFT. It is possible to show that there is no effect at 90° of the efficient case, like for the above observation. This proposal is interesting because by mastering the space charge orientation, it is possible to open the door to orientation control of the seed at will. But, before, we can also use the seeds for mapping this space charge distribution pertinently.

## 5.4 Conclusion

Direct 3D precipitation of optical crystals in traditional transparent glass by ultra-fast laser irradiation has been realized in this thesis. The size and orientation of crystals are efficiently affected by varying either pulse energy or the applied polarization direction which are examined by EBSD mapping method. When linear polarization was parallel to the motion direction, oriented nonlinear crystals at nano-scale preferred to precipitate at low pulse energy. When linear polarization is in perpendicular case for laser irradiation, the crystals in nano-size can be obtained as well but with randomly orientation.

Evident thermo-migration of constituent elements has not been observed by EDX, WDS or nuclear microprobe methods. Si elements are considered to reside and homogeneously distribute in the laser tracks in nano-sized crystals that is undetectable by presented methods.

SH intensity depending on both polarization and on detect beam-size has achieved. The preferential orientation of crystals induced at high pulse energy is along laser motion direction and at low pulse energy is perpendicular to the laser motion direction. This observation is consistent with EBSD results. Moreover, the orientation of polar axis of functional crystals in each line has examined by the beam-size dependence measurement and it deduced that they preferred orientating in the same direction in the same direction.

The mechanism of oriented crystallization has been discussed and its demonstration of fs laser-induced oriented  $\text{LiNbO}_3$ -like crystals in glass enables a versatile route for designing desired crystals in transparent materials. The nonlinear optical property indicates that various optical and electro-optical devices can be expected, e.g. doubling or routing waveguides, by this technology. Furthermore, the controllable crystallization in other functional material, such as fresnoite-type glass, is undergoing continuously studied to broaden the availability of this promising technology in laser-material processing.

## Reference

- [1]. Fan, C. X. Contribution to nano or micro crystallization induction in silica-based glasses by femtosecond laser irradiation. Université de Paris Sud 11 & East China University of Science and Technology 2012.
- [2]. Schaufele, R. F., Weber, M. J. , Raman scattering by lithium niobate. *Physics Review* **1966**, *152*, 705-708.
- [3]. Yu, B.,Chen, B.,Yang, X. Y., *et al.*, Study of crystal formation in borate, niobate, and titanate glasses irradiated by femtosecond laser pulses. *J Opt Soc Am B* **2004**, *21* (1), 83-87.
- [4]. Awada, C.,Jonin, C.,Kessi, F., *et al.*, Polarized second harmonic response of square, hexagonal and random arrays of gold metallic nanocylinders. *Opt Mater* **2011**, *33* (9), 1440-1444.
- [5]. Awada, C.,Kessi, F.,Jonin, C., *et al.*, On- and off-axis second harmonic generation from an array of gold metallic nanocylinders. *J Appl Phys* **2011**, *110* (2).
- [6]. Kurtz, S. K., Perry, T. T. , A powder technique for the evaluation of nonlinear optical materials. *J Appl Phys* **1968**, *39*, 3798-3813.
- [7]. Fan, C. X.,Poumellec, B.,Lancry, M., *et al.*, Three-dimensional photoprecipitation of oriented LiNbO<sub>3</sub>-like crystals in silica-based glass with femtosecond laser irradiation. *Opt Lett* **2012**, *37* (14), 2955-2957.
- [8]. Vigouroux, H.,Fargin, E.,Fargues, A., *et al.*, Crystallization and Second Harmonic Generation of Lithium Niobium Silicate Glass Ceramics. *J Am Ceram Soc* **2011**, *94* (7), 2080-2086.
- [9]. Yonesaki, Y.,Miura, K.,Araki, R., *et al.*, Space-selective precipitation of non-linear optical crystals inside silicate glasses using near-infrared femtosecond laser. *J Non-Cryst Solids* **2005**, *351* (10-11), 885-892.
- [10]. Scheel, H. J., Capper, P. , *Crystal Growth Technology: from fundamentals and simulation to large-scale production*. Wiley-VCH: 2008.
- [11]. Gutzow, I.,Dobrev, A.,Russel, C., *et al.*, Kinetics of vitrification under hydrostatic pressure and under tangential stress. *J Non-Cryst Solids* **1997**, *215* (2-3), 313-319.
- [12]. Yonesaki, Y.,Miura, K.,Araki, R., *et al.*, Space-selective precipitation of non-linear optical crystals inside silicate glasses using near-infrared femtosecond laser. *J Non-Cryst Solids* **2005**, *351* (10–11), 885-892.
- [13]. Stone, A.,Sakakura, M.,Shimotsuma, Y., *et al.*, Directionally controlled 3D ferroelectric single crystal growth in LaBGeO<sub>5</sub> glass by femtosecond laser irradiation. *Opt Express* **2009**, *17* (25), 23284-23289.
- [14]. Yang, W. J.,Kazansky, P. G.,Svirko, Y. P., Non-reciprocal ultrafast laser writing. *Nat Photonics* **2008**, *2* (2), 99-104.

## **Chapter 6 Photo-Induced oriented crystallization in STS glass by fs laser**

In this chapter, the oriented crystallization in SrO-TiO<sub>2</sub>-SiO<sub>2</sub> glass will be studied systemically by fs laser irradiation based on the investigation of chapter 4. The glass with stoichiometric and non-stoichiometric compositions regarding to the fresnoite-phase Sr<sub>2</sub>TiSi<sub>2</sub>O<sub>8</sub> have been prepared by traditional melt-quenching method and named as STS-1 and STS-2 glass in this thesis, respectively. SEM images has been taken to investigate the morphology of laser track cross-section and EBSD method has been used to characterize the size and orientation of polar axis of induced crystals as well. SHG intensity measurement was applied again to check the oriented crystallization in macroscopic aspect and the nonlinear optical properties of laser lines.

### **6.1 Photo-induced oriented crystallization in the glass 40SrO-20TiO<sub>2</sub>-40SiO<sub>2</sub> (STS1)**

#### **6.1.1 The crystallization induced by fs laser**

##### **Laser writing process**

The laser writing process was realized using femtosecond laser femtosecond laser system (Satsuma, Amplitude Systèmes Ltd.) at 1030 nm and delivering pulses of 300 fs. The laser beam motion ( $v$ ), pulse energy ( $E$ ) and polarization ( $e$ ) were controlled by a 5D stage-control software (Gol3D from GBCS<sup>®</sup>). To avoid anisotropic heat dissipation due to the presence of the glass sample surface, the beam was focused virtually at 150  $\mu$ m in depth using a microscopic objective (NA=0.6). All of the laser lines were written with first static irradiation for 30 seconds and then written in x-axis continuously at different scanning velocities with polarization parallel to the motion direction (Xp-x) .

A series of static irradiations (pulse energy vs repetition rate) has been completed to define the crystallization threshold in 40SrO-20TiO<sub>2</sub>-40SiO<sub>2</sub> (STS-1) glass at first.

We found that when the repetition rate is less than 200 kHz, no crystallization occurs during the irradiation. At 200 kHz, the crystallization is observed when the pulse energy overcomes 1.0 $\mu$ J. If the glass is irradiated at 300 kHz, crystallization happens with the pulse energy at 0.4-1.0  $\mu$ J. With increasing the repetition rate up to 400 kHz, crystallization can be achieved with the applied pulse energy ranging from 0.3 to 0.7 $\mu$ J, the crystallization is observed. And then, no crystals are obtained any more with the repetition rate at 500 kHz.

Systematic experiments were carried out to investigate the influence of laser parameters on crystallization and its orientation via modifying the pulse energy, writing velocity and laser polarization.

### **Optical properties-Birefringence**

After laser irradiation, we measured the retardance proportional to birefringence originating from photo-induced crystallization and a part of induced stress as shown in table 6.1. Notice that no crystallization was observed for a writing velocity at 40 $\mu$ m/s and for low pulse energies at 20  $\mu$ m/s (for instance, at 0.5  $\mu$ J, 0.7 $\mu$ J and 0.9  $\mu$ J).

Table 6.1 gives the measured retardance of laser tracks written at different pulse energies at different motion velocities in x-y plan. The retardance value in *Italic* in the table means that no crystals are observed in laser trace at this configuration. In general, the retardance of laser lines written at one pulse energy is declined when increasing the laser motion velocity. At high writing velocity, i.e. at 40  $\mu$ m/s, the thermal-heating effect and its aftereffect induced-stress field caused by fs laser irradiation might probably give rise to the birefringence which is increasing with inputting high pulse energies<sup>[1-2]</sup>. Moreover, in the case of crystallization occurring at low writing velocity ranging from 3 $\mu$ m/s to 10  $\mu$ m/s, the retardance of laser lines is increased in general with pulse energy being higher at each velocity. This might due to the both contributions from the thermal-heating effect and appearance of crystallization in laser lines. Besides, at 20 $\mu$ m/s, no obvious trend of retardance change is observed and this might be caused by the transition state around crystallization process when varying pulse energy from 0.5 to 1.7  $\mu$ J.

Table 6.1 The measured retardance (nm) of laser tracks in x-y plan by Senarmon method. Other laser parameters: 300 kHz, 300 fs, 1030 nm, NA = 0.6, Xp-x writing configuration.

	3 $\mu\text{m/s}$	5 $\mu\text{m/s}$	10 $\mu\text{m/s}$	20 $\mu\text{m/s}$	40 $\mu\text{m/s}$
0.5 $\mu\text{J}$	83	98	61	46	49
0.7 $\mu\text{J}$	57	47	34	31	26
0.9 $\mu\text{J}$	40	37	34	32	43
1.1 $\mu\text{J}$	74	67	57	51	51
1.3 $\mu\text{J}$	55	55	70	49	64
1.5 $\mu\text{J}$	110	80	136	49	67
1.7 $\mu\text{J}$	57	122	78	211	170

### Micro-Raman scattering spectra

The formation of crystals induced by femtosecond laser in STS-1glass was examined by micro-Raman scattering spectra in laser line as shown in figure 6.1.

The black curve presents the Raman-spectra of amorphous glass substrate. The broad bands are observed around 1050  $\text{cm}^{-1}$ , 860  $\text{cm}^{-1}$  and 320  $\text{cm}^{-1}$ . Then the laser beam is focused on irradiated zone. Without taking polarizers, the red curve can be obtained with 3 sharp peaks at 610  $\text{cm}^{-1}$ , 675  $\text{cm}^{-1}$  and 850  $\text{cm}^{-1}$ , respectively. The band observed at 610  $\text{cm}^{-1}$  may be assigned to the bending modes of  $\text{Si}_2\text{O}_7$  groups in the laser trace. The 675  $\text{cm}^{-1}$  band, which exhibits smaller intensity, is assigned to the bridge symmetric stretch  $\nu_s$  ( $\text{SiOSi}$ ) (A1 class) of the two pyro groups. The presence of strongest peak at the 850  $\text{cm}^{-1}$  suggests the assignment to the A1-type  $\nu_s$  ( $\text{SiO}_3$ ) vibration mixing with the stretching vibration with the short Ti-O bonds, which is also A1 type. All these results point out one kind of the fresnoite-type crystal,  $\text{Sr}_2\text{TiSi}_2\text{O}_8$ , which has precipitated by laser irradiation in this glass<sup>[3]</sup>.

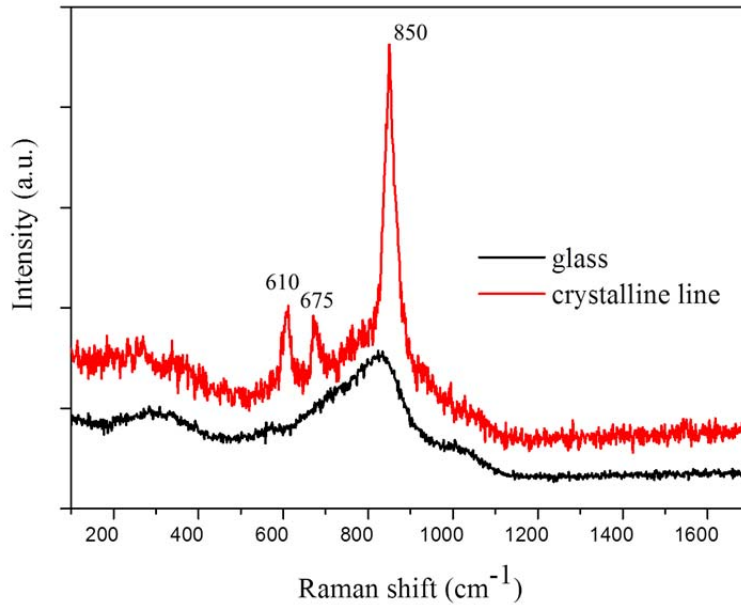


Figure 6.1 Micro-Raman scattering spectra at room temperature for glass substrate and irradiated crystalline in STS-1 glass. Laser parameter: 300 kHz, 0.7  $\mu\text{J}$ , 5  $\mu\text{m/s}$ , 300fs, 1030nm, NA=0.6,  $\vec{e} \parallel \vec{v}$

#### EDX analysis in the interacted zone

The morphology of elliptical shaped cross-section of laser line along the propagation direction is shown by SEM after cleaving and etching by 2% HF acid for 30 s shown in figure 6.2. Three distinguished region is observed: the smooth glass substrate, thermal an affected region around laser trace and the rough crystallized region at the center of laser track. The length and width of laser trace is about 20  $\mu\text{m}$  and 5.5  $\mu\text{m}$ , respectively. Besides, a transverse fracture is revealed by chemical etching as shown in the SEM images which might be resulted both from the change of specific volume with the appearance of crystallization and from the induced-stress which overcomes its rupture limit to form a fracture perpendicular to the contraction direction<sup>[4-6]</sup>.

The elemental redistribution is discovered by EDX line scanning spectra across the laser irradiated zone as shown in figure 6.2(b) and (c). It is seen that the element Si prefers to be concentrated at the center of irradiated region while Sr tends to

migrate towards to the surrounding of the focal point. No apparent evidence for the composition variation for the element Ti. This result is consistent with that of the observation in ref (formation mechanism and applications of laser induced elemental distribution in glasses).

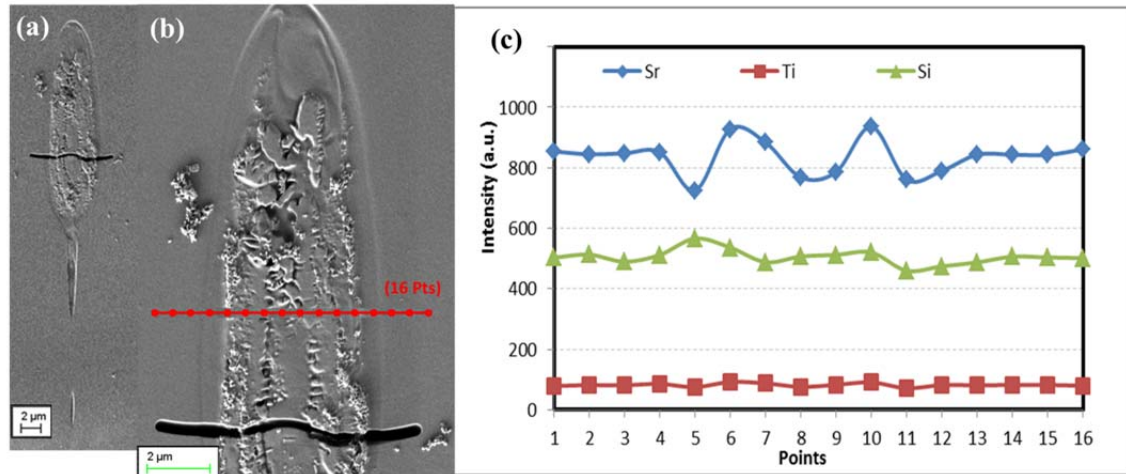


Figure 6.2 SEM image of entire morphology of cross-section of laser trace written at 0.7 μJ in STS-1 glass after cleaving and etching with 2% HF acid for 30s and magnified part at the head of cross-section (b) and EDX line scanning spectra (c). The fs laser propagation is along z-axis, from the top to bottom of the photographs. Laser parameter: 300 kHz, 5 μm/s, 300fs, 150 μm, 1030nm, NA=0.6,  $\vec{e} \parallel \vec{v}$

### The influence of pulse energy and writing velocity

The influence of pulse energy and writing velocity on crystallization has been investigated via undertaking SEM images of cross-section of laser lines as shown in figure 6.3. As the same as that in LNS glass, three regions, crystallized region at the center, thermal affected region at surrounding and exterior glass matrix, have been clearly observed. Besides, it seems that no pronounced change concerning to the size of the interaction volume by varying writing velocity when fixing the pulse energy. But, it affects much on the distribution and crystalline phase of crystals during the irradiation. As shown in figure 6.3 (a), lens-shaped cross-section is formed and the raised crystals appears at the head. A non-diverging trace beyond focal volume appears due to a balance between the nonlinear increase of refractive index and the defocusing effect of electron plasma<sup>[7-8]</sup>. The crystallized part is examined by EBSD

method and the diffraction patterns show that the precipitated crystalline phase is  $\text{SrTiO}_3$ . When writing velocity is higher, more crystals are obtained around the raised crystals and the second crystalline phase in Fresnoite-type  $\text{Sr}_2\text{TiSi}_2\text{O}_8$  crystal comes about with  $5\mu\text{m/s}$ . If increasing the writing velocity to  $20\mu\text{m/s}$ , dendritic shaped crystals  $\text{Sr}_2\text{TiSi}_2\text{O}_8$  are acquired and the crystals turn to fill the center of interaction volume as displayed in figure 6.3 (c). In the other hand, if writing laser lines at low pulse energy, for instance, at  $0.7\mu\text{J}$ , crystallization prefers to take place at the center of interaction volume in figures 6.3 (g-i) and the sole crystalline phase  $\text{Sr}_2\text{TiSi}_2\text{O}_8$  is obtained. More descriptions in detail are presented in table 6.2.

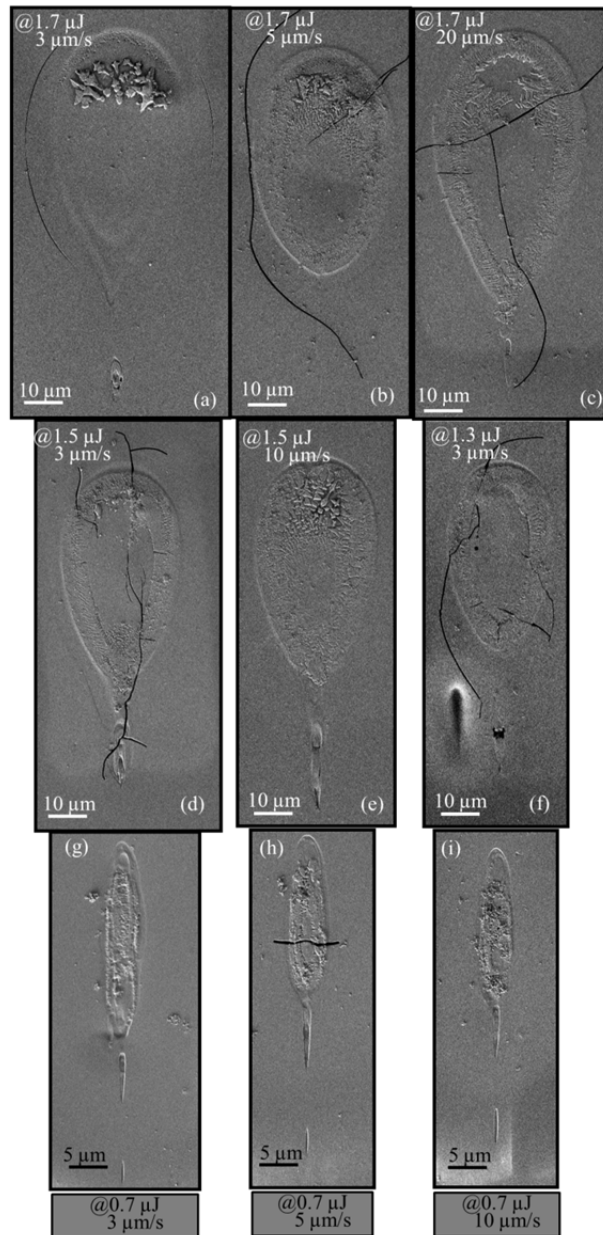


Figure 6.3 SEM images of cross-section of the written lines irradiated 150  $\mu\text{m}$  below the glass surface after having cleaved, polished and etched with 2%HF for 30s. Laser parameters:(a) 1.7  $\mu\text{J}$ , 3  $\mu\text{m/s}$ ;(b) 1.7  $\mu\text{J}$ , 5  $\mu\text{m/s}$ ;(c) 1.7  $\mu\text{J}$ , 20  $\mu\text{m/s}$ ;(d) 1.5  $\mu\text{J}$ , 3  $\mu\text{m/s}$ ;(e) 1.5  $\mu\text{J}$ , 10  $\mu\text{m/s}$ ;(f) 1.3  $\mu\text{J}$ , 3  $\mu\text{m/s}$ ;(g) 0.7  $\mu\text{J}$ , 3  $\mu\text{m/s}$ ;(h) 0.7  $\mu\text{J}$ , 5  $\mu\text{m/s}$ ;(i) 0.7  $\mu\text{J}$ , 10  $\mu\text{m/s}$ ;  
other parameters: 300 kHz, 300 fs, 1030 nm, NA = 0.6,  $\vec{e} \parallel \vec{v}$ .

Table 6.2 The detailed information concerning to the size of interaction volume, location and crystalline phase of induced crystals in laser tracks shown in figure 6.3.

( $\mu\text{J}$ )		3 $\mu\text{m/s}$	5 $\mu\text{m/s}$	10 $\mu\text{m/s}$	20 $\mu\text{m/s}$
	Width:	~30 $\mu\text{m}$	~35 $\mu\text{m}$	-	~38 $\mu\text{m}$
	Length:	~65 $\mu\text{m}$	~60 $\mu\text{m}$	-	~70 $\mu\text{m}$
1.7	Crystalline phase:	100% SrTiO <sub>3</sub> , in the head	50% SrTiO <sub>3</sub> +50% Sr <sub>2</sub> TiSi <sub>2</sub> O <sub>8</sub> , in the head	-	100% Sr <sub>2</sub> TiSi <sub>2</sub> O <sub>8</sub> , shell
	Width:	~30 $\mu\text{m}$	-	~32 $\mu\text{m}$	-
	Length:	~55 $\mu\text{m}$	-	~53 $\mu\text{m}$	-
1.5	Crystalline phase:	5% SrTiO <sub>3</sub> in the head, 95% Sr <sub>2</sub> TiSi <sub>2</sub> O <sub>8</sub> shell	-	5% SrTiO <sub>3</sub> in the head, 95% Sr <sub>2</sub> TiSi <sub>2</sub> O <sub>8</sub> , In the head+ shell	-
	Width:	~27 $\mu\text{m}$	-	-	-
	Length:	~47 $\mu\text{m}$	-	-	-
1.3	Crystalline phase:	5% SrTiO <sub>3</sub> in the head, 95% Sr <sub>2</sub> TiSi <sub>2</sub> O <sub>8</sub> , shell	-	-	-
	Width:	~5 $\mu\text{m}$	~5 $\mu\text{m}$	~5 $\mu\text{m}$	-
	Length:	~23 $\mu\text{m}$	~20 $\mu\text{m}$	~18 $\mu\text{m}$	-
0.7	Crystalline phase:	100% Sr <sub>2</sub> TiSi <sub>2</sub> O <sub>8</sub> , center	100% Sr <sub>2</sub> TiSi <sub>2</sub> O <sub>8</sub> , center	100% Sr <sub>2</sub> TiSi <sub>2</sub> O <sub>8</sub> , center	-

### 6.1.2 The orientation of induced crystallization by fs laser irradiation

The cubic lattice of SrTiO<sub>3</sub> crystal possesses inversion symmetric center with  $a=b=c=3.905\text{\AA}^{[9]}$ . In this case, the zero value of  $\chi^{(2)}$  does not permit it to be used as a double frequency convertor but Sr<sub>2</sub>TiSi<sub>2</sub>O<sub>8</sub>, being P4bm system and TiO<sub>5</sub> square pyramidal structure and owning large permanent polarizability along c-axis, is favorable for the application of nonlinear optical materials<sup>[10]</sup>. Therefore, it is much more interesting to investigate the orientation of polar axis of this last functional

crystal. EBSD images coding orientation of polar axis (c-axis) of precipitated  $\text{Sr}_2\text{TiSi}_2\text{O}_8$  crystals along x-axis in laser traces written with different parameters are given in figure 6.4. The polarization direction during writing procedure is parallel to the laser motion direction.

When the pulse energy is  $1.7\mu\text{J}$ , the precipitated pure  $\text{Sr}_2\text{TiSi}_2\text{O}_8$  crystalline phase distributes circumferentially and parts of crystals in dendritic form is found in the head of laser track. No preferential orientation of crystals c-axis (001) in laser track is exhibited in figure 6.4 (a). Contrarily to this, c-axis of crystals prefers to orient along the writing direction with a tilted angle has been observed in laser tracks with other pulse energies (figure 6.4 (b-g)). Furthermore, when pulse energy is at  $0.7\mu\text{J}$ , crystals in micro scale are precipitated at the center of laser tracks with low writing velocity. If laser moves faster, crystals turn to be fragmentally distributed with maintain their preferential orientation.

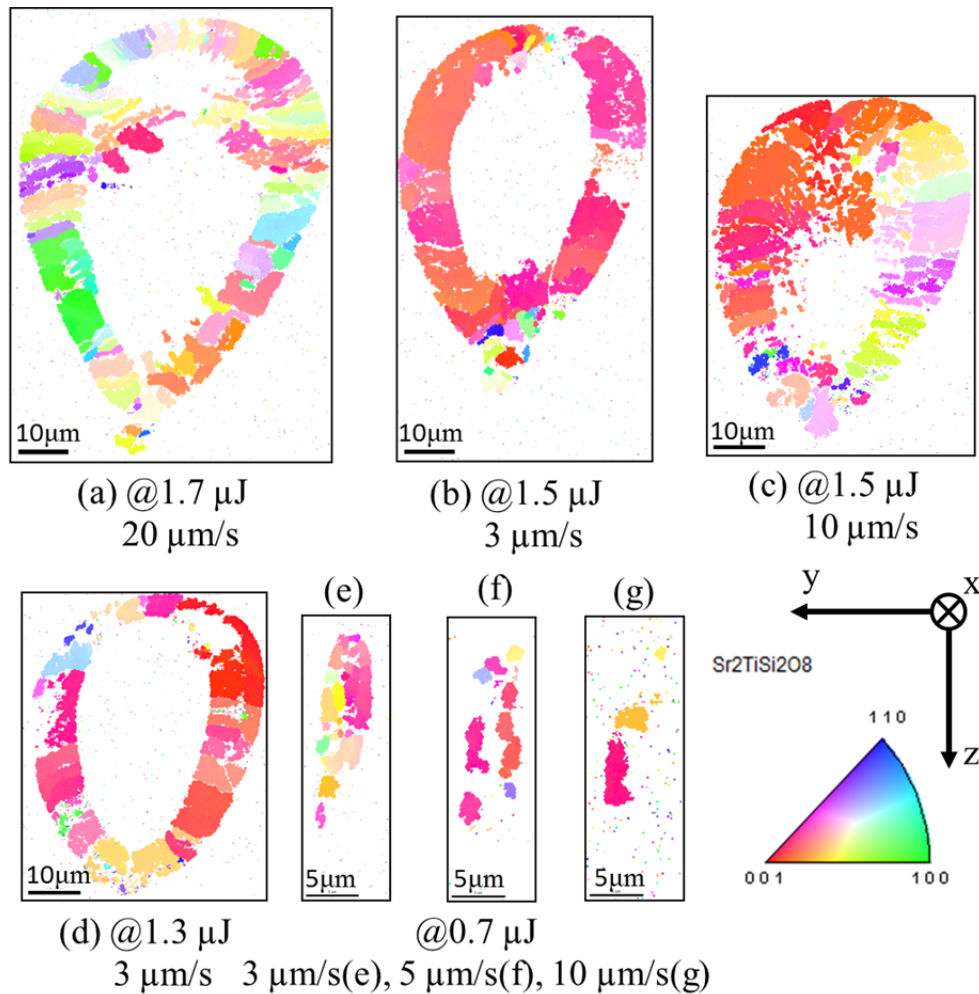


Figure 6.4 EBSD images coding the orientation of  $\text{Sr}_2\text{TiSi}_2\text{O}_8$  crystals along x-axis in the cross-section of the written lines irradiated 150  $\mu\text{m}$  below the glass surface after having cleaved, polished and etched with 2% HF for 30s. Laser parameters:(a) 1.7  $\mu\text{J}$ , 20  $\mu\text{m/s}$ ; (b) 1.5  $\mu\text{J}$ , 3  $\mu\text{m/s}$ ; (c) 1.5  $\mu\text{J}$ , 10  $\mu\text{m/s}$ ; (d) 1.3  $\mu\text{J}$ , 3  $\mu\text{m/s}$ ; (e) 0.7  $\mu\text{J}$ , 3  $\mu\text{m/s}$ ; (f) 0.7  $\mu\text{J}$ , 5  $\mu\text{m/s}$ ; (g) 0.7  $\mu\text{J}$ , 10  $\mu\text{m/s}$ ; other parameters: 300 kHz, 300 fs, 1030 nm, NA = 0.6,  $\vec{e} \parallel \vec{v}$

It seems that nearly all of the crystals induced with laser parameters being 1.5  $\mu\text{J}$  and 3  $\mu\text{m/s}$  prefer to orient along the writing direction x-axis. To investigate further the orientation of crystals in laser tracks, both EBSD mapping coding the orientation of c-axis of  $\text{Sr}_2\text{TiSi}_2\text{O}_8$  crystals along x-axis and orientation distribution functions (ODFs) in the cross-section of this written line have been given in figure 6.5 (a) and (b), respectively. The preferential orientation, or so-called texture, with 2 high

intensities color coded by red-orange can be found in  $\phi_2=0$  section (in Euler space<sup>[11]</sup>) as displayed in figure 6.5 (b). The black wire frame illustrates the orientation of a unit cell of crystal occurring at the highest intensity region which is almost perfectly along the x-axis.

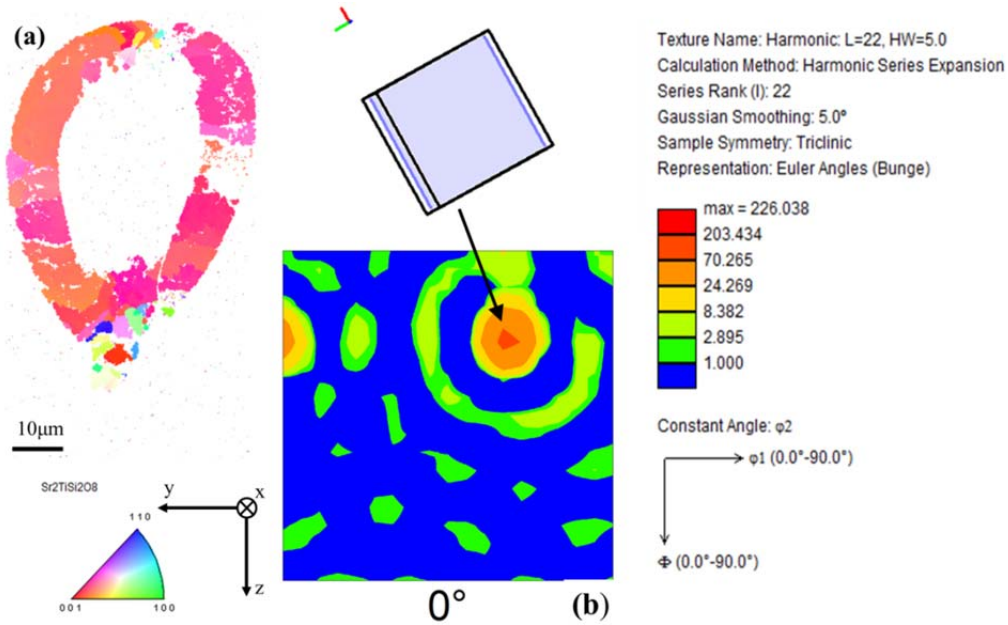


Figure 6.5 EBSD images (a) coding the orientation of Sr<sub>2</sub>TiSi<sub>2</sub>O<sub>8</sub> crystals along x-axis and orientation distribution functions (ODFs) (b) in the cross-section of the written lines irradiated 150  $\mu\text{m}$  below the glass surface after having cleaved, polished and etched with 2% HF for 30s. Laser parameters: 1.5  $\mu\text{J}$ , 3  $\mu\text{m/s}$ , 300 kHz, 300 fs, 1030 nm, NA = 0.6,  $\vec{e} \parallel \vec{v}$

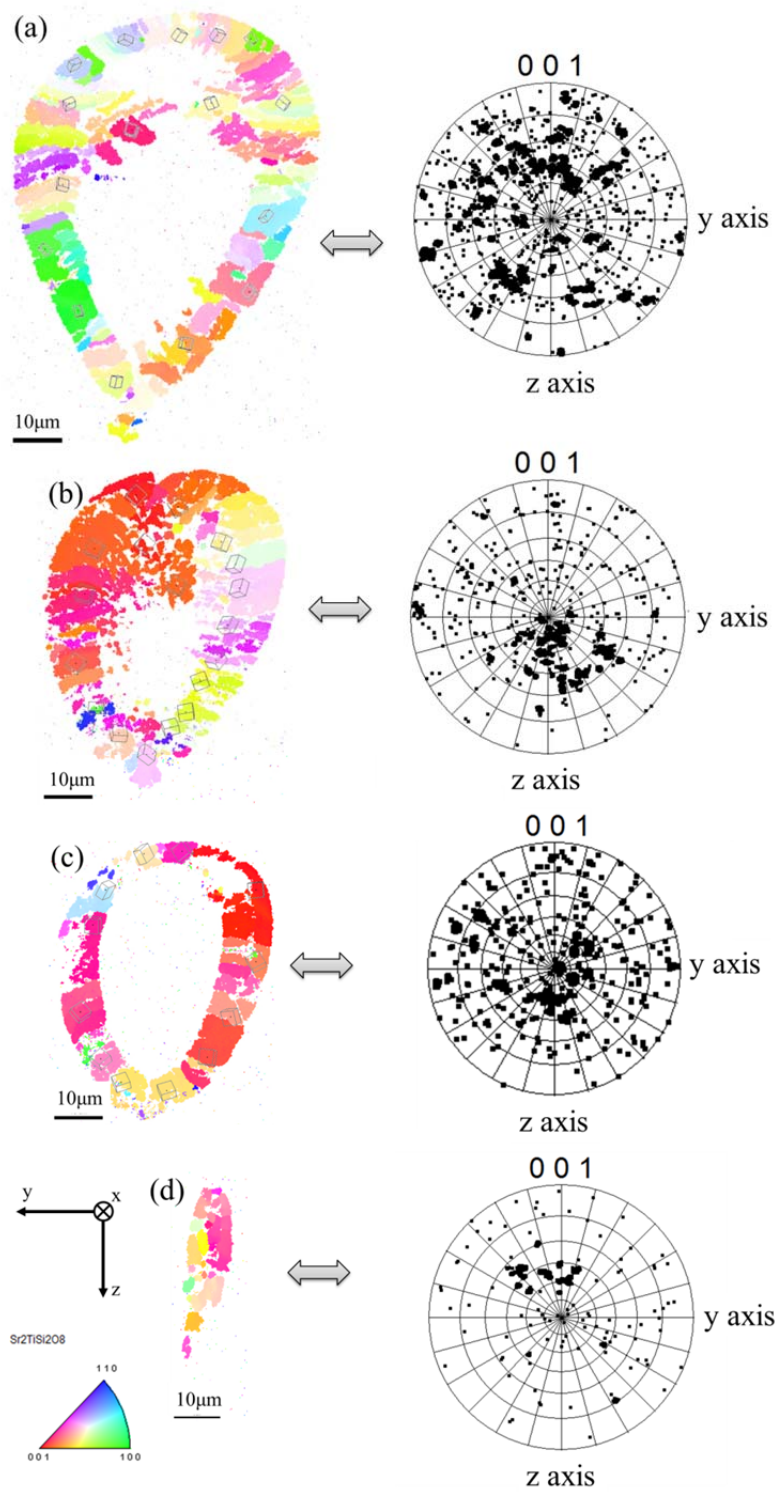


Figure 6.6 EBSD images coding the orientation of  $\text{Sr}_2\text{TiSi}_2\text{O}_8$  crystals along x-axis of the sample (a) and angular distribution of c axis (001 pole figures) obtained in the cross-section of

the same written lines irradiated 150  $\mu\text{m}$  below the glass surface after having cleaved, polished and etched with 2% HF for 30s. Laser parameters:(a) 1.7  $\mu\text{J}$ , 20  $\mu\text{m/s}$ ; (b) 1.5  $\mu\text{J}$ , 10  $\mu\text{m/s}$ ; (c)

1.3  $\mu\text{J}$ , 3  $\mu\text{m/s}$ ; (d) 0.7  $\mu\text{J}$ , 3  $\mu\text{m/s}$ ; other parameters: 300 kHz, 300 fs, 1030 nm, NA = 0.6,

$$\vec{e} \parallel \vec{v}.$$

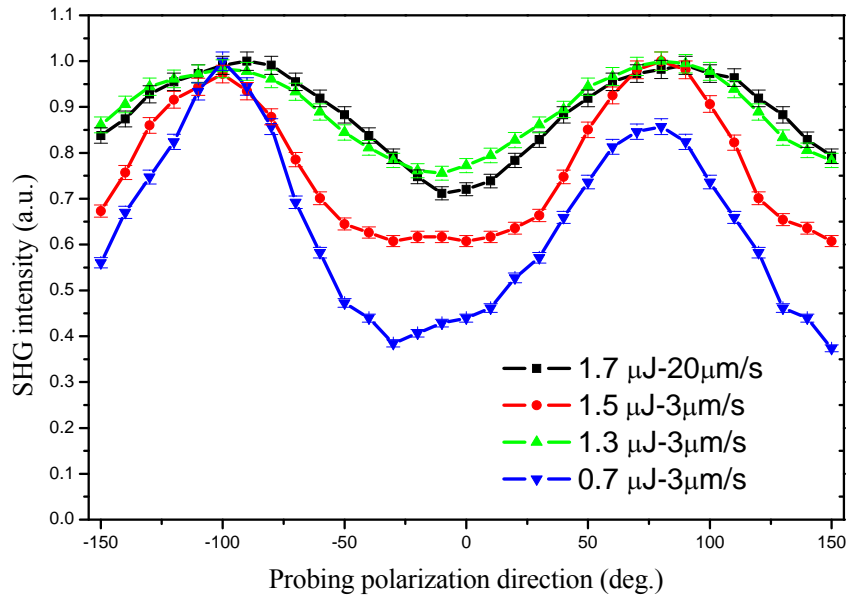


Figure 6.7 Polarization dependence in the plane  $x,y$  of normalized SH intensity curves of the written lines at 0.7 $\mu\text{J}$ -3 $\mu\text{m/s}$  (blue-inversed triangle), 1.3 $\mu\text{J}$ -3 $\mu\text{m/s}$  (green-triangle), 1.5 $\mu\text{J}$ -3 $\mu\text{m/s}$   $\mu\text{J}$  (red-circle) and 1.7 $\mu\text{J}$ -20 $\mu\text{m/s}$  (black-rectangle) as a function of probing polarization angle, the line direction is at  $\pm 90^\circ$  ( $\parallel$   $x$ -axis). Other laser parameters: 300 kHz, 5  $\mu\text{m/s}$ , 300 fs, 1030 nm, NA = 0.6,  $\vec{e} \parallel \vec{v}$ .

Regarding to the orientation of crystals in cross-section in other laser lines, comparison of the degree of preferred orientation have been achieved in  $\langle 001 \rangle$  pole figures as shown in figure 6.6. Immediately noticeable is the relatively large dispersion of black dots in figure 6.6 (a), implying a weak preferred orientation. In figure 6.6 (b,c,d), it is found that the  $c$ -axis of crystals prefers to lie around the center of the pole figure i.e. parallel to the writing direction. Beside the main texture in 6(b), a part of crystals is disordered (right hand side of the interaction volume). In figure

6.6 (d), the preferential orientation is indicated by  $\langle 001 \rangle$  pole figure which shows that c axis is tilted by  $30^\circ$  from the writing direction.

The quality of the crystal orientation in lines was characterized by normalized SH intensity measurement as a function of probing polarization azimuth in figure 6.7. The obtained maximum intensity of curves is around  $\pm 90^\circ$  which implies that the oriented nonlinear crystals along laser writing direction are precipitated in laser lines. Moreover, the SH intensity at  $0^\circ$  at  $0.7 \mu\text{J}-3\mu\text{m/s}$  is much closer to 0 than the other cases. It elucidates that using ultra-short irradiation with low pulse energy can induce highly oriented c-axis of crystals towards the writing direction in lines such as in case of  $0.7 \mu\text{J}-3\mu\text{m/s}$ . Although it is possible to precipitate crystals along the writing direction at high pulse energy (higher than  $1.3\mu\text{J}$ ), randomly oriented crystals, or tilted crystals towards the writing direction are usually accompanied during crystallization. This results in larger SHG intensity at  $0^\circ$  in figure 6.7 and consistent with the EBSD images in figure 6.4 and figure 6.6. Furthermore, it is surprising to find that the envelope of SHG intensity curve obtained at  $1.7\mu\text{J}-20\mu\text{m/s}$  is quite similar to that at  $1.3\mu\text{J}-3\mu\text{m/s}$ .

## 6.2 Photo-induced asymmetric oriented crystallization in the glass 33.3SrO-16.7TiO<sub>2</sub>-50SiO<sub>2</sub> (STS-2)

Indeed, since Sr<sub>2</sub>TiSi<sub>2</sub>O<sub>8</sub> could not be grown from the stoichiometric melt, accompanying crystalline phase precipitated along with fresnoite-type crystal Sr<sub>2</sub>TiSi<sub>2</sub>O<sub>8</sub> makes it impossible to grow pure strontium titanium silicate single crystals by the usual crystal growing techniques<sup>[12-13]</sup>. Nevertheless, to get pure Sr<sub>2</sub>TiSi<sub>2</sub>O<sub>8</sub> crystals in glass, non-stoichiometric composition with rich-Si inside should be applied for crystal-growth suitability. For this point of view, the glass system with composition 33.3SrO-16.7TiO<sub>2</sub>-50SiO<sub>2</sub> was chosen for maintaining ratio Sr: Ti at 2:1.

### 6.2.1 The crystallization induced by fs laser

#### Glass Elaboration and laser irradiation

33.3SrO-16.7TiO<sub>2</sub>-50SiO<sub>2</sub> (mol%) glass was fabricated by a traditional method which was described in chapter 3. Irradiations were performed with a femtosecond laser system (Satsuma, Amplitude Systèmes Ltd.) operating at 1030 nm and delivering pulses of 300 fs at 300 kHz which is the optimized frequency for oriented crystallization<sup>[14]</sup>. The inscription was realized in pairs using a microscope objective (NA=0.6) 150 μm below the entry surface with a linear and polarization direction parallel/perpendicular to the scanning direction. The average pulse energy applied at the focus was changed from 0.1 to 2.0 μJ/pulse.

After writing lines, the sample was cleaved along the plane perpendicular to the written lines, polished to optical quality and subsequently etched in 2% hydrogen fluoride (HF) acid for 30 s. Then a Field-Emission Gun Scanning Electron Microscope (FEG-SEM ZEISS SUPRA 55 VP) was used for imaging and for analyzing the crystal orientation (Electron Back-Scattered Diffraction or EBSD) in the cross section of the lines. The chemical analysis Energy-dispersive X-ray spectroscopy (EDX) was also used to evaluate the compositional variation caused by the laser irradiation. SHG microscopy measurement were carried out in the same

experimental conditions used for inscription except that the focusing was with a smaller NA here and that applied pulse energy was below the threshold of glass modification. The probe polarization was linear and the 1030 nm light was filtered before the CCD.

### **Chemistry analysis in interaction volume**

The elemental distribution was examined in the interaction volume by EDX line scanning spectra as shown in figure 6.8. The shell-shaped gray part observed in SEM image (figure 6.8 (a)) implies the morphology of the cross-section of laser track after polishing and being etched by HF acid. It should be mentioned that the circumferential crystallized zone obtained in STS is quite different from that in LNS glass<sup>[14]</sup>. The write broad line, between the dashed lines and passing through the whole laser track, is a fracture generated during etching procedure. EDX line scanning spectra across the interaction volume at the head and at the tail have been realized as shown in figure 6.8 (b) and figure 6.8 (c), respectively.

To elucidate clearly, the interaction volume shown in figure 6.8 (a) was analyzed in 3 distinct regions: I-amorphous region at the center of laser track, II-crystallized region and III-glassy substrate. It is observed that there is no pronounced concentration change of Ti along the scanning line both at the head and at the tail in figure 6.8 (b)-(c). With respect to the Sr, the interested variation of concentration should be mentioned that is  $C_I(\text{Sr}) < C_{III}(\text{Sr}) < C_{II}(\text{Sr})$ , and this is the opposite case in term of Si which varied as  $C_I(\text{Si}) > C_{III}(\text{Si}) > C_{II}(\text{Si})$ . Normally, under a temperature gradient the network former trends to concentrate at the focal center of laser trace as a result of the elements strong bonded with oxygen tending to migrate to the hot region while the network modifiers have a tendency to migrate from the hot region to the cool region<sup>[15-16]</sup>. Here, the network modifier Sr prefers to migrate from the center to the edge of laser track while Si has a contrary tendency from the edge to the center. Moreover, in order to precipitate pure  $\text{Sr}_2\text{TiSi}_2\text{O}_8$  crystals in glass, more Sr but less Si is needed in 33.3SrO-16.7TiO<sub>2</sub>-50SiO<sub>2</sub> glass. This gives an additional assistance to the elemental migration inside and in the surroundings which should be parallel to the T gradient.

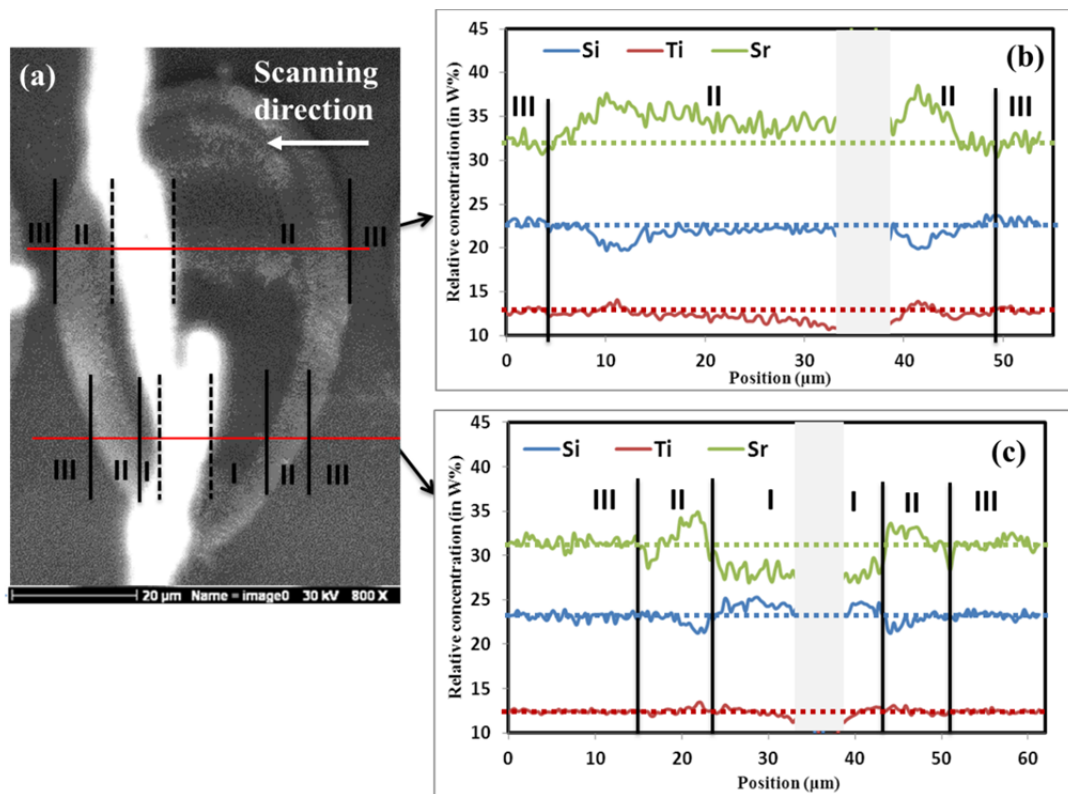


Figure 6.8 The SEM image (a) and EDX line scanning spectra (right to left) of the cross section of laser track at the head (b) and at the tail (c), respectively. The grey regions in (b) and (c) are the white fracture as shown in (a). The concentration in weight of each element in zone  $i$  ( $i=I, II, \text{ or } III$ ) is named as  $C_i$  (Si, Sr or Ti). The colored pointed-lines present the  $C_i$  in the parent glass to observe well the change tendency in zone I, II and III.

### 6.2.2 Asymmetric oriented crystallization induced by fs laser

Figure 6.9 is a series of images of laser lines cross section obtained by EBSD-scan technology performed with a step size of 200 nm. The shell-shaped laser track (written at 1.7  $\mu\text{J}$  pulse energy) were observed by the IQ (Image Quality) maps (figure 6.9 (a)) and IPF (Inversed Pole Figure) maps (figure 6.9 (b)) of EBSD-scan. The width and length of the line are  $\sim 45 \mu\text{m}$  and  $\sim 80 \mu\text{m}$ , respectively.

When a beam of SEM strikes a crystalline material mounted at an incline around  $70^\circ$ , the electrons disperse beneath the surface, subsequently diffracting among the crystallographic planes. Through this technology, we know that the white region in

figure 6.9 (a) is crystalline phase and the crystals are with  $\text{Sr}_2\text{TiSi}_2\text{O}_8$ -like lattice structure in the crystallized zone. It is obvious that the crystallized zone is symmetric transversally but not in longitudinal direction. The orientations of crystals in the shell-shaped region II by the color-coded orientation images in figure 6.9 (b). As illustrated, the c-axis  $\langle 001 \rangle$  of well-crystallized grains is oriented along the motion direction at the inner-head part of the interaction volume with a tilted angle around  $30^\circ$ , while surroundings in the circumferential zone have an asymmetric orientation from the left (pink color coded) to the right (green-blue color coded) as the appearance of different colors in figure 6.9 (b). As the absent of red color in right part of shell, there are not any c-axis  $\langle 001 \rangle$  of crystals orienting along the motion direction neither at the head of the laser track. Compared to EBSD images in figure 6.4, it seems that symmetrically oriented crystals were obtained at low writing velocity while randomly oriented crystals were usually precipitated at high velocity.

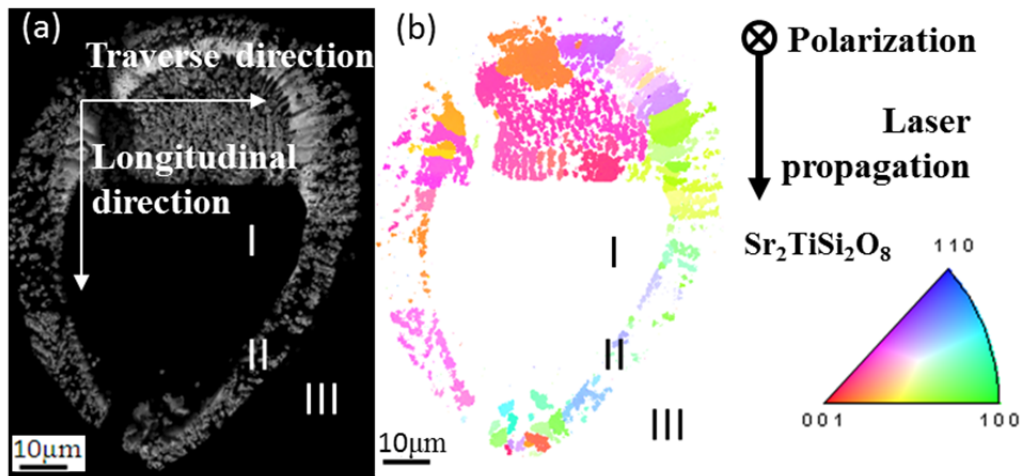


Figure 6.9 IQ maps (a) and IPF maps (b) of cross section of laser lines. Other laser parameters: 300 kHz,  $1.7 \mu\text{J}$ ,  $10 \mu\text{m/s}$ , 300 fs, 1030 nm,  $\text{NA} = 0.6$ , laser polarization is parallel to the written lines. The colors in IPF map of EBSD-scan based on  $\text{Pb}4\text{m}$  space group and  $\text{Sr}_2\text{TiSi}_2\text{O}_8$  crystal parameters indicate the crystal axis  $\langle a b c \rangle$  which is normal to the image plane.

### Nonlinear Optical Activity

As a kind of polar crystal,  $\text{Sr}_2\text{TiSi}_2\text{O}_8$  owns SHG-active structure with one strong

principal  $d_{33}$  nonlinear coefficient, therefore, the distribution of  $\text{Sr}_2\text{TiSi}_2\text{O}_8$  with polar-axis parallel to the applied polarization can be obtained by  $\mu$ -SHG map which can be also visually confirmed from the appearance of red color in the relative IPF maps<sup>[17]</sup>. The color gradient appearing in the  $\mu$ -SHG maps relates to the SH intensity of parallel component of c-axis to the probing polarization. Shell-shaped crystallization of  $\text{Sr}_2\text{TiSi}_2\text{O}_8$  is not only observed in the  $\mu$ -SHG images with vertical (longitudinal) and horizontal (transversal) polarization direction and but also in the corresponded IPF images in figure 6.10 (a-b), respectively. It should be mentioned that the compatibility of the crystal orientation maps of polar-axis and SH intensity map is not extremely perfect that should be due to the effective depth from the surface of EBSD ( $\sim 20\text{nm}$ ) and  $\mu$ -SHG ( $\sim 1\text{-}2\ \mu\text{m}$ ) and the possible inhomogeneous oriented crystallization in lines. In this case, SHG microscopy images and intensity curves according to the probed polarization azimuth were carried out to study the “quality” of crystal orientation along the same line.

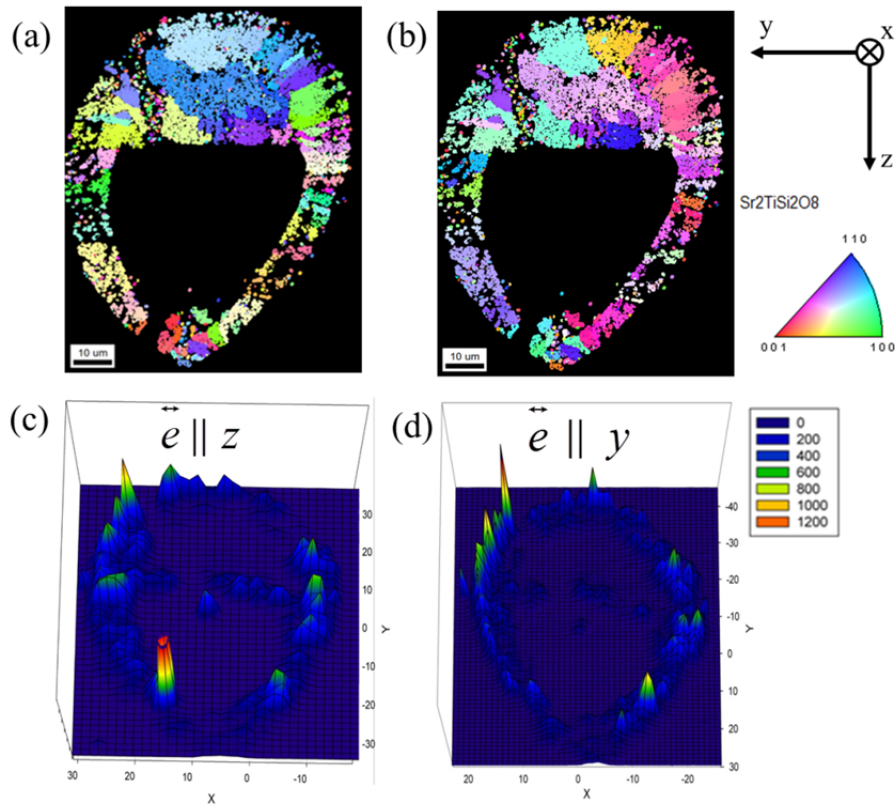


Figure 6.10 IPF images of EBSD-scan color coding the longitudinal (a) and transversal (b) orientation of polar-axis which are corresponding to the  $\mu$ -SHG mapping images with vertical (c) and horizontal (d) probing polarization of the cross-section of laser lines written at  $1.7 \mu\text{J}$  in  $10 \mu\text{m/s}$ , respectively. N. B. The colors in two IPF maps of EBSD-scan indicate the crystal axis  $\langle a b c \rangle$ , which is parallel to the applied polarization in (c) and (d), respectively.

To understand well the orientation of polar-axis of  $\text{Sr}_2\text{TiSi}_2\text{O}_8$  crystals in 3D (both in the cross-section and in lines), we have performed SHG microscopy measurement in lines.

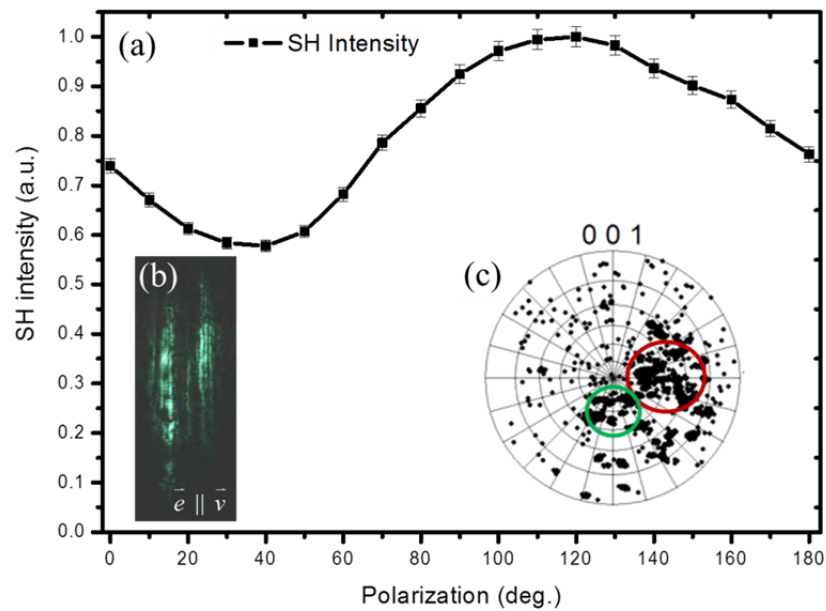


Figure 6.11 Polarization dependence of SH intensity of the written lines (a) at  $1.7 \mu\text{J}$   $150 \mu\text{m}$  below the glass surface as a function of probe polarization angle, and the line direction is at  $0^\circ$ . Insert images: (b) Second harmonic microscopy image of one line written at  $1.7 \mu\text{J}$  with probing polarization parallel to laser lines. (c) 001 pole figure obtained at the same polished laser track surface as in Fig. 1. N.B.: the laser focus has been enlarged and thus the probe intensity is below modification threshold during the SH intensity measurement.

The population of c-axis orientation can be deduced through recording the SH intensity using a photomultiplier as shown in figure 6.11 (a). As well, the SHG microscopy image of laser line was obtained as displayed in figure 6.11 (b). The exhibited green light of laser line with probed polarization along the writing direction indicates the existence of nonlinear  $\text{Sr}_2\text{TiSi}_2\text{O}_8$ -like fresnoite-crystals inside. This line is split into 2 parts which is contributed from the two sides of shell-shape crystallized zone. Noticeably, the inhomogeneous distribution of green light reveals a departure from single-crystallite along the lines. Moreover, the SHG intensity is lower at  $0^\circ$  with the applied polarization parallel to the laser lines than that at  $90^\circ$  in perpendicular case and the maximum (minimum) value appearing around  $120^\circ$  ( $30^\circ$ ) in the characteristic sine curve received in figure 6.11 (a).

Considering the orientation of crystals in cross-section given from IPF maps of

EBSD-scan before, the left and inner-head part of shell in the cross-section is parallel to the laser line but with a tilted angle as the appearance of mixed pink-red colors there in figure 6.9 (b), while the right part of shell is mostly perpendicular to the line with a smaller tilted angle shown by mixed blue-green colors. Combining with SH intensity curve, we speculate that the titled angle is probably around  $30^\circ$ . To verify this point of view, the  $\langle 001 \rangle$  pole figure was carried out based on figure 6.9 (b). As the center point in the pole figure represents the c-axis  $\langle 001 \rangle$  is normal to the plan, we found the orientations of crystals with their polar axis tilted by  $\theta = 30 \pm 15^\circ$  relative to the laser moving direction. The points circled by red line are consistent with the occurrence of pink-red colors in figure 6.9 (b). This preferential orientation of polar axis gives rise to the maximum SH intensity in figure 6.9 (a). Correspondently, the points in the green circle present the population of oriented crystal along x-axis with a tilted angle ( $\sim 15^\circ$ ) to z-axis which contributes to a portion of the SH intensity when the probe polarization is parallel to the laser line (at  $0^\circ$ ). Moreover, the minimum SH intensity is not an absolute zero value which might be due to the existence of randomly oriented crystals in laser lines.

### 6.2.3 Polarization direction and orientation writing dependence of crystallization orientation induced by fs laser.

We first look at the effects of polarization on crystallization during laser writing with applying different irradiation configurations performed by EBSD maps in figure 6.12. The quality of crystallization is dramatically decreased, that the pieces of micro-sized  $\text{Sr}_2\text{TiSi}_2\text{O}_8$  crystals are scattered at the interaction volume surroundings (figure 6.12 (a)), comparing to that in STS-1 under the same irradiation condition (figure 6.4(f)). The same phenomenon is observed when writing configuration is Yp-y (figure 6.12 (b)). Contrarily to both of them above, when fs laser is moved along y-axis facing the positive direction with linear polarization in x-axis, larger crystallized region appear at the surrounding, being similar to that in figure 6.4(f), but the preferential cruystallization orientation is more or less in the y-z plane which is coded by green-bluish color (figure 6.12 (c)). Furthermore, no obvious preferential

orientation of crystals in one direction is shown by their relevant  $\langle 001 \rangle$  pole figures in figure 6.12 (d)-(f).

The first evidence on the orientational dependence of oriented crystallization induced by fs laser is given in figure 6.13. This pair of laser lines was scribed in two directions along y-axis, negative orientation (figure 6.13 (a)) and positive orientation (figure 6.13 (b)), respectively. The precipitated crystals in these two laser tracks are in scale of micrometer and demonstrate that the formation is favoured at the surrounding when writing in positive direction. It seems that the parts of polar axis of crystals orientate to be normal to the y-z plane (or with a tilted angle around  $15^\circ$ ) in figure 6.13 (a) while polar axis of crystals obtained in case of Yp-x prefer to lie in the y-z plane as displayed in figure 6.13 (a). Moreover, relative larger crystallized regions with configurations Yp-x (figure 6.13 (a)) and Yn-x (figure 6.13 (b)) than that with configuration in Xp-x (figure 6.12 (a)) and Yp-y (figure 6.12 (b)) are observed.

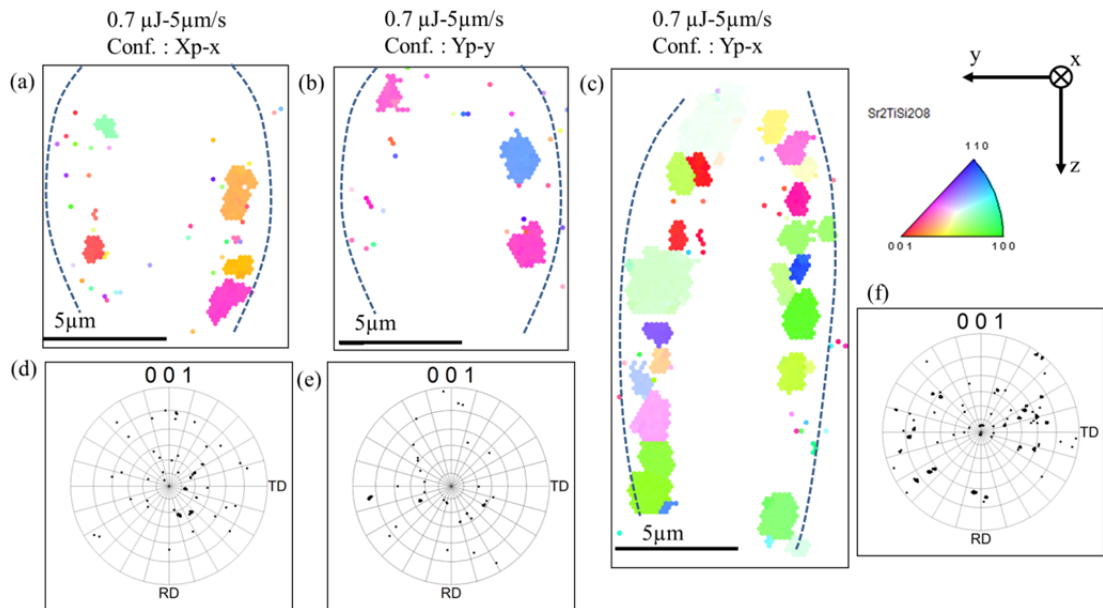


Figure 6.12 IPF EBSD maps of cross section of laser lines written at configuration Xp-x (a), Yp-y(b) and Yp-x(c) in STS-2 glass. The corresponding polar figures are displayed in (d), (e) and (f), respectively. Other laser parameters: 300 kHz, 0.7  $\mu\text{J}$ , 5  $\mu\text{m/s}$ , 300 fs, 1030 nm, NA = 0.6. The colors in IPF map of EBSD-scan based on Pb4m space group and  $\text{Sr}_2\text{TiSi}_2\text{O}_8$  crystal parameters indicate the crystal axis  $\langle a b c \rangle$  is normal to the image plane ( $\parallel x$  axis).

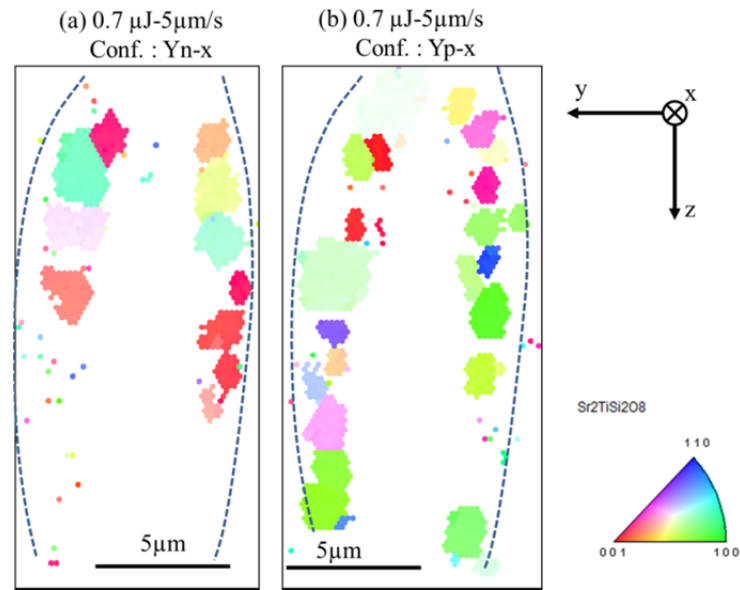


Figure 6.13 IPF EBSD maps of cross section of laser lines written at configuration Yn-x (a) and Yp-x(b) in STS-2 glass. Other laser parameters: 300 kHz, 0.7 μJ, 5 μm/s, 300 fs, 1030 nm, NA = 0.6.

### 6.3 Discussion

If an ultra-fast laser is focused into a transparent material, i.e. in glass, high laser energy flows into the material at micro-sized focal point as the occurrence of nonlinear multiphoton absorption. The heat accumulation happens at high repetition rate (typ. >100 kHz) as the interval time of two consecutive pulses is too short for the thermal diffusion. In this case, the local temperature increase appears and gives the possibility for space-selective crystallization. Actually, the temperature (T) distribution and T gradient are heavily depending on the applied pulse energy, repetition rate and thermal diffusion in terms of the thermal property of the material<sup>[18]</sup>. Those key points to the crystallization can be used to control crystalline size in the laser trace, large size if the stable temperature falls into the overlapping range of nucleation rate and growth rate, and small size if the stable temperature just stays in the nucleation process.

Indeed, temperature distribution and heat-modification during high-repetition-rate irradiation have been investigated in silicate glasses<sup>[18-22]</sup>. It reported that the outer-modified region should be due to the visco-elastic deformation

and the characteristic temperature is around transition temperature  $T_g^{[19]}$  with the consideration of temperature dependence of the specific heat. However, all of these investigations pointed out that the temperature at the focus center principally depends on the thermophysical properties of materials, characterized by thermal diffusivity  $D_{th}$  and conductivity  $\alpha$ , heat capacity  $C_p$ , density  $\rho$  and so on. The maximum temperature increase by one laser pulse  $\Delta T_0 = Q_0 / \rho C_p^{[19]}$  where  $Q_0$  is the maximum heat density at the focus by photoexcitation induced by one pulse. Since the approximated  $\rho C_p$  value of simulation in LNS glass<sup>[14]</sup> is around 1.2 times larger than that in STS glass in this thesis. Thus, the aftereffects of energy deposition in STS glass gives rise to much higher temperature at the focus center than that in LNS glass with the same irradiation parameter. This gives an explanation that larger interaction volumes, both in width and in length (around  $\sim 4$  times), are observed in STS glass than that in LNS glass. Moreover, higher pulse energy is applied, larger size of interaction region is induced. It is because applying higher pulse energy could deposit more heat density at the focus via nonlinear absorption.

Regarding to the velocity dependence laser-matter interaction, we found that varying laser motion velocity can induce slightly change in terms of the size of interaction volume. Since longer time of heat accumulation produce higher temperature at the focus center, lower motion velocity provides longer effective irradiation time on one point during the passage of laser and results in larger interaction volume. But the irregular change trend revealed by table 6.1 at 1.7  $\mu\text{J}$  is probably due to the density change with the appearance of  $\text{SrTiO}_3$  crystal ( $5.11 \text{ g/cm}^3$ ) and  $\text{Sr}_2\text{TiSi}_2\text{O}_8$  crystal ( $3.887 \text{ g/cm}^3$ )<sup>[13]</sup> in STS-1 glass ( $3.600 \text{ g/cm}^3$ )<sup>[23]</sup>. Moreover, since it reported that  $\text{Sr}_2\text{TiSi}_2\text{O}_8$  crystal could not be grown from the stoichiometric melt as in glass STS-1, more  $\text{SiO}_2$  should be added to get pure fresnoite-type crystals as in glass STS-2<sup>[13]</sup>. The phenomenon of crystalline phase transition in STS-1 glass, from pure  $\text{SrTiO}_3$ , the mixture of  $\text{SrTiO}_3$  and  $\text{Sr}_2\text{TiSi}_2\text{O}_8$  and then to pure  $\text{Sr}_2\text{TiSi}_2\text{O}_8$  crystalline phase either via decreasing pulse energy or via increasing laser motion velocity, reveals that  $\text{SrTiO}_3$  prefers to be precipitated at higher temperature than  $\text{Sr}_2\text{TiSi}_2\text{O}_8$ . Another solution is that the  $\text{Sr}_2\text{TiSi}_2\text{O}_8$  crystalline phase appears first at relative low temperature and high temperature could provide more energy in system

to dissociate the link  $\text{SiO}_2$  from  $\text{Sr}_2\text{TiSi}_2\text{O}_8$  to generate  $\text{SrTiO}_3$  as a result. But this point of view should be under discussion in future.

Furthermore, different shapes of crystallized zone have been exhibited both by SEM images and EBSD maps. As illustration in terms of crystallization mechanism induced by fs laser in chapter 5, we assume that the crystallization temperature range ( $T_{\max}-T_{\min}$ ) of STS glasses might be narrower than that of LNS glass. This might be one conceivable reason to produce crystallization in a shell form at high pulse energy and in the center at low pulse energy in STS glasses. Besides, the repeated laser irradiation at the focus results in a dramatically increase of temperature and high temperature gradient can be induced as a consequence. Since the temperature dependence of the chemical diffusion coefficient can be expressed by the Arrhenius-type equation  $D = D_0 \exp(-E_a R/T)$  where  $E_a$  is the activation energy and  $R$  is the gas constant<sup>[16, 24]</sup>. In this case, the modifiers with much larger diffusion coefficient such as Sr-O are weakly bonded and migrate to the outside, whereas strongly bonded ions like Si-O with lower diffusion coefficient migrate to the center of irradiated spot. Unlike in LNS glass, that the balance between thermal-migration and elemental diffusion for crystallization gives rise to no evidence of elemental migration in laser tracks described in chapter 5, when the heated element Sr tends to cross the crystallized zone II to amorphous zone III, relative low T and high viscosity make it difficult to move further. This leads to the accumulation of Sr at the frontier between zone II and III. Additionally, the formation of  $\text{Sr}_2\text{TiSi}_2\text{O}_8$  crystalline phase in STS-2 glass requiring less percentage of  $\text{SiO}_2$  gives an assistant to the concentrated element Si at the center (figure 6.8 (b)-(c)). This migration of constituent could form a suitable zone to precipitate crystals, such as shell-shaped in STS at high pulse energy. At the focus center, neither the composition nor high temperature at the center is suitable for the formation of  $\text{Sr}_2\text{TiSi}_2\text{O}_8$  fresnoite-type crystal with the lack of Sr and rich-Si at this moment. In case of low energy, low probability of element diffusion at focus center and suitable thermal environment may result in crystallization in the center of laser tracks but not at the surrounding (figure 6.4 (e)-(g)). Therefore, the aftereffect of thermal migration could be regarded as the second possible reason to get different distribution of crystallization should be. So far,

STS glass has been widely discussed as so-called “perfectly surface-crystallized” material<sup>[25]</sup> and it is thought that the formation of the SiO<sub>2</sub>-rich nanoparticles causes the matrix composition to approach that of Sr<sub>2</sub>TiSi<sub>2</sub>O<sub>8</sub> in SiO<sub>2</sub>-enriched non-stoichiometric glass, and thus the matrix tends to be transformed into the fresnoite crystal domain due to the surface crystallization with increasing temperature at which inhomogeneous nucleation occurs. The migration of constituent provides the condition for the crystallization of Sr<sub>2</sub>TiSi<sub>2</sub>O<sub>8</sub> via laser irradiation as well in our case. The inhomogeneous nucleation happens and dendrites like crystals in the crystallized area are observed from SEM images in figure 6.3.

It was believed that a Gaussian mode of a laser beam with light intensity distributed centro-symmetrically in 3D normally leads to a circular symmetric T distribution with a Gaussian attenuation in an isotropic medium. However, without the correction by SLM, the existence of self-absorption and spherical aberration is possible to break the symmetry of light intensity in the materials, but in longitudinal direction<sup>[26]</sup>. This leads to the asymmetric heated zone inside and then the longitudinal crystallized zone became asymmetric and ellipse shell-shaped with a filled head as presented in figure 6.9 (b).

The orientation of induced crystal is normally defined by the gradients of temperature and chemical potential during static irradiation. As the elemental redistribution is caused by thermal-migration effect, in other words, without the other force, the orientation of crystallization in fast growth direction should be towards the direction along the radial heat diffusion and elemental migration during static irradiation. However, the minimization of the variation in the surface energy gives rise to the fast formation nuclei with (001) plans parallel to the interface between the irradiated region and glass matrix in STS glass. Thus, inhomogeneous nucleation and following growth easily occurs at their and leads to a well radially oriented crystals with polar axis directing to the hot focus center<sup>[27]</sup> in figure 6.6.

When moving the laser, the material situated in front of the spot is heated at high temperature and potentially re-melted during the laser moving even if it started to crystallize at zone II. T gradient of the material after the focus spots in zone I turns to be parallel to the motion direction. Subsequently, crystals in zone II orient along the

motion direction but with an angular dispersion on the cross-section resulting from the competition between radially T gradient and parallel T gradient to motion direction. This induced a consequent maximum SHG intensity around  $120^\circ$  in figure 6.11(a) but not at  $0^\circ$  (parallel to the motion direction).

Noticeably, if the applied laser beam is symmetric in the transversal direction, the T gradient and chemical potential should be identical and symmetric from left side to right side. However, as observed in figure 6.9(b), the orientation of polar-axis of crystal in the left part and right part of laser track is not mirror symmetry as shown by the red color and green color respectively. Furthermore, the result in terms of polarization/direction-dependence crystallization exhibited in figure 6.12 and figure 6.13 implies that an asymmetric heat density and T gradient might appear during the ultra-short irradiation. Another possible affected factor such as a DC non-linear heat current originated from pulse front tilt (PFT) and polarization<sup>[28]</sup> under uniform illumination should be considered to give reasons for asymmetric T distribution as well as thermochemical gradient in the traversal direction of laser tracks cross-section. Moreover, these additional effects have also an impact on elemental migration<sup>[26]</sup>. The orientation of crystals was then driven to be asymmetric or the distribution of crystallization is not different either. This interesting phenomenon brings us some anticipation that using a prism or grating pairs to control intensity front, the controllable oriented crystallization of each part in the interacted region can be realized with ultra-short light pulses used for special frequency waveguide convert, for example.

## 6.4 Conclusion

To summarize, systematical studies of photo-induced crystallization in STS glass system have been taken via varying irradiation parameters. In stoichiometric STS-1 glass, 4 times larger of interaction volume is obtained comparing to that in LNS glass. Shell-shaped inhomogeneous nucleation crystallization in laser track has been observed at high pulse energy ( $\geq 1.3\mu\text{J}$ ), while centered crystallization in micro-sized has been obtained at low pulse energy ( $=0.7\mu\text{J}$ ). We assume that both the thermal

condition and element diffusion are important roles to get those different crystallized distributions. Moreover, the competition among T gradient, chemistry potential gradient and fast direction of crystallization drives the orientation of polar axis of crystals towards the laser writing direction, but with a tilted angle at some time. The configurational dependence of asymmetric orientational writing on crystallization is given, it reveals that not only the polarization can be an affected factor regarding to the laser writing as illustrated before, but also the direction of writing may influence the laser crystallization in glass.

## Reference

- [1]. Yang, P., Burns, G. R., Guo, J. P., *et al.*, Femtosecond laser-pulse-induced birefringence in optically isotropic glass. *J Appl Phys* **2004**, *95* (10), 5280-5283.
- [2]. Poumellec, B., Sudrie, L., Franco, M., *et al.*, Femtosecond laser irradiation stress induced in pure silica. *Opt Express* **2003**, *11* (9), 1070-1079.
- [3]. Gabelica-Robert, M., Tarte, P., Vibrational spectrum of fresnoite (Ba<sub>2</sub>TiOSi<sub>2</sub>O<sub>7</sub>) and isostructural compounds. *Phys Chem Miner* **1981**, *7* (1), 26-30.
- [4]. Serbena, F. C., Zanutto, E. D., Internal residual stresses in glass-ceramics: A review. *J Non-Cryst Solids* **2012**, *358* (6-7), 975-984.
- [5]. Le Parc, R., Levelut, C., Pelous, J., *et al.*, Influence of fictive temperature and composition of silica glass on anomalous elastic behaviour (vol 18, pg 7507, 2006). *J Phys-Condens Mat* **2009**, *21* (7).
- [6]. Davidge, R. W., Green, T. J., The strength of two-phase ceramic/glass materials. *J Mater Sci* **1968**, *3* (6), 629-634.
- [7]. Poumellec, B., Lancry, M., Chahid-Erraji, A., *et al.*, Modification thresholds in femtosecond laser processing of pure silica: review of dependencies on laser parameters [Invited]. *Opt Mater Express* **2011**, *1* (4), 766-782.
- [8]. Schaffer, C. B., Brodeur, A., Mazur, E., Laser-induced breakdown and damage in bulk transparent materials induced by tightly focused femtosecond laser pulses. *Meas Sci Technol* **2001**, *12* (11), 1784-1794.
- [9]. Petrov, P. K., Ivanov, Z. G., Gevorgyan, S. S., X-ray study of SrTiO<sub>3</sub> thin films in multilayer structures. *Materials Science and Engineering: A* **2000**, *288* (2), 231-234.
- [10]. Hoche, T., Russel, C., Neumann, W., Incommensurate modulations in Ba<sub>2</sub>TiSi<sub>2</sub>O<sub>8</sub>, Sr<sub>2</sub>TiSi<sub>2</sub>O<sub>8</sub>, and Ba<sub>2</sub>TiGe<sub>2</sub>O<sub>8</sub>. *Solid State Commun* **1999**, *110* (12), 651-656.
- [11]. Maitland, T., Sitzman, S., Backscattering Detector and EBSD in Nanomaterials Characterization. In *Scanning Microscopy for Nanotechnology*, Zhou, W.; Wang, Z., Eds. Springer New York: 2007; pp 41-75.
- [12]. Halliyal, A., Bhalla, A. S., Cross, L. E., *et al.*, Dielectric, piezoelectric and pyroelectric properties of Sr<sub>2</sub>TiSi<sub>2</sub>O<sub>8</sub> polar glass-ceramic: A new polar material. *J Mater Sci* **1985**, *20* (10), 3745-3749.
- [13]. Hoche, T., Neumann, W., Esmaeilzadeh, S., *et al.*, The crystal structure of Sr<sub>2</sub>TiSi<sub>2</sub>O<sub>8</sub>. *J Solid State Chem* **2002**, *166* (1), 15-23.

- [14]. Fan, C. X., Poumellec, B., Lancry, M., *et al.*, Three-dimensional photoprecipitation of oriented LiNbO<sub>3</sub>-like crystals in silica-based glass with femtosecond laser irradiation. *Opt Lett* **2012**, 37 (14), 2955-2957.
- [15]. Shimizu, M., Sakakura, M., Nishi, M., *et al.*, Control of element distribution in glass with femtosecond laser. *Laser-Based Micro- and Nanopackaging and Assembly VI* **2012**, 8244.
- [16]. Shimizu, M., Sakakura, M., Kanehira, S., *et al.*, Formation mechanism of element distribution in glass under femtosecond laser irradiation. *Opt Lett* **2011**, 36 (11), 2161-2163.
- [17]. Vigouroux, H., Fargin, E., Gomez, S., *et al.*, Synthesis and Multiscale Evaluation of LiNbO<sub>3</sub>-Containing Silicate Glass-Ceramics with Efficient Isotropic SHG Response. *Adv Funct Mater* **2012**, 22 (19), 3985-3993.
- [18]. Shimizu, M., Sakakura, M., Ohnishi, M., *et al.*, Mechanism of heat-modification inside a glass after irradiation with high-repetition rate femtosecond laser pulses. *J Appl Phys* **2010**, 108 (7).
- [19]. Shimizu, M., Sakakura, M., Ohnishi, M., *et al.*, Three-dimensional temperature distribution and modification mechanism in glass during ultrafast laser irradiation at high repetition rates. *Opt Express* **2012**, 20 (2), 934-940.
- [20]. Eaton, S., Zhang, H., Herman, P., *et al.*, Heat accumulation effects in femtosecond laser-written waveguides with variable repetition rate. *Opt. Express* **2005**, 13 (12), 4708-4716.
- [21]. Eaton, S. M., Zhang, H., Ng, M. L., *et al.*, Transition from thermal diffusion to heat accumulation in high repetition rate femtosecond laser writing of buried optical waveguides. *Opt. Express* **2008**, 16 (13), 9443-9458.
- [22]. Sakakura, M., Shimizu, M., Shimotsuma, Y., *et al.*, Temperature distribution and modification mechanism inside glass with heat accumulation during 250 kHz irradiation of femtosecond laser pulses. *Appl Phys Lett* **2008**, 93 (23).
- [23]. Halliyal, A., Safari, A., Bhalla, A. S., *et al.*, Grain-Oriented Glass-Ceramics for Piezoelectric Devices. *J Am Ceram Soc* **1984**, 67 (5), 331-335.
- [24]. Qiu, J. R., Femtosecond laser-induced microstructures in glasses and applications in micro-optics. *Chem Rec* **2004**, 4 (1), 50-58.
- [25]. Takahashi, Y., Yamazaki, Y., Ihara, R., *et al.*, Parasitic amorphous on single-domain crystal: Structural observations of silicate glass-ceramics. *Sci Rep-Uk* **2013**, 3.
- [26]. Zhong, M., Du, Y., Ma, H., *et al.*, Crystalline phase distribution of Dy<sub>2</sub>(MoO<sub>4</sub>)<sub>3</sub> in glass induced by 250 kHz femtosecond laser irradiation. *Opt. Mater. Express* **2012**, 2 (8), 1156-1164.
- [27]. Maury, N., Cambier, F., Gonon, M., Bulk crystallisation of (001) oriented fresnoite Sr<sub>2</sub>TiSi<sub>2</sub>O<sub>8</sub> in glass-ceramics of the Sr-Ti-Si-K-B-O system. *J Non-Cryst Solids* **2011**, 357 (3), 1079-1084.
- [28]. Yang, W. J., Kazansky, P. G., Svirko, Y. P., Non-reciprocal ultrafast laser writing. *Nat Photonics* **2008**, 2 (2), 99-104.

## Chapter 7 Summery and perspective

### 7.1 Summery of thesis

Owing to low cost, easy fabrication and stable nonlinear optical properties, glasses containing oriented nonlinear crystals in scale of nano/micrometer own great potential application on optical telecommunication, integrated optical devices, etc. In this thesis, we discussed how to control crystallization behavior of oxide crystals, particularly oriented nano/micro-crystallization, in different glasses treated under additional fields (heat treatment and ultra-short laser irradiation). We found that the controllable crystallization (e.g. phase, size, distribution, orientation, etc.) and nonlinear optical properties can be achieved via varying parameters of treatments.

The 2.0SrO-1.0TiO<sub>2</sub>-2.9SiO<sub>2</sub> (mol%) glass was put in an additional heat field after annealing. Maker fringes method was first utilized for characterizing the crystallization behavior in varying the temperature and time of heat treatment. As implied by the results of transmission spectroscopy, higher temperature was applied, lower transmittance of treated samples was obtained. The SHG responses appeared in Maker fringes measurement since treatment condition was 850°-2h. In this case, the oriented fresnoit-type crystals Sr<sub>2</sub>TiSi<sub>2</sub>O<sub>8</sub> were formed in glass exhibited by XRD results. Moreover, if increasing temperature or prolonging treatment duration, the maximum SHG intensity shifted from 40° towards 0°. Combining the XRD and SEM images, we assumed that nucleation and crystal growth happened at surface of glass at first, and then with thickness of crystallized layer being larger, these two processes extended towards the interior of bulk to result in the formation of disordered crystals inside. We also simulated the experimental results and proposed that Maker fringes method can be not only regarded as a tool to characterize the second-order nonlinear property of material, but also a means to analyze the crystallization process of glass.

Heat treatment is easy proceeding, but its disadvantages, such as long period during the treatment and poor controllability, limit the realization of controllable 3D crystallization in glass. Thus, due to achievable space-selectively crystallization, we

discussed then the femtosecond laser irradiation induced controllable crystallization in glass.

From the previous work in terms of laser irradiation in silicate glass, we focused femtosecond laser in LNS glasses and achieved space-selective crystallization inside. After characterization by EBSD method, we found that controllable crystallization in size and orientation of nonlinear crystals can be realized via varying the writing pulse energy and polarization direction. When polarization is parallel to the writing direction, laser-induced oriented nano-crystallization occurred if applying low pulse energy. When polarization is in perpendicular case, nano-crystals can be also obtained during high pulse energy writing, but without population of orientation. According to EDX/WDS and nuclear microprobe analysis, we do not observed any obvious concentration fluctuation of each element in the interaction volume, neither in the laser propagation direction nor along laser line direction. It elucidated that element Si might distribute homogeneously in laser track as a constituent of SiO<sub>2</sub>-nanocrystals. SHG intensity evaluation depending on polarization azimuth implied that polar axis of precipitated crystals at high pulse energy was along writing direction, while being in perpendicular direction at low pulse energy, which was consistent with EBSD results. Moreover, different sizes of laser beam were used to verify the orientation of crystals in pairs of laser tracks. The results indicated that polar axis of crystals in two laser tracks oriented in the same direction that is determined with the orientation of crystals in the initial laser line. The mechanism of controllable laser-induced crystallization in LNS glass was discussed and ultra-short laser irradiation can be used efficiently to design and produce novel nonlinear materials in future.

After that, we turned back to investigate crystallization in STS glass during fs laser irradiation. In stoichiometric composition STS-1 glass, the interaction volume was about 4 times larger than that in LNS glass at the same irradiation parameter because of a higher temperature induced at the focus center in STS-1 glass. Different morphologies of laser trace cross-section were observed. The shell-shaped crystallized zone was gained at high pulse energy ( $\geq 1.3\mu\text{J}$ ) and micro-sized crystallization at center of laser trace was achieved at low energy ( $=0.7\mu\text{J}$ ). The connected and dendritic crystals indicated that nucleation process might be

inhomogeneous. Contrary to that in LNS glass, obvious concentration fluctuation of Si and Sr elements occurred as the aftereffects of laser irradiation. The temperature distribution and thermo-migration were supposed as the origin of different morphologies of crystallized zone. Besides, pure  $\text{SrTiO}_3$  phase was obtained at high pulse energy with low writing velocity. This phase translated into  $\text{Sr}_2\text{TiSi}_2\text{O}_8$  when pulse energy was lower with faster writing velocity. This might be originated from different temperatures with varying laser irradiation parameters. We also reported that with the combined actions of temperature gradient and chemical potential gradient, polar axis of crystals in laser traces were towards the writing direction with a dispersion angle and were independent on the pulse energy. In STS-2 sample, the glass with non-stoichiometric composition, pure  $\text{Sr}_2\text{TiSi}_2\text{O}_8$  crystalline phase precipitated and polar axis of crystals orientated asymmetrically in the crystallized zone. We found that the orientation of crystals depends on the polarization direction and writing direction. It deduced that the concurrent contributions of the polarization and of PFT might give rise to the orientation of polarization and writing depending crystallization during ultra-short laser irradiation.

## 7.2 Perspective

As summarized, this thesis involves systematical works concerning controllable nano/micro-crystallization in silicate glass either by traditional treatment or by modern ultra-short laser irradiation to provide possibilities for fabricating optical elements or devices as one's will via controlling nonlinear optical properties of material. But, there are still some novel challenges or untouched problems. For instance, it needs to complete the simulation of ultra-short laser nonlinear propagation, to determine the exact function of PFT during laser irradiation particularly in term of oriented crystallization, and to define the crystallization thresholds in different glass systems.

Therefore, the next step is to perform a simulated model of nonlinear propagation of femtosecond laser in glass, the mechanism of crystallization during irradiation, and the impact of PFT for oriented crystallization. This work will be a

guidance for controllable laser-matter interaction, especially for orienting nano/micro-crystallization in glass, to some extent.

To find the nano/micro-crystallization thresholds via irradiating glasses with typical compositions (e.g. well-formed glass composition inside the glass-forming region, potentially crystallized composition at the frontier of glass-forming region, etc.) is another unaccomplished work in future. In this thesis, we found that the crystallization behavior is also sensitive to the glass initial composition. Therefore, it needs to verify the compositional effect through the determination of crystallization threshold in other glass system, and to discuss the possibility of controllable precipitation of nonlinear crystals in glass further. Moreover, the quality of 3D crystallization in glass should be improved imperatively which is the key for the industrial producing and application

## Appendix SHG simulation

According to the discussion involving nonlinear optics in chapter 2, we simulated the Maker fringes measurement to understand the mechanism of second harmonic generation in nonlinear medium.

Given a homogeneous nonlinear medium, the fundamental incident beam with power  $P_\omega$  pass through it along the direction of wave vector and the polarization is parallel to the  $y'$ -axis. The beam Gaussian radius is  $\omega_0$  and the thickness of transparent material is  $L$ . The angle between incident beam and normal direction of entry surface is  $\theta$ . The fundamental wave propagates through the entry surface and its polarization is in  $x'y'$  plane with an angle  $\phi$  to  $x'$ -axis. If the polarization is parallel to  $y'$ -axis, i.e.  $\phi=\pi/2$ , we defined it as “p” direction, and it is named as “s” direction if it is parallel to  $x'$ -axis. The following calculation has achieved by MathCAD software.

## Annexe 1: SHG simulation

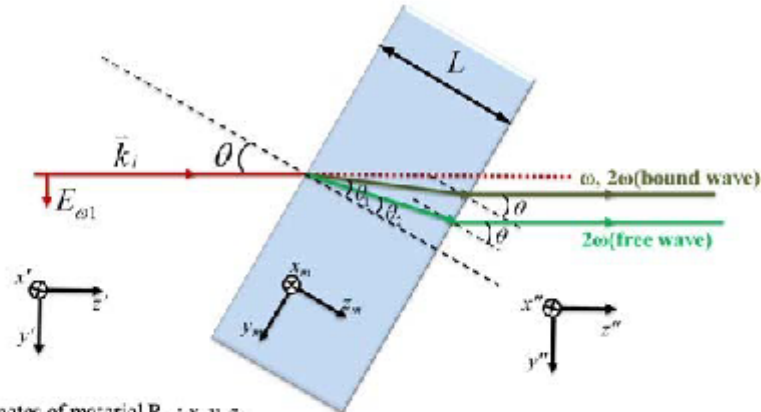
Rv est le repère attaché à l'onde incidente.

Rm est le repère dans le matériau

y, z' ou y,z est le plan d'incidence.

anticlockwise is plus  
clockwise is minus

Rm est le repère fixé sur le dioptre entré, mais pas necessairement sur les axes de symétrie du matériau.



Coordinates of material  $R_m : x_m, y_m, z_m$   
of incident beam  $R_v : x_v, y_v, z_v$   
of transmitted beam  $R_t : x_t, y_t, z_t$   
of crystallographic geometry  $R_c : x_c, y_c, z_c$   
Incident plan: y-z plan and y'-z' plan

x est perpendiculaire au plan d'incidence.

### Divers constantes et paramètres entrants

$$\lambda := 1.064 \cdot 10^{-6} \text{ m}$$

la longueur d'onde du laser dans le vide

$$\text{Paverage} := 0.002 \cdot \text{W}$$

la puissance moyenne incidente

$$\text{Repetrate} := 100 \cdot \text{Hz}$$

$$\text{FWHM} := 100 \cdot 10^{-9} \cdot \text{s}$$

$$w0 := 100 \cdot 10^{-6} \cdot \text{m}$$

le rayon du faisceau Gaussien

$$L := 1.830 \cdot 10^{-3} \cdot \text{m}$$

l'épaisseur de l'échantillon

$$c := 2.997 \cdot 10^8 \cdot \frac{\text{m}}{\text{s}}$$

la vitesse de la lumière

$$\epsilon_0 := \frac{10^7 \cdot (\text{C} \cdot \text{m})}{4 \cdot \pi \cdot c^2 \cdot (\text{V} \cdot \text{s}^2)}$$

$\epsilon_0 = \epsilon_0$

$$P_{\omega} := \text{Paverage} \cdot \frac{\text{Repetrate}}{\text{FWHM}} \cdot \frac{1}{\pi \cdot w0^2}$$

$$\text{Paverage} \cdot \frac{\text{Repetrate}}{\text{FWHM}} = \text{puissance pic}$$

peak power density

$P_{\omega} = \mathbf{I}$

$$n_{\omega} := 1.534 \quad n_{2\omega} := 1.547 \text{ (quartz)} \quad n_{air} := 1 \quad L_{coh} := \frac{\lambda}{4(n_{2\omega} - n_{\omega})}$$

$$\omega := \frac{2 \cdot \pi \cdot c}{\lambda}$$

$L_{coh} = \mathbf{I}$

dans le matériau 1: l'air

$$k_i := n_{air} \cdot \frac{\omega}{c} \quad k_{tr} := n_{air} \cdot \frac{\omega}{c} \quad k_t := n_{\omega} \cdot \frac{\omega}{c} \quad k_r := n_{air} \cdot \frac{2\omega}{c} \quad \text{groupe 32-D}_3$$

dans le matériau 2: non-linéaire

$$k_f := n_{2\omega} \cdot \frac{2\omega}{c} \quad k_b := n_{\omega} \cdot \frac{2\omega}{c} \quad k_{2r} := n_{2\omega} \cdot \frac{2\omega}{c}$$

dans le matériau 3: l'air

$$k_{2t} := n_{air} \cdot \frac{2\omega}{c}$$

D'après la loi de conservation des composantes tangentielles des vecteurs d'onde, on a les relations suivantes:

$$\theta_1(\theta) := \text{asin}\left(\frac{\sin(\theta)}{n_{\omega}}\right) \quad \theta = \text{angle d'incidence, } \theta_1 = \text{angle que fait l'onde réfractée à } \omega \text{ avec l'axe z}$$

Loi de Snell-Descarte:  $\sin(\theta) = n_{\omega} \sin(\theta_1)$

$$\theta_3(\theta) := \text{asin}\left(\frac{\sin(\theta)}{n_{2\omega}}\right) \quad \theta_3 = \text{angle que fait l'onde liée } 2\omega \text{ avec l'axe z}$$

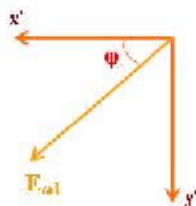
Loi de Snell-Descarte:  $\sin(\theta) = n_{2\omega} \sin(\theta_3)$

$$B(\psi) := \begin{pmatrix} 1 & 0 & 0 \\ 0 & \cos(\psi) & -\sin(\psi) \\ 0 & \sin(\psi) & \cos(\psi) \end{pmatrix}$$

**N.B.** La matrice B exprime, un vecteur du repère de départ, dans le repère d'arrivée, si l'angle  $\psi$  est orienté du z du repère d'arrivée vers le z du repère de départ.

### Le faisceau incident:

La polarisation du faisceau incident est dans le plan ( $x'$ ,  $y'$ ) du repère  $R_v$ .  $y'$  correspond à la polarisation "p",  $x'$  correspond à la polarisation "s".



**N.B.** L'unité du champ électrique est:  $V/m = m\ddot{a}kg\cos^{-3}A^{-1}$

$$E := \sqrt{2 \frac{P_{\omega}}{\epsilon_0 \cdot c \cdot n_{air}}} \quad E = \mathbf{I}$$

L'expression du champ électrique dans  $R_v$  est:  $E_{\omega 1}(\phi) := \begin{pmatrix} \cos(\phi) \\ \sin(\phi) \\ 0 \end{pmatrix} \cdot E$

### Le champ électrique fondamental:

A partir de la formule de Fresnel, les facteurs de transmission de l'amplitude des composantes "s" et "p" du champ électrique sont pour une transmission à la fréquence  $\omega$  de l'air au matériau:

$$t_{ux}(\theta) := \frac{\cos(\theta) \cdot (k_{tr} + k_i)}{k_{tr} \cdot \cos(\theta) + k_t \cdot \cos(\theta_1(\theta))} \quad x \text{ est perpendiculaire au plan d'incidence.}$$

$$t_{uy}(\theta) := \frac{\cos(\theta) \cdot (k_{tr} + k_i)}{\cos(\theta_1(\theta)) \cdot k_{tr} + k_t \cdot \cos(\theta)} \quad y, z \text{ est le plan d'incidence.}$$

On peut définir la matrice suivante qui transforme le vecteur champ électrique de l'onde incidente dans le repère Ri (attaché à l'onde incidente), en celui de l'onde transmise dans le repère Rt (attaché à l'onde transmise).

$$t_{\omega}(\theta) := \begin{pmatrix} t_{\omega x}(\theta) & 0 & 0 \\ 0 & t_{\omega y}(\theta) & 0 \\ 0 & 0 & 0 \end{pmatrix}$$

**N.B.** Les coefficients de la matrice ci-dessus correspond est bien à ceux reportés par N.Bloembergen, 1962, Physical Review, 128(2) page 606.

En utilisant la matrice B appropriée, on obtient ensuite le champ électrique dans le repère Rm

$$E_{\omega m}(\phi, \theta) := B(\theta)(\theta) \cdot t_{\omega}(\theta) \cdot E_{\omega 1}(\phi)$$

**N.B.** Le vecteur  $E_{\omega m}$  est nécessairement un vecteur perpendiculaire à la direction de propagation de l'onde transmise.

### L'expression du champ électrique harmonique:

L'équation de propagation non-linéaire dans le matériau supposé uniforme est:

$$\vec{\nabla} \wedge \vec{\nabla} \wedge \vec{E}_{2\omega}(\vec{r}, t) + \epsilon_{2\omega} \mu_0 \frac{\partial \vec{E}_{2\omega}(\vec{r}, t)}{\partial t^2} = -\mu_0 \frac{\partial \vec{P}_{2\omega}(\vec{r}, t)}{\partial t^2}$$

$$\text{Ou } \vec{\nabla} \wedge \vec{\nabla} \wedge \vec{E}(\vec{r}) - \frac{n_{2\omega}^2 A \omega^2}{c^2} \vec{E}(\vec{r}) = \frac{4\omega^2}{c^2 \epsilon_0} \vec{P}(\vec{r})$$

La forme de solution de l'équation de propagation non-linéaire est une somme d'une solution de l'équation homogène et d'une autre, particulière, de l'équation complète, i.e.:

$$\vec{E}_{2\omega} = \vec{E}_f \exp(i\vec{k}_{2\omega f} \vec{r}) + \vec{E}_b \exp(i\vec{k}_{2\omega b} \vec{r})$$

avec:

$$\vec{E}_b = \left[ \vec{P} - \frac{\vec{k}_{2\omega b} (\vec{k}_{2\omega b} \vec{P})}{k_{2\omega b}^2} \right] \frac{1}{\epsilon_0 (n_{2\omega}^2 - n_{2\omega f}^2)}$$

$$\vec{k}_{2\omega b} = 2\vec{k}_i$$

**N.B.**  $\vec{E}_f$  est une onde libre d'où  $\vec{E}_f$  est perpendiculaire à  $\vec{k}_{2\omega f}$   
Ce n'est pas le cas de  $\vec{E}_b$

**N.B.**  $\vec{E}_b$  est une solution particulière, donc totalement définie en amplitude et en direction de propagation dans le milieu non-linéaire par le champ  $E_{\omega m}$ .

$$k_{2\omega b}(\theta) := \begin{pmatrix} 0 \\ -\sin(\theta) \\ \cos(\theta) \end{pmatrix} \cdot \vec{k}_b$$

$k_{2\omega b}(\theta)$  = le vecteur d'onde liée dans le milieu, exprimé dans le repère Rm

### La polarisation et le tenseur $\chi^{(2)}$ :

Le vecteur de polarisation est défini par  $\vec{P} = \frac{\epsilon_0}{2} \chi^{(2)} \vec{E}_{\omega} \vec{E}_{\omega}$  où  $\chi^{(2)} = 2d$  source: Handbook of Laser Science and Technology

Du fait de la symétrie du tenseur  $\chi^{(2)}$ , on peut écrire, pour les matériaux qui ne possèdent pas de symétrie,

$$\frac{\chi^{(2)}}{2} = \begin{pmatrix} d_{11} & d_{12} & d_{13} & d_{14} & d_{15} & d_{16} \\ d_{21} & d_{22} & d_{23} & d_{24} & d_{25} & d_{26} \\ d_{31} & d_{32} & d_{33} & d_{34} & d_{35} & d_{36} \end{pmatrix}$$

Les conventions sont les suivantes

$$1 = 11 \quad 4 = 23 = 32$$

$$2 = 22 \quad 5 = 13 = 31$$

$$3 = 33 \quad 6 = 12 = 21$$

Compte tenu du groupe ponctuel du cristal  $\alpha$ -quartz(D32), le tenseur dans le référentiel du cristal se réduit à celui ci-dessous.

## Appendix-SHG simulation

on définit:  $pm := 10^{-12} \cdot m$

$$d11 := 0.60 \cdot \frac{pm}{V} \quad d14 := 0.00 \cdot \frac{pm}{V}$$

$$\frac{\chi^{(2)}}{2} = \begin{pmatrix} d11 & -d11 & 0 & d14 & 0 & 0 \\ 0 & 0 & 0 & 0 & -d14 & -d11 \\ 0 & 0 & 0 & 0 & 0 & 0 \end{pmatrix}$$

**N.B.** Le référentiel Rc est tel que l'axe z correspond à l'axe 3, et l'axe x à l'axe 2

$$A(i,j,k) := \begin{cases} d11 & \text{if } i = 1 \wedge j = 1 \wedge k = 1 \\ -d11 & \text{if } i = 1 \wedge j = 2 \wedge k = 2 \\ -d11 & \text{if } i = 2 \wedge j = 1 \wedge k = 2 \\ -d11 & \text{if } i = 2 \wedge j = 2 \wedge k = 1 \\ d14 & \text{if } i = 1 \wedge j = 2 \wedge k = 3 \\ d14 & \text{if } i = 1 \wedge j = 3 \wedge k = 2 \\ -d14 & \text{if } i = 2 \wedge j = 1 \wedge k = 3 \\ -d14 & \text{if } i = 2 \wedge j = 3 \wedge k = 1 \\ 0 \cdot \frac{pm}{V} & \text{otherwise} \end{cases}$$

$A(i,j,k)$  soit les composantes du tenseur  $\chi^{(2)}/2$  dans le repère Rc.

Parce que l'on fait tous les calculs dans le repère Rm, on doit transformer le tenseur A du repère du cristal Rc au repère Rm. Dans le repère Rm, A est noté Am. Pour construire la matrice de changement de base Bcm, on remarque que la première colonne est l'expression du vecteur de base xc du cristal exprimé dans le repère Rm, de même pour le vecteur

$$y_c \begin{matrix} \rightarrow \\ \rightarrow \\ \rightarrow \end{matrix} = \begin{pmatrix} \alpha_x & \beta_x & \gamma_x \\ \alpha_y & \beta_y & \gamma_y \\ \alpha_z & \beta_z & \gamma_z \end{pmatrix} \begin{pmatrix} x \\ y \\ z \end{pmatrix} = \begin{pmatrix} \alpha_x & \beta_x & \gamma_x \\ \alpha_y & \beta_y & \gamma_y \\ \alpha_z & \beta_z & \gamma_z \end{pmatrix} \begin{pmatrix} x_c \\ y_c \\ z_c \end{pmatrix}$$

i.e. les coordonnées des vecteurs de base de Rm ( $x, y, z$ ) dans la base Rc ( $x_c, y_c, z_c$ )

la matrice de changement de base Bcm entre les deux repères Rc et Rm (du repère du cristal Rc au repère Rm) s'exprime par la matrice suivante à partir des expressions de x, y, z au dessus:

On suppose que l'axe polaire du cristal ( $z_c$ ) est perpendiculaire au dioptre d'entrée (z-cut) et l'axe  $x_c$  fait un angle  $\alpha$  avec l'axe x dans le base Rm. La rotation s'effectue autour de l'axe z.

$$Bcm(\alpha) := \begin{pmatrix} \cos(\alpha) & -\sin(\alpha) & 0 \\ \sin(\alpha) & \cos(\alpha) & 0 \\ 0 & 0 & 1 \end{pmatrix} \quad Bcm(\alpha)^{-1} = \begin{pmatrix} \cos(\alpha) & \sin(\alpha) & 0 \\ -\sin(\alpha) & \cos(\alpha) & 0 \\ 0 & 0 & 1 \end{pmatrix}$$

le champ électrique  $\vec{E}_{\omega m}$  et la polarisation  $\vec{P}_{\omega m}$  dans le repère  $R_c$  sont :

$$\vec{E}_{\omega m} = B_{cm} \vec{E}_{\omega c} \quad \vec{P}_{\omega m} = B_{cm} \vec{P}_{\omega c}$$

On obtient la relation suivante:

$$P(\alpha, \phi, \theta) := B_{cm}(\alpha) \cdot \begin{bmatrix} \sum_{j=1}^3 \sum_{k=1}^3 \left[ A(1,j,k) \cdot \left( B_{cm}(\alpha)^{-1} \cdot E_{\omega m}(\phi, \theta) \right)_j \cdot \left( B_{cm}(\alpha)^{-1} \cdot E_{\omega m}(\phi, \theta) \right)_k \right] \\ \sum_{j=1}^3 \sum_{k=1}^3 \left[ A(2,j,k) \cdot \left( B_{cm}(\alpha)^{-1} \cdot E_{\omega m}(\phi, \theta) \right)_j \cdot \left( B_{cm}(\alpha)^{-1} \cdot E_{\omega m}(\phi, \theta) \right)_k \right] \\ \sum_{j=1}^3 \sum_{k=1}^3 \left[ A(3,j,k) \cdot \left( B_{cm}(\alpha)^{-1} \cdot E_{\omega m}(\phi, \theta) \right)_j \cdot \left( B_{cm}(\alpha)^{-1} \cdot E_{\omega m}(\phi, \theta) \right)_k \right] \end{bmatrix}$$

**N.B.** On oublie  $\epsilon_0$  ici. Car il disparaît ensuite dans les calculs.

**N.B.**  $\vec{P}$  est dans  $R_m$  car  $E$  et  $A$  sont dans  $R_m$ .

### le calcul du champ électrique harmonique:

$$E_b(\alpha, \phi, \theta) := \left[ P(\alpha, \phi, \theta) - \frac{k2\omega b(\theta) \cdot (k2\omega b(\theta) \cdot P(\alpha, \phi, \theta))}{k^2} \right] \cdot \frac{1}{n\omega^2 - n2\omega^2}$$

L'expression de  $E_f$  en fonction de  $E_b$  et le vecteur d'onde  $k_f$ , est définie par la continuité des vecteurs d'onde à  $2\omega$ , d'une part, et par la continuité des composantes tangentielles de  $E$  et  $H$ , d'autre part sur le dioptré d'entrée. Ce calcul est effectué en annexe 2. On obtient le résultat ci-dessous.

$$T_f(\theta) := \begin{pmatrix} \frac{k_r \cdot \cos(\theta) + k_b \cdot \cos(\theta_1(\theta))}{k_f \cdot \cos(\theta_3(\theta)) + k_r \cdot \cos(\theta)} & 0 & 0 \\ 0 & -\cos(\theta_3(\theta)) \cdot \frac{\cos(\theta_1(\theta)) \cdot \cos(\theta) \cdot k_b + k_r}{\cos(\theta_3(\theta)) \cdot k_r + k_f \cdot \cos(\theta)} & \frac{\cos(\theta_3(\theta)) \cdot \sin(\theta_1(\theta)) \cdot \cos(\theta) \cdot k_b}{\cos(\theta_3(\theta)) \cdot k_r + k_f \cdot \cos(\theta)} \\ 0 & -\sin(\theta_3(\theta)) \cdot \frac{\cos(\theta_1(\theta)) \cdot \cos(\theta) \cdot k_b + k_r}{\cos(\theta_3(\theta)) \cdot k_r + k_f \cdot \cos(\theta)} & \frac{\sin(\theta_3(\theta)) \cdot \sin(\theta_1(\theta)) \cdot \cos(\theta) \cdot k_b}{\cos(\theta_3(\theta)) \cdot k_r + k_f \cdot \cos(\theta)} \end{pmatrix}$$

et  $E_f(\alpha, \phi, \theta) := T_f(\theta) \cdot E_b(\alpha, \phi, \theta)$

### La transmission du milieu non-linéaire à l'air à la fréquence $2\omega$

On peut exprimer le champ transmis en fonction de  $E_f$  et  $E_b$  de la manière suivante:

$$\vec{E}_{2\omega t} = T_{2f} \vec{E}_f \exp(i\vec{k}_f \vec{r}) + T_{2b} \vec{E}_b \exp(i\vec{k}_b \vec{r})$$

A partir de la condition de continuité des champs électriques et des champs magnétiques sur le deuxième dioptré, on obtient les matrices  $T_{2f}$  et  $T_{2b}$  suivantes (Le calcul est effectué dans l'annexe 3 avec  $\vec{E}_f$  et  $\vec{E}_b$  dans  $R_m$  mais  $\vec{E}_{2\omega t}$  dans  $R_t$ ) :

$$T2f(\theta) := \begin{bmatrix} \frac{(k2r + kf) \cdot \cos(\theta3(\theta))}{k2r \cdot \cos(\theta3(\theta)) + k2t \cdot \cos(\theta)} & 0 & 0 \\ 0 & \frac{(k2r + kf) \cdot \cos(\theta3(\theta))^2}{\cos(\theta) \cdot k2r + k2t \cdot \cos(\theta3(\theta))} & \frac{\cos(\theta3(\theta)) \cdot \sin(\theta3(\theta)) \cdot (k2r + kf)}{\cos(\theta) \cdot k2r + k2t \cdot \cos(\theta3(\theta))} \\ 0 & 0 & 0 \end{bmatrix}$$

$$T2b(\theta) := \begin{bmatrix} \frac{k2r \cdot \cos(\theta3(\theta)) + kb \cdot \cos(\theta1(\theta))}{k2r \cdot \cos(\theta3(\theta)) + k2t \cdot \cos(\theta)} & 0 & 0 \\ 0 & \frac{\cos(\theta1(\theta)) \cdot \cos(\theta3(\theta)) \cdot kb + k2r}{\cos(\theta) \cdot k2r + k2t \cdot \cos(\theta3(\theta))} & \frac{kb \cdot (\sin(\theta1(\theta)) \cdot \cos(\theta3(\theta)))}{\cos(\theta) \cdot k2r + k2t \cdot \cos(\theta3(\theta))} \\ 0 & 0 & 0 \end{bmatrix}$$

### Le désaccord de phase

En mettant en facteur  $\exp(ikr)$  dans l'expression de  $E2\omega$ , on isole le terme ci-dessous qui s'appelle désaccord de phase:

$$\Delta \vec{k} = \vec{k}_{2\omega} - 2\vec{k}_{\omega} = \frac{2\omega}{c} (n_{2\omega} \cos(\theta3) - n_{\omega} \cos(\theta1)) \hat{z}$$

Rigoureusement, le vecteur  $r$  dans la phase est celui qui réunit les deux faces en suivant la direction de propagation de l'énergie. Mais, comme la différence des vecteurs d'onde est un vecteur de  $z$ , le désaccord de phase  $\Delta k \cdot s$  est seulement défini par la distance entre les dioptries.

on a :

$$s = z / \cos(z, E^*H) \quad \hat{z} \cdot \vec{s} = z \quad \Delta k \cdot s \text{ est renommé } \Delta(z, \theta) \quad \Delta(z, \theta) := \frac{2 \cdot \omega}{c} (n_{2\omega} \cdot \cos(\theta3(\theta)) - n_{\omega} \cdot \cos(\theta1(\theta))) \cdot z$$

### La puissance seconde harmonique transmise

le champ électrique sur la face de sortie est donc:

$$E2t(\alpha, \phi, \theta, L) := \left( T2f(\theta) \cdot \overrightarrow{E_f(\alpha, \phi, \theta)} + T2b(\theta) \cdot \overrightarrow{E_b(\alpha, \phi, \theta)} \cdot \exp(i \cdot \Delta(L, \theta)) \right)$$

L'air étant de nouveau transverse dans le milieu de sortie. La direction de propagation de l'énergie est parallèle à la direction de propagation du champ électromagnétique.

$$\text{et on a :} \quad P_{2\omega} = \frac{\epsilon_0}{2} c \cdot n_{2\omega} \left| \overrightarrow{E}_{2t}(\alpha, \phi, \theta, L) \right|^2 \cdot \pi \cdot w_0^2$$

ce qui donne en fonction de la polarisation de sortie:

$$P_{2\omega s}(\alpha, \phi, \theta, L) := \frac{\epsilon_0 \cdot c \cdot n_{2\omega}}{2} \cdot \left( \left| E2t(\alpha, \phi, \theta, L)_1 \right| \right)^2 \cdot \pi \cdot w_0^2 \quad P_{2\omega p}(\alpha, \phi, \theta, L) := \frac{\epsilon_0 \cdot c \cdot n_{2\omega}}{2} \cdot \left( \left| E2t(\alpha, \phi, \theta, L)_2 \right| \right)^2 \cdot \pi \cdot w_0^2$$

## Publication list

1. Xuan He, Bertrand Pommellec, et al. Size-controlled oriented crystallization in SiO<sub>2</sub>-based glasses by femtosecond laser irradiation, submitted to Journal of the Optical Society of America B.
2. Chaxing Fan, Bertrand Pommellec, Matthieu Lancry, Xuan He, Huidan Zeng, Abdel Erraji-Chahid, Qiming Liu, and Guorong Chen, 3D photo-precipitation of oriented LiNbO<sub>3</sub>-like crystals in silica based glass with femtosecond laser irradiation, *Optics Letters*, 37(14), (2012) 2955-2957
3. Qiming Liu, Xuan He, et al. Thermally induced nanocrystallization in SrO-TiO<sub>2</sub>-SiO<sub>2</sub> glasses tracking by the Maker fringe patterns analysis, *J. optoelectro. adv. Mater*, 14(11- 12), (2012) 905 – 909
4. Xuan He, Qiming Liu, Xiujian Zhao, B. Pommellec, M. Lancry, second-order nonlinear maker fringes measurement and simulation, *Journal of the Chinese Ceramic Society*, 2010, 38(11): 2050-2053
5. Qiming Liu, Xuan He, Xiujian Zhao, et al., Enhancement of third-order nonlinearity in Ag-nanoparticles contained chalcocalide glasses, *J.Nano Res.*,13, 2011, 3693-3697
6. Qiming Liu, Xuan He, et al. Third-order nonlinearity in Ag-nanoparticles embedded 56GeS<sub>2</sub>-24Ga<sub>2</sub>S<sub>3</sub>-20KBr chalcocalide glasses, *J. Non-Cryst Solids*, 357, 2011, 2320–2323.
7. X. He, Q. Liu, H. Zhou, Y. Hou, S. Qian, X. Zhao, Effect of CdS on the third-order nonlinearity in bulk GeS<sub>2</sub> -Ga<sub>2</sub>S<sub>3</sub> -CdS chalcogenide glasses, *J. optoelectro. adv. Mater*, 13, (2011) 19 - 23
8. Qiming Liu, Xuan He, et al. Optimized second-order optical nonlinearity in thermally poled GeS<sub>2</sub>-Ga<sub>2</sub>S<sub>3</sub>-KI chalcocalide glass, *Applied Physics A: Materials Science & Processing*, 2011, 102( 1): 245-249